



EDITORIAL BOARD

Editor-in-Chief

B.E. Paton

Scientists of PWI, Kyiv

S.I. Kuchuk-Yatsenko (*vice-chief ed.*),

V.N. Lipodaev (*vice-chief ed.*),

Yu.S. Borisov, G.M. Grigorenko,

A.T. Zelnichenko, V.V. Knysh,

I.V. Krivtsun, Yu.N. Lankin,

L.M. Lobanov, V.D. Poznyakov,

I.A. Ryabtsev, K.A. Yushchenko

Scientists of Ukrainian Universities

V.V. Dmitrik, NTU «KhPI», Kharkov

V.V. Kvasnitsky, NTUU «KPI», Kyiv

E.P. Chvertko, NTUU «KPI», Kyiv

Foreign Scientists

N.P. Alyoshin

N.E. Bauman MSTU, Moscow, Russia

Guan Qiao

Beijing Aeronautical Institute, China

M. Zinigrad

Ariel University, Israel

V.I. Lysak

Volgograd STU, Russia

Ya. Pilarczyk

Welding Institute, Gliwice, Poland

U. Reisgen

Welding and Joining Institute, Aachen, Germany

G.A. Turichin

St. Petersburg SPU, Russia

Founders

E.O. Paton Electric Welding Institute, NASU

International Association «Welding»

Publisher

International Association «Welding»

Translators

A.A. Fomin, O.S. Kurochko, I.N. Kutianova

Editor

N.G. Khomenko

Electron galley

D.I. Sereda, T.Yu. Snegiryova

Address

E.O. Paton Electric Welding Institute,

International Association «Welding»

11 Kazimir Malevich Str. (former Bozhenko Str.),

03150, Kyiv, Ukraine

Tel.: (38044) 200 60 16, 200 82 77

Fax: (38044) 200 82 77, 200 81 45

E-mail: journal@paton.kiev.ua

www.patonpublishinghouse.com

State Registration Certificate

KV 4790 of 09.01.2001

ISSN 0957-798X

DOI: <http://dx.doi.org/10.15407/tpwj>

Subscriptions

\$384, 12 issues per year,

air postage and packaging included.

Back issues available.

All rights reserved.

This publication and each of the articles contained

herein are protected by copyright.

Permission to reproduce material contained in this journal must be obtained in writing from the Publisher.

CONTENTS

SCIENTIFIC AND TECHNICAL

- Kuchuk-Yatsenko S.I., Zyakhor I.V., Nakonechny A.A., Zavertanny M.S. and Kapitanchuk L.M.* Resistance butt welding of titanium aluminide γ -TiAl with VT5 alloy 2
- Poznyakov V.D., Zavdoveev A.V., Gajvoronsky A.A., Denisenko A.M. and Maksymenko A.A.* Effect of pulsed-arc welding modes on the change of weld metal and HAZ parameters of welded joints produced with Sv-08kh20N9G7T wire 7
- Poklyatsky A.G., Golovatyuk Yu.V., Labur T.M., Ostash O.P. and Motrunich S.I.* Characteristics of structural strength of D16T alloy welded joints, produced by friction stir welding 13
- Borisov Yu.S., Kyslytsia O.M., Voinarovych S.G., Kuzmych-Ianchuk Ie.K. and Kaliuzhnyi S.M.* Investigation of plasmatron electric and energy characteristics in microplasma spraying with wire materials 18

INDUSTRIAL

- Yushchenko K.A., Lychko I.I., Kozulin S.M., Fomakin A.A. and Nesena I.S.* Application of electroslag welding in construction 23
- Peremitko V.V., Sukhomlin V.L., Kosinskaya O.L. and Panfilov A.I.* Effect of alloying charge and external magnetic field on structure and properties of deposited metal 28
- Soloviov V.G. and Kuskov Yu.M.* Control of the process of base metal penetration at end face electroslag surfacing in current-supplying mould 33
- Cheylyakh Ya.A. and Cheylyakh A.P.* Modeling of phase-structure state and regulation of properties of Fe–Cr–Mn alloying system metal deposited on low-carbon structural steel 39

NEWS

- Visit to welding center of ISF-2 project in Chernobyl 47

RESISTANCE BUTT WELDING OF TITANIUM ALUMINIDE γ -TiAl WITH VT5 ALLOY*

S.I. KUCHUK-YATSENKO, I.V. ZYAKHOR, A.A. NAKONECHNY,
M.S. ZAVERTANNY and L.M. KAPITANCHUK

E.O. Paton Electric Welding Institute of the NAS of Ukraine
11 Kazimir Malevich Str., 03150, Kyiv, Ukraine. E-mail: office@paton.kiev.ua

In the work, the peculiarities of formation of dissimilar joints of Ti-46Al-2Cr-2Nb alloy on the base of titanium aluminide γ -TiAl with titanium alloy VT5 in resistance butt welding, in particular, using interlayers in the form of nanolayer foils were studied. In resistance butt welding without the use of nanolayer foils it was failed to provide the defect-free joints: in the butts the presence of areas of cast metal and cracks was detected. It was found that the use of Ti/Cu and Cu-Ti/Ni-C systems as an interlayer of nanolayer foils of an eutectic type significantly influences the activation processes of the surfaces to be welded and the formation of joints in resistance butt welding. The presence of nanolayer foils in the contact zone facilitates the formation of a thin layer of the liquid phase at the initial stage of the heating process, localization of heat evolution process, activation of surfaces of both alloys with the duration of heating stage of 50–60 % of such at the direct resistance butt welding of alloys γ -TiAl and VT5. The two-stage pressure cyclogram provides formation of defect-free joints at the values of heating temperature, which are lower than those of the liquidus temperature in the system Ti-Al. According to the data of scanning electron microscopy and the EDS-analysis, the absence of the areas of cast metal and the remnants of nanolayer foils in the zone of joints was established, which testifies the solid-phase nature of the formation of joints and the complete displacement of nanolayer foils beyond the cross-section of the billets. 12 Ref., 8 Figures.

Keywords: titanium aluminide, VT5 alloy, resistance butt welding, nanolayer foil, solid-phase joint

The promising materials for production of components of aircraft and automobile engines are the intermetallic-based alloys, in particular, titanium aluminides [1–5]. Due to low specific weight and high heat resistance, titanium aluminides and the alloys based on them have advantages over the existing titanium and nickel alloys in a wide range of temperatures. The titanium aluminides are envisaged for using in manufacture of valves in automobile engines [2] and parts of aircraft engines operating at high temperatures [4].

One of the reasons that inhibits the use of intermetallic alloys is the complexity of their technological treatment, in particular, welding, predetermined by extremely low ductility at room temperature, high sensitivity to thermal and deformation cycles of treatment [6]. Perspective for the permanent joint of intermetallic alloys in similar and dissimilar combinations is the use of pressure welding methods [7–11], in particular, resistance butt welding (RBW) [10, 11]. The development of an effective technology for RBW of intermetallic alloys is associated with a number of problems, in particular, with a nonuniformity of heating and deformation processes of near-contact

material volumes, considerable resistance to plastic deformation, high electrical resistance and a large temperature range of brittleness of these alloys.

An effective technological procedure, which facilitates the activation of welded surfaces and intensification of diffusion processes in the joint zone, is the use of intermediate layers. As such layers, nanolayer foils (NF) on the base of reaction elements which are the part of materials welded [9–11] can be used. To weld dissimilar materials, it is important to use intermediate layers that will, on the one hand, facilitate the establishment of physical contact and on the other hand, prevent the mixing of elements being a part of materials welded. To such requirements intermediate layers in the form of NF correspond, having a nonuniform distribution of structure parameters across the thickness.

The previous experience shows the effectiveness of applying NF as interlayers and activators in RBW of alloys based on titanium aluminides in a homogeneous combination. The positive effect of using NF is manifested in the localization of the processes of heat evolution and deformation in the contact zone, which facilitates the activation of surfaces welded and

*According to the materials of the report at the International Conference «Titanium 2018. Production and Application in Ukraine», June 11–13, 2018, Kyiv, E.O. Paton Electric Welding Institute of the NAS of Ukraine.

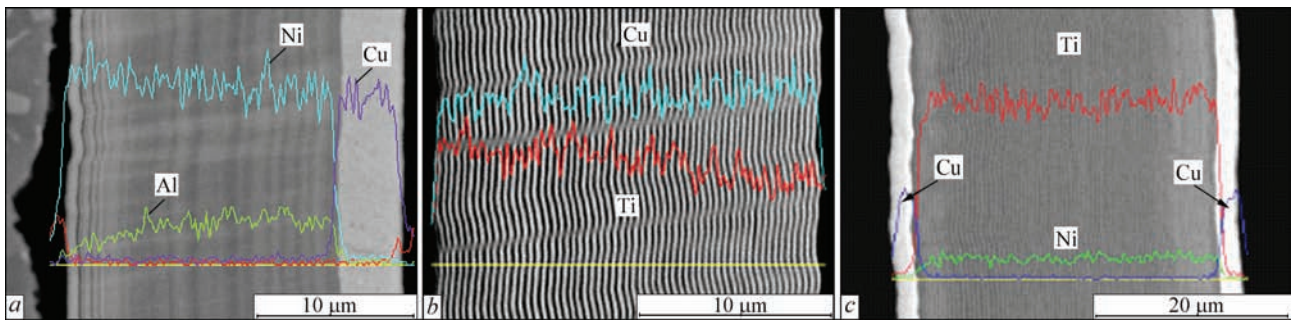


Figure 1. Electron microscopic image and distribution of components in NF of Al/Ni-Cu (a), Cu/Ti (b), Cu-Ti/Ni-Cu (c) systems

provides the formation of joints at essentially lower values of energy input [11].

The aim of investigations was to establish the peculiarities of formation of dissimilar joints of alloy on the base of γ -titanium aluminide with high-strength titanium alloy in RBW, i.e. directly and with the use of NF at a nonuniform distribution of structure parameters.

The influence of RBW modes on the formation of Ti-46Al-2Cr-2Nb (γ -TiAl) titanium aluminide joints with the alloy VT5 (hereinafter — joint γ -TiAl + VT5) was investigated. A comprehensive research methodology was developed, which included producing welded joints by different technological schemes: directly by RBW and RBW using NF of different chemical composition. To carry out investigations, the machine K766 was modernized to provide a high quick-response of compression mechanism and precision control of compression forces during the welding current passing. The range of technological parameters change was optimized based on previous experiments in such a way that to provide a predetermined value of upsetting during welding. The parameters of RBW mode were changed within the following limits: pressure at heating $P = 2\text{--}10$ MPa, pressure during upsetting of 10–50 MPa, welding time 1.5–3.5 s.

The structure of joints and presence of defects were determined by metallographic examinations of sections prepared using the chemical method of detecting the structure. An optical microscopy (Neophot-32), scanning microscopy (Auger-microprobe JAMP-9500F and scanning electron microscope JSM-35SA, JEOL), micro X-ray spectral analysis of elements distribution (EDS-analyzer INCA-450, Oxford Instruments), measurements of microhardness (M400, LECO, at loading of 1–5 N). The mechanical properties of joints were evaluated by the distribution of microhardness of metal in the zone of joint and in the zone of thermomechanical effect on the butts.

For conducting experiments on RBW with the use of intermediate layers, NF of system Ti/Al and foils with a nonuniform distribution of parameters of the structure of two types were selected: discrete (TiNb/Al, Ni/Ti-Al, Ti/Ni-Cu, Ni-Ti/Cu-Ni, Ti-Al/Ni-Ti,

Al/Ni-Cu) and gradient (Cu/Ti). The thickness of NF was 30–60 μm , the thickness of each layer was 10–50 nm. The microstructure and the results of micro X-ray spectral analysis of NF Al/Ni-Cu, Cu/Ti and Cu-Ti/Ni-Cu across their thickness are presented in Figure 1.

An essential characteristic of the discrete type of foils, used as an intermediate layer in RBW is the material of outer layers. According to the research methodology, it was envisaged that the use of NF of a discrete type with an outer layer having thermophysical characteristics different from those of alloys welded should have a significant influence on heating, deformation processes, character and intensity of diffusion processes in the contact zone during welding.

Thus, for the NF of Ti-Al/Ni-Ti the outer layer (titanium) corresponded to the base of both alloys welded; for the NF of Cu-Ti/Ni-Cu and Ni-Al/Ni-Ni, the outer layers (copper and nickel) form the low-melting eutectic with the base of both alloys. It was envisaged that during metallographic examinations of the joints, the difference in detection of the NF structure and the base metal of alloys would allow establishing the regularities of behavior of the near-contact volumes of metal and material of the interlayer in the process of welding.

The influence of RBW modes in a wide range of changes in technological parameters on the formation of γ -TiAl + VT5 joints was investigated. The structure of the joint zone produced by RBW at the optimal mode without the use of intermediate layers is shown in Figure 2, a, b, respectively, in the central and peripheral parts of the section of billets. The presence of areas of cast metal and microcracks in the joint zone is noted.

The analysis of the results of oscillography of the value of welding current and the measurement of temperature by thermocouples indicate that, in this case, during RBW process, the formation of the joint occurred through a melt layer which solidified after the stage of deformation of billets in the cooling process. During RBW without melting directly, it was not possible to form joining of the alloys γ -TiAl + VT5, as the defects of the type of oxide films and lacks of penetration were detected.

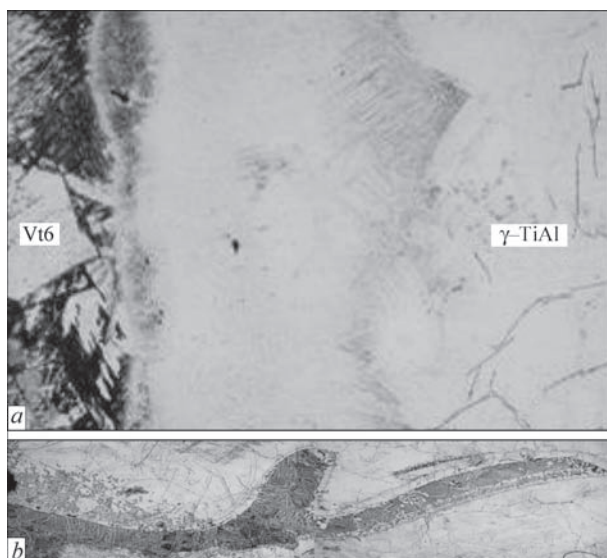


Figure 2. Microstructure (x100) of joint of the alloys γ -TiAl + VT5 at direct RBW: central part of the cross-section (a), peripheral part of the cross-section (b)

The influence of RBW modes on the structure of joints of γ -TiAl + VT5 alloys produced through NF of Ti/Al system was investigated. The temperature-time parameters of the welding process provided exceeding the melting temperature of the alloys γ -TiAl ($T_{\text{liquidus}} = 1475 \text{ }^\circ\text{C}$) and VT5 ($T_{\text{liquidus}} = 1670 \text{ }^\circ\text{C}$) in the contact zone according to the state diagram of the Ti–Al system (Figure 3) [12]. In this case, the axial force at the stage of upsetting was not increased (single-stage pressure cyclogram). It was established that during air cooling of γ -TiAl + VT5 joints produced by RBW with a single-stage pressure cyclogram, the cracks are formed in welded butts directly throughout the diffusion zone or in the areas of the γ -TiAl alloy adjacent to it (Figure 4, a), obviously, due to structural transformations «melt \rightarrow α -phase \rightarrow ($\alpha + \gamma$) \rightarrow ($\alpha_2 + \gamma$), which are accompanied by the appearance of significant welding stresses.

The structure of joints of alloys γ -TiAl + VT5, produced by RBW through the NF of Ti/Al system

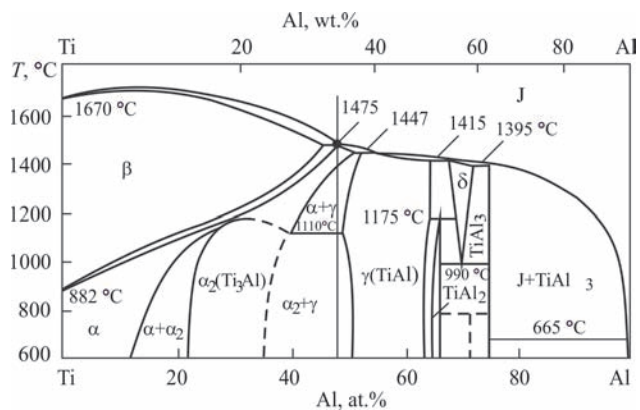


Figure 3. Diagram of state of the Ti–Al system [12]

with a two-stage pressure cyclogram, was investigated when the melting temperature of the alloy γ -TiAl was reached in the contact zone. During the analysis of the joint microstructure, the formation of common grains at the contact boundary of the alloys γ -TiAl + VT5 (Figure 4, b) is observed.

Obviously, in the process of heating during RBW, a short-term local achievement of the liquidus temperature of alloys was provided, at the same time the melt areas were solidified at the stage of deformation of billets during upsetting. In this case, the solid-phase nature of the formation of the joint γ -TiAl + VT5 in the α -region of the state diagram of the Ti–Al system was provided. The registration of thermal cycles with the help of thermocouples established that the use of NF provides localization of heat evolution in the contact area (along the axis of billets) and a more uniform heat evolution across the section of billets as compared to RBW without the use of NF.

The oxide films, pores, cracks and other defects in the joining zone were not revealed. The analysis of microstructure of joint shows the presence of a diffusion zone with a width of more than 100 μm , in which the content of titanium gradually decreases from about 93 g, at.% in the alloy VT5 to 50 at.% in the alloy of γ -TiAl, which, in accordance with the

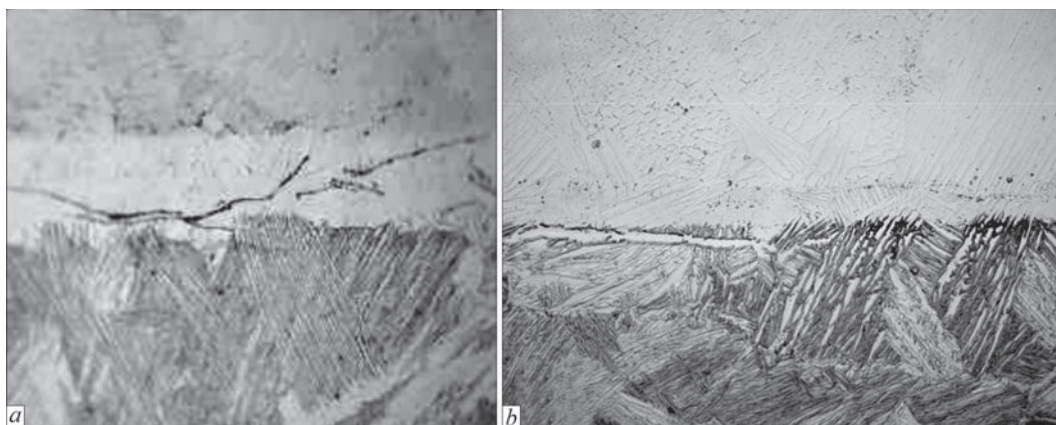


Figure 4. Microstructure ($\times 200$) of the joint γ -TiAl + VT5 in RBW through NF of Ti/Al system at one- (a) and two-stage (b) pressure cyclogram (alloy VT5 in the photo below)

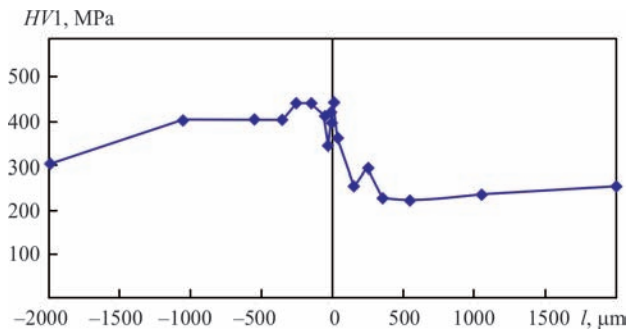


Figure 5. Change in microhardness in the joint γ -TiAl + VT5 in RBW through NF Ti/Al

state diagram of the system Ti–Al, predetermines the existence of several phases of different composition — α (Ti), $\alpha + \alpha_2$, α_2 (Ti₃Al), $\alpha_2 + \gamma$ (TiAl). The nature of change of microhardness in the zone of joining of γ -TiAl + VT5 (Figure 5) indicates the absence of areas with decreased strength in the heat-affected zone of both alloys. The presence of a wide diffusion zone is a significant factor which can affect mechanical characteristics of welded butts, in particular, the formation of cracks during their heat treatment or operational loads.

The influence of RBW modes on the structure of joints γ -TiAl + VT5 produced with the use of NF of eutectic type with a nonuniform distribution of the structure parameters across the thickness: discrete (Ni/Ti–Al, Ti/Ni–Cu, Cu–Ti/Ni–Cu, Al/Ni–Cu) and gradient (Ti/Al, Cu/Ti). The technological parameters of the RBW mode were set so, that to provide a short-term eutectic temperature exceeding in the

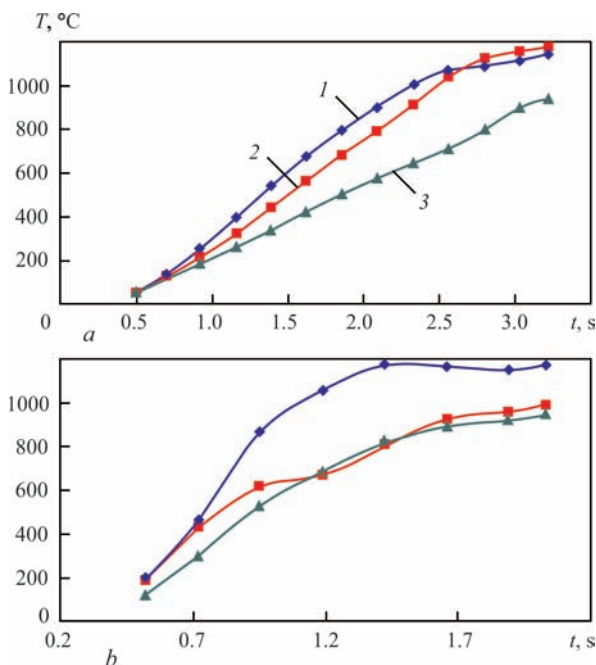


Figure 6. Change in heating temperature at the distance of 1.5 (1) 2.5 (2), 3.5 (3) mm from the butt in RBW of alloys γ -TiAl + VT5 through NF Cu–Ti/Ni–Cu (a) and Cu/Ti (b)

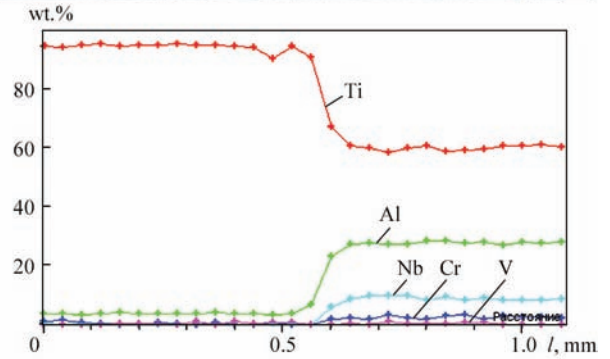
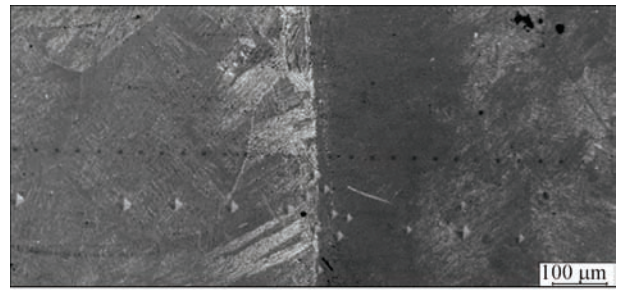
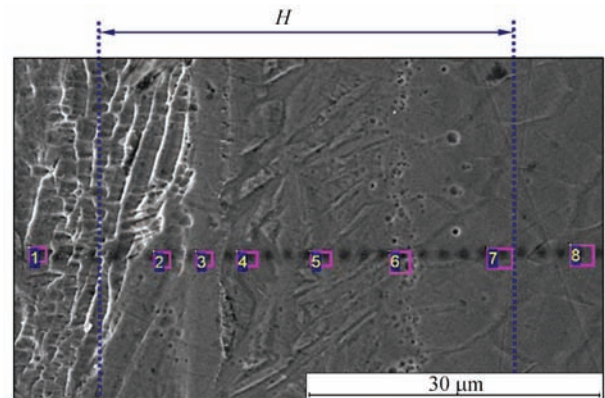


Figure 7. SEM of the image of microstructure and results of X-ray spectral analysis of the zone of the joint γ -TiAl + VT5 in RBW through NF Cu–Ti/Ni–Cu

titanium-material of external NF layer system in the contact zone.

In particular, for NF of the system Cu–Ti/Ni–Cu and Cu/Ti the heating temperature during RBW process should exceed the value of $T_{\text{eutCu-Ti}} = 885^\circ\text{C}$ for a short time in accordance with the state diagram of the system Cu–Ti [12]. At the same time, the temperature-time conditions of the RBW process (value



Spectrum	C	Al	Ti	V	Cr	Nb
1	1.27	5.32	93.15	0.15	0.10	0
2	0.75	12.03	86.31	0.66	0.15	0.11
3	0.91	14.46	84.44	0	0.08	0.12
4	0.95	17.99	80.44	0.13	0.24	0.25
5	0.76	20.68	76.47	0	0.76	1.33
6	0.96	22.54	71.15	0	1.46	3.89
7	1.04	25.46	66.13	0	0.99	6.38
8	0.77	25.87	62.98	0.05	2.09	8.23

Figure 8. Microstructure and chemical composition of metal in different areas of the joint γ -TiAl + VT5 in RBW through NF Cu–Ti/Ni–Cu, wt.%, H — width of diffusion zone

of voltage, current, time, heating pressure, upsetting pressure) were controlled in such a way that to prevent exceeding the melting temperature of alloy γ -TiAl in the contact zone (Figure 6). The process of forming the joint occurs in α -region or $(\alpha + \gamma)$ region according to the state diagram of Ti–Al system.

The experiments showed that the optimal conditions for formation of joints in RBW are provided with the use of NF of systems Cu–Ti/Ni–Cu and Cu/Ti. The microstructure of joint γ -TiAl + VT5 at scanning electron microscopy (SEM) and the results of micro X-ray spectral analysis are presented in Figures 7, 8.

It was established that the use of NF significantly influences the processes of activation of surfaces welded and the formation of joints. The use of the systems Cu–Ti/Ni–Cu and Cu/Ti in RBW with a two-stage pressure cyclogram facilitates the formation of a thin layer of liquid phase at the initial stage of heating process, localization of heat evolution process, the activation of surfaces of both alloys and the formation of defect-free joints at the stage of upsetting with the duration of heating stage being 50–60 % of such at the direct RBW. With the help of SEM (Auger-microprobe JAMP-9500F, JEOL EDS-analyzer INCA-450), the absence of areas of cast metal, NF remnants was established in the joints zone, which proves the solid-phase nature of formation of joints and the complete displacement of NF beyond the boundaries of the cross-section of billets. The width of the diffusion zone in the joint γ -TiAl + VT5 does not exceed 50 μm (Figure 8).

Conclusions

1. In resistance butt welding (RBW) of the alloy γ -TiAl with titanium alloy VT5 without the use of intermediate layers it was not possible to provide defect-free joints: the presence of areas of cast metal and cracks was recorded in the butts. The formation of joints occurred through a melt layer, which solidified after the stage of deformation of billets during cooling of the butts.

2. In the butts produced by RBW through the NF of the Ti/Al system at a single-stage pressure cyclogram, the cracks are formed directly across the diffusion zone or in the areas of the alloy γ -TiAl adjacent to it apparently, due to the structural transformations «melt \rightarrow α -phase \rightarrow $(\alpha + \gamma) \rightarrow (\alpha_2 + \gamma)$, which are accompanied by the appearance of significant welding stresses.

3. Two-stage pressure cyclogram in RBW through the NF of the Ti/Al system provides the formation of defect-free joints. The presence of a diffusion zone with a width of more than 100 μm is a significant factor that can affect the mechanical characteristics of welded butts, in particular, the formation of cracks during their heat treatment or operating loads.

4. The use of the eutectic type of the Ti/Cu and Cu–Ti/Ni–Cu systems as an intermediate layer of NF significantly affects the activation processes of welded surfaces and formation of joints in RBW. The presence of NF in the contact zone results in the formation of a thin layer of liquid phase at the initial stage of heating process, localization of heat evolution process, activation of surfaces of both alloys at the duration of heating stage of 50–60 % of such at direct RBW of alloys γ -TiAl and VT5.

5. In RBW with a two-stage pressure cyclogram, the formation of defect-free joints is provided at the values of heating temperature lower than the liquidus temperature in the Ti–Al system. According to the data of micro X-ray spectral analysis, the absence of the areas of cast metal and the NF remnants was established, which testifies the solid-phase nature of the formation of joints and the complete displacement of NF beyond the cross-section of the billets.

- Chesnutt, J., Hall, J., Lipsitt, H. (1995) Titanium intermetallics — present and future. In: *Proc. of 8th World Conf. of Titanium* (UK, Birmingham, 22–26 October, 1995). The Institute of Materials, 70–79.
- Hurta, S., Clemens, H., Frommeyer, G. et al. Valves of intermetallic γ -TiAl-based alloys: Processing and Properties. *Ibid.*, 97–104.
- Iliin, A.A., Kolachev, B.A., Polkin, I.S. (2009) *Titanium alloys. Composition, structure, properties*: Refer. Book. Moscow, VILS-MATI [in Russian].
- Kablov, E.N., Lukin, V.I. (2008) Intermetallics based on titanium and nickel for advanced engineering products. *The Paton Welding J.*, **11**, 65–70.
- Grigorenko, S.G., Grigorenko, G.M., Zadorozhnyuk, O.M. (2017) Intermetallics of titanium. Peculiar features, properties, application (Review). *Sovrem. Elektrometall.*, **3**, 51–58 [in Russian].
- Jian Cao, Junlei Qi, Xiaoguo Song, Licai Feng (2014) Welding and joining of titanium aluminides. *Materials*, **7**(7), 4930–4962.
- Yushtin, A.N., Zamkov, V.N., Sabokar, V.K. et al. (2001) Pressure welding of intermetallic alloy γ -TiAl. *The Paton Welding J.*, **1**, 33–37.
- Sabokar, V.K., Akhonin, S.V., Petrichenko, I.K. et al. (2009) Pressure welding of titanium aluminide to other titanium alloys. *Ibid.*, **12**, 10–12.
- Gorban, V.F., Kharchenko, G.K., Falchenko, Yu.V. et al. (2009) Investigation of joints of titanium aluminide with titanium alloy VT8 produced by diffusion welding. *Ibid.*, **12**, 7–9.
- Kuchuk-Yatsenko, V.S., Shvets, V.I., Sakhatsky, A.G. et al. (2009) Features of resistance welding of titanium aluminides using nanolayered aluminium-titanium foils. *Ibid.*, **3**, 11–14.
- Kuchuk-Yatsenko, S.I., Zyakhor, I.V., Chernobaj, S.V. et al. (2015) Structure of γ -TiAl joints in resistance butt welding with application of interlayers. *Ibid.*, **9**, 5–12.
- Barabash, O.M., Koval, Yu.N. (1986) *Crystalline structure of metals and alloys*: Refer. Book. Kiev, Naukova Dumka [in Russian].

Received 17.07.2018

EFFECT OF PULSED-ARC WELDING MODES ON THE CHANGE OF WELD METAL AND HAZ PARAMETERS OF WELDED JOINTS PRODUCED WITH Sv-08Kh20N9G7T WIRE

V.D. POZNYAKOV, A.V. ZAVDOVEEV, A.A. GAJVORONSKY,
A.M. DENISENKO and A.A. MAKSYMENKO

E.O. Paton Electric Welding Institute of the NAS of Ukraine
11 Kazimir Malevich Str., 03150, Kyiv, Ukraine. E-mail: office@paton.kiev.ua

Pulsed-arc welding is characterized by periodically varying arc power and due to its peculiarities it allows solving complex technology issues in development of unique structures, increasing the efficiency of welding processes, and depositing corrosion-resistant alloys on steel. At present, there is a great number of welding equipment manufacturers, who have introduced the ideas of pulsed welding application in their production. However, the data on the effect of pulsed-arc welding on the welding thermal cycles are of a fragmentary nature, and, therefore, it is difficult to compare the thermal cycles typical for stationary and pulsed-arc welding. In welding of high-carbon steels there is a problem of reducing weld metal mixing with base metal and the resulting increase of welded joint cold cracking resistance. Successful application of pulsed-arc welding for solution of the above-mentioned problems necessitated performance of comparative investigations of the effect of the modes of pulsed-arc welding on the parameters of welds, HAZ and welding thermal cycles in comparison with stationary arc welding produced with high-alloy welding consumables. This was the main aim of the investigations, the results of which are given in this paper. 31 Ref., 8 Figures.

Keywords: *pulsed-arc welding, pulsating-arc welding, welding thermal cycle, heat-affected zone, high-alloy welding consumables*

Pulsed-arc welding (PAW) is characterized by periodically changed power of the arc, and it has been known since 1940s. Welding process with periodically changed arc power was proposed for the first time in the USSR in 1953 by Zajtsev M.P., for welding steel sheets, in order to reduce the heat losses [1]. However, the first mention of pulsed welding in the world dates back to 1932. This kind of welding was invented by engineer Earl J. Ragsdale in Budd Company in 1932 for stainless steel welding and was used to manufacture diesel railway train Pioneer Zephyr [2]. Pulsed-arc welding in this case allowed 3–8 times increase of labour efficiency, compared to nonconsumable electrode welding, and considerable reduction of deformation during its performance at practically the same quality of welded joints. Different authors called welding with periodically changing power of the arc in different ways: pulsed-arc, pulsating-arc, modulated current, and nonstationary arc welding. However, the common name of all the above methods is modulated current welding (MCW) [3]. MCW mainly allows ensuring a controllable transfer of electrode metal, increasing arcing stability, reducing spatter, as well as controlling the rate and direction of weld pool metal solidification, regulating the thermal impact on

the heat-affected zone (HAZ) of welded joints. By pulse repetition rate MCW is divided into PAW ($f \geq 25$ Hz, Figure 1, *a*) and pulsating-arc welding ($f < 25$ Hz, Figure 1, *b*).

PAW [4–6] provides controllable transfer of electrode metal, the main condition of which is drop detachment by each current pulse and possibility of controlling their transfer frequency. It is believed that in gas-shielded welding, the pulse duration should be sufficient for detachment of the electrode metal drop. In the case of drop detachment at the current close to the amplitude value, metal transfer is accompanied by greater spatter [7]. Minimum spattering losses and controlled metal transfer at welding in all the positions ensure drop detachment at the end of pulse action. The main advantages of PAW include its ability to be used for critical structures from different steel grades, aluminium, copper, nickel alloys and titanium of 1 mm and greater thickness.

Owing to high spatial stabilization of the arc and possibility of application of greater electrode extension, this process can be used with success, both for welding thin metal, and for thick-walled structures. PAW in an intermediate link between spray transfer and short arc welding that makes it ideal for weld-

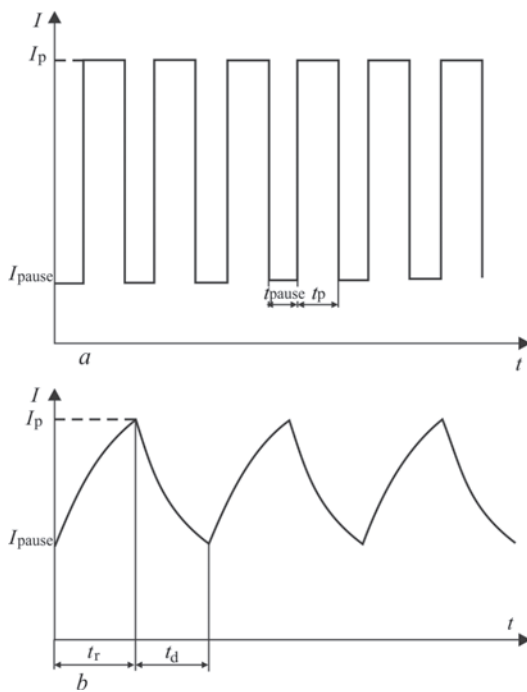


Figure 1. Change of current in time at PAW ($f \geq 25$ Hz) (a) and pulsating-arc welding ($f < 25$ Hz) (b): t_p — pulse time; t_{pause} — pause time; t_r — current rise time; t_d — current drop time; I_p — pulse current; I_{pause} — pause current

ing thick metal, where heat input control is required. PAW, owing to its features, allows solving complex technological issues at development of unique structures, increasing the efficiency of the welding processes, and depositing corrosion-resistant alloys on steel [8]. At present there exists a great number of welding equipment manufacturers, who introduced the ideas of pulsed welding application in their production. Swedish Company ESAB developed Aristo 500 power source for PAW [9] with program control, which automatically assigns the welding modes, according to synergistic dependencies. US Company Hobart developed Ultra-Arc 350 system for consumable electrode PAW [10]. This system has nine programs, envisaging welding of carbon and stainless steels in a mixture of gases with 0.8 and 1.2 mm wires. PWI developed I-169 power source for PAW with smooth regulation of the parameters of current pulses of a stepped form [11].

An important condition of the stationary nature of running of PAW process is the optimum combination of the pulse and pause parameters [8, 12–19]. In view of the fact that the number of variable parameters at PAW is considerable, selection of their optimum combination is a quite labour-consuming process and it includes a large number of trials and errors [20]. General recommendation for selection of an optimum combination of PAW parameters is transfer of one drop per pulse [8, 12]. This condition, which is the

criterion of metal transfer, can be expressed by the following relationship [12, 21]:

$$D = I_p^n t_p, \quad (1)$$

where D is the constant, depending on drop volume, welding wire composition and diameter; exponent « n » has the average value of 2.

If values I_p/I_{pause} are small, then the energy of one pulse is insufficient for drop detachment. In this case, the drop can separate from the electrode under the impact of gravitation forces. In the case, when the products of pulse current and time have large values, two or three drops can separate per one pulse, and the stability of the welding process is disturbed. Minimum pause current is selected so that the arc was not extinguished during the pause. Modern power sources use the above-listed recommendations for PAW in the programmed modes. As a rule, operator instrument panels show average values of current, which is determined by the following equation [8, 12, 22]:

$$I_{\text{av}} = \frac{I_p t_p + I_{\text{pause}} t_{\text{pause}}}{t_p + t_{\text{pause}}}. \quad (2)$$

In this case, it is possible to compare PAW modes with those of stationary welding, welding heat input is directly proportional to welding current.

One of the most important characteristics, determining the welded joint properties, is the welding thermal cycle (WTC), which determines the HAZ metal structure. Knowing the features of WTC at pulsed-arc welding mode it is possible to predict formation of the structure and properties of welded joint HAZ. So, for instance the authors of [12, 23–25] report that PAW is characterized by a lower level of heat input, thus ensuring penetration comparable with spray transfer. K. Tsen [26], measuring the welding thermal cycles for the stationary and pulsating modes, at 2 mm distance from the fusion line, showed that in the latter case smaller maximum temperature of metal heating is achieved. This fact can be an indication, in the opinion of the authors of [26], of smaller heat input. As the metal heating temperature is smaller in the case of the pulsed process at the same distance from the fusion line, this leads to an indirect conclusion that the HAZ width in this case was smaller, and that the rate of metal cooling in the high-temperature region was higher, compared to the process, which was performed by a stationary arc. The effect of the pulse repetition rate and fullness on the metal cooling rate is considered in [27]. It is shown that in the range of the change of repetition rate from 60 up to 120 Hz and of fullness from 20 up to 30 %, the cooling rate practically does not change, either in the high-tem-

perature, or in the low-temperature regions. Values of pulse repetition rates and fullness were selected, proceeding from the fact that these ranges of PAW parameters cover a wide area of practical application [28]. It should be also noted that based on WTC data for the pulsed mode, a certain «tooth» (jump) in metal temperature variation is observed in the high-temperature region that, in all probability, is attributable to the features of pulsed heat input into the weld pool. Study of WTC in the case of pulsating-arc welding [22, 29] showed that in the low-temperature range the rate of HAZ metal cooling is slowed down, compared to the stationary mode, and in the high-temperature range it is accelerated. Here, in the case [29] of arc pulsation frequency rising from 0.5 up to 10 Hz, the rate of HAZ metal cooling becomes the same, as in the case of stationary welding, that is indicative of irrationality of further increase of pulsation frequency.

It should be also noted that the data on PAW effect on the welding thermal cycles are of a fragmentary nature and, therefore, it is difficult to make a comparison between the thermal cycles, characteristic for welding by a steadily burning and pulsed arc. A similar situation is observed in investigations, dealing with variation of weld parameters [30, 31]. The works mainly give comparison of weld parameters at different variants of pulsed or pulsating welding, whereas comparison with similar results for stationary arc welding is absent. Such data are required for understanding the conditions, under which stationary arc welding can be replaced by PAW, in order to increase the productivity and improve product quality. For performing tasks such as welding of high-strength fine-grained steels, it was necessary to solve two mutually exclusive problems of improvement of the process productivity and ensuring the fine-grained structure in the HAZ metal, as well as good penetration of the weld root. Moreover, in welding high-carbon steels, the problem arises of reducing weld metal mixing with base metal and this way increasing welded joint resistance to cold cracking. Thus, successful application of PAW in solving the above problems necessitated performance of comparative studies of the influence of PAW modes on the parameters of welds (width, reinforcement height, penetration depth), HAZ and WTC, compared to stationary arc, performed earlier by high-alloy welding consumables. This was the main purpose of investigations, the results of which are given in this paper.

Experimental procedure. In order to solve the problem defined in the work, beads were deposited by HORDA 307Ti high-alloyed welding wire, which is an analog of the known wire of Sv-08Kh20N19G7T grade. Wire of 1.2 mm diameter was used. Deposition was performed on 10 mm plates from 09G2S steel. Plates with the deposited bead were used to prepare

sections for performing measurements of weld and HAZ parameters. To reveal the HAZ, the sections were subjected to macroetching by a solution of ferric chloride. WTC of the HAZ overheated zone was recorded, using chromel-alumel thermocouples of 0.5 mm diameter. The thermocouple was mounted in the HAZ area, which was heated up to the temperature of 1200 °C.

To assess the effect of PAW modes on weld parameters the following modes were selected: welding current $I = 120, 160, 200, 240$ A, voltage $U = 20, 24, 28, 30$ V, welding speed of 15 m/h, shielding gas — a mixture of Ar + 18 % CO₂. Inverter type rectifier of ewm Phoenix Pulse 401 grade was used as the current source, which provides pulse repetition rate of 130 Hz at PAW.

Optimum pulsation modes were selected using a pulsating arc. In this case the welding mode was as follows: pulse welding current $I_p = 160$ A, pause current (base current) $I_{\text{pause}} = 80$ A; arc voltage in the pulse $U_p = 24$ V, arc voltage in the pause $U_{\text{pause}} = 18$ V; $v_w = 15$ m/h. Pulse time t_p and pause time t_{pause} as well as pause current and pulse-to-pause ratio were varied. Values of pause current were as follows: $I_{\text{pause}} = 60, 80, 100, 120$ A; pulse-to-pause ratio was varied from 1.4 up to 2.0, pulse repetition rate was higher than 0.5 Hz.

Results and their discussion. *Pulsed-arc welding.* Appearance of bead deposits, made by stationary welding and PAW, is given in Figure 2. At comparison of stationary and pulsed-arc welding modes one can clearly see, that at PAW the weld bead is more uniform and regular without traces of spattering (Figure 2, *b*). Measurements of metal losses for spatter showed that at PAW it is reduced by an order of magnitude, from 0.7 % at stationary mode to 0.07 % at PAW.

Analysis of the cross-section of the beads deposited in different modes, revealed that the penetration depth at PAW becomes greater, compared to stationary welding in the same modes (Figure 3). The shape of weld penetration at PAW differs significantly from

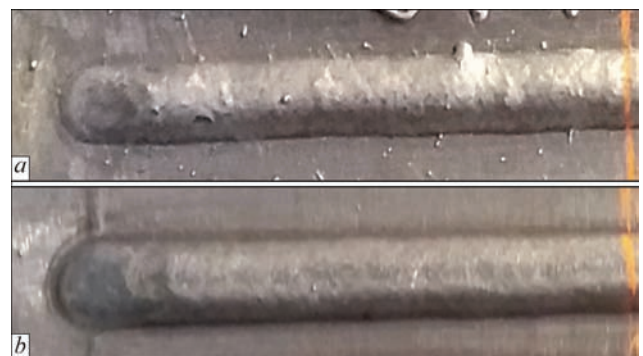


Figure 2. Appearance of the deposited bead: *a* — stationary welding mode; $I_w = 160$ A; $U = 24$ V; *b* — pulsed welding mode, $I_{\text{av}} = 160$ A; $U = 24$ V, welding speed of 15 m/h in both the cases

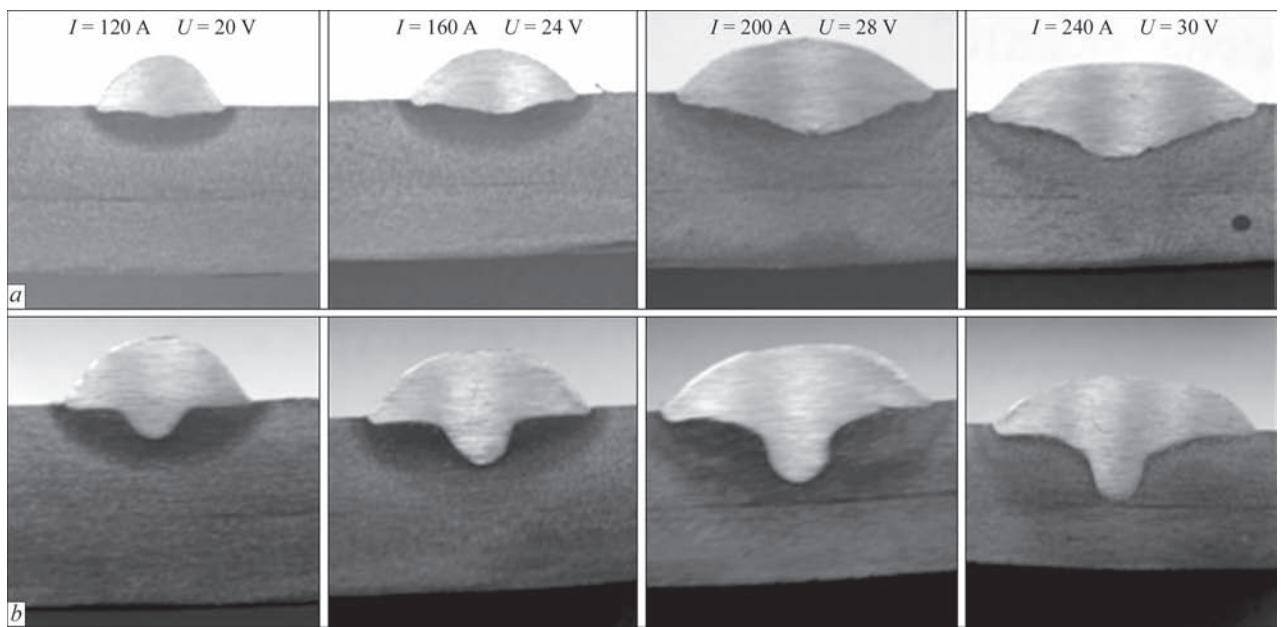


Figure 3. Appearance of the deposits, made by stationary-arc welding (*a*) and PAW (*b*) at the speed of 15 m/h; transverse macrosections the process, which was performed by stationary arc. Quantitative analysis showed that the weld width also becomes greater with increase of welding current. The nature of variation of this value is the same, both for welding by a stationary arc, and for PAW. A similar dependence is also observed for weld height. As regards penetration depth, on the whole, it increases

with increase of welding current, but in the case of PAW the penetration depth is practically two times greater than in the case of stationary arc welding (Figure 4, *a*). At PAW also the weld cross-sectional area exceeds these values for stationary arc welding. HAZ value under the cap is comparable for both kinds of welding, and in the weld root the HAZ is smaller at PAW (Figure 4, *b*). Another important parameter is the width of the HAZ at weld surface, the values of which in PAW at currents higher than 160 A become smaller than in stationary arc welding.

Pulsating-arc welding. At pulse frequency of 0.3 Hz coarse-flaky intermittent weld forms (Figure 5), where the uniformity of bead width along weld length increases with pulse-to-pause ratio reduction. At small frequency of arc pulsations also a nonuniform penetration of the plate is observed (i.e. a marked change of penetration depth along the weld length is found, which reaches 70 %, Figure 5, *b*). Penetration uniformity can be increased by increasing the arc pulsation frequency up to 1 Hz. At constant values of

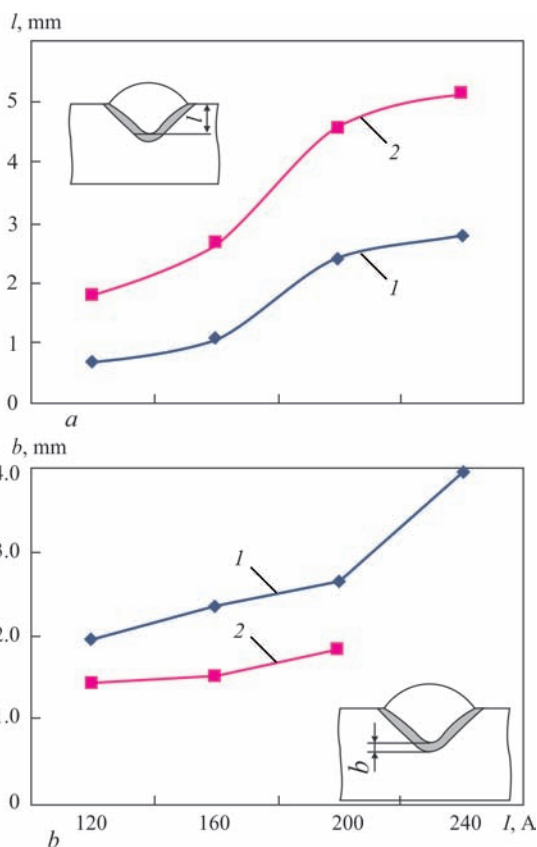


Figure 4. Change of weld and HAZ parameters at stationary-arc welding (1) and PAW (2), welding speed of 15 m/h: *a* — penetration depth; *b* — HAZ width in weld root

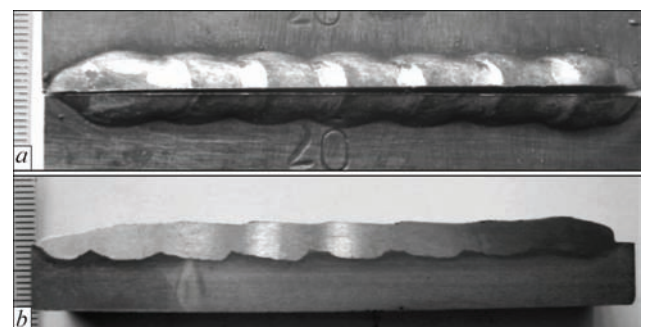


Figure 5. Appearance of deposited bead in the mode of pulsating-arc welding with pulse repetition rate of 0.3 Hz ($I_p = 160$ A, pulse voltage $U_p = 24$ V; $I_{\text{pause}} = 80$ A; $U_{\text{pause}} = 18$ V); *a* — top view; *b* — longitudinal section

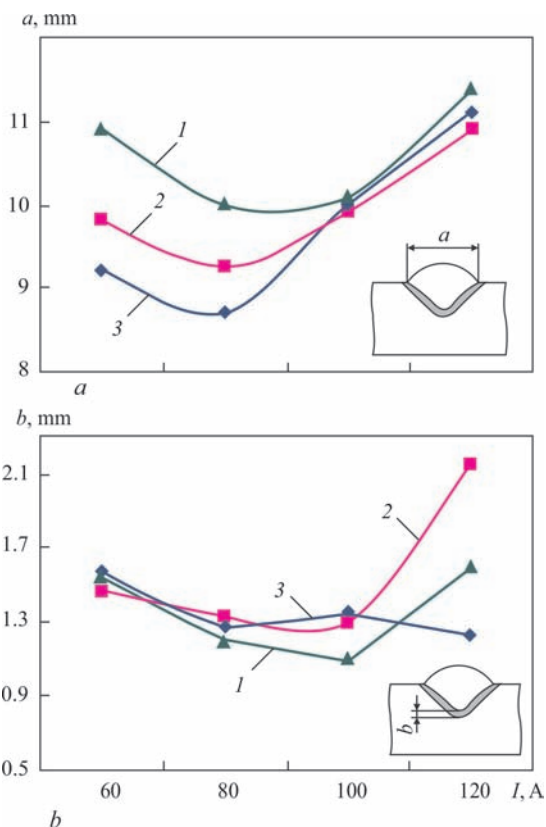


Figure 6. Change of weld and HAZ parameters in pulsating-arc welding, $I_p = 160$ A; $U_p = 24$ V (pulse-to-pause ratio: 1 — 1.4; 2 — 1.5; 3 — 2.0): a — weld width; b — HAZ width in weld root

average current and process pulse-to-pause ratio, also the uniformity of weld bead formation is improved and flakiness becomes smaller with increase of arc pulsation frequency. Experimental data show that with increase of pause current the weld width first somewhat decreases, and then increases, smaller values of pulse-to-pause ratio corresponding to greater weld width (Figure 6, a). Weld height increases uniformly with increase of pause current. Change of penetration depth has some features. At pulse-to-pause ratio equal to two, it changes from 1 mm (that corresponds to penetration depth at stationary welding mode at specified current) up to 1.8 mm. At smaller pulse-to-pause ratio (1.4 and 1.5) the values of penetration depth are in the range of 1.7 mm that is by 70 % greater than in the stationary mode. Weld area increases accordingly with increase of pause current.

Change of HAZ parameters under the cap is of a monotonic nature. Smaller pulse-to-pause ratio corresponds to greater values of HAZ width. It is important to note that average HAZ values under the cap are lower than in stationary arc welding and PAW. Similar regularities are observed also for HAZ, both in the weld root (Figure 6, b) and at the weld surface. With increase of pause current the angle of transition to base metal decreases for pulse-to-pause ratio of 2, and practically does not change for smaller values.

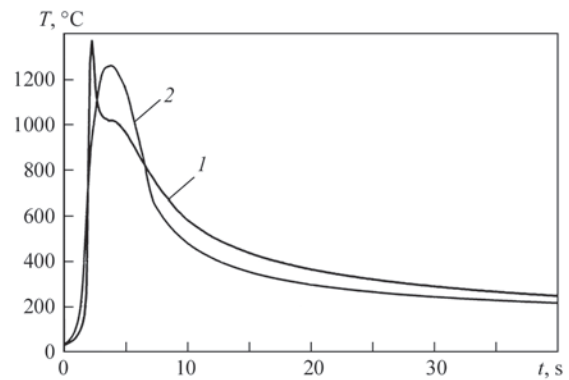


Figure 7. Welding thermal cycles in deposition of high-alloyed welding wire HORDA 307 on 10 mm plates from 09G2S steel: $I_w = 120$ A; $U_p = 20$ V, welding speed of 15 m/h (1 — PAW; 2 — stationary-arc welding)

In the welding mode with pulse current $I_p = 160$ A and pause current $I_{\text{pause}} = 120$ A (fixed pulse time of 0.5 s) with greater pause time, weld height increases, weld width becomes somewhat smaller, and HAZ width decreases, while penetration depth practically does not change. In the case of fixation of pause time (0.5 s) and increase of pulse time, weld height decreases, and weld width increases (that is, apparently, associated with increase of penetrability/effectiveness). HAZ width changes nonlinearly, first increasing, then decreasing and increasing again.

Analysis of welding thermal cycles allowed establishing the following features: at PAW the rate of rise of metal temperature in the HAZ overheated zone is greater than in the case of stationary-arc welding; in the high-temperature region from 1350 to 1000 °C metal cooling at PAW occurs faster, and in the region

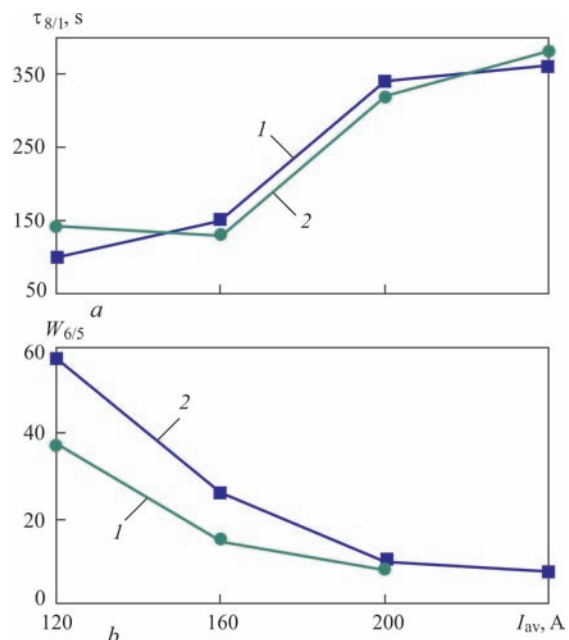


Figure 8. Change of time (a) and rate (b) of cooling of the overheated zone of HAZ metal at PAW (1) and stationary-arc welding (2) with the speed of 15 m/h. Deposition of high-alloyed welding wire HORDA 307 on 10 mm plates from 09G2S steel

of temperatures below 1000 °C it proceeds slower (Figure 7). More detailed analysis of the effect of pulsed welding mode on the rate of metal cooling in the HAZ is given in Figure 8. The given data show that the rate of metal cooling in the range of temperatures of the lowest austenite stability of 600–500 °C is lower for PAW, than in the case of stationary-arc welding, whereas time $\tau_{8/1}$ has close values.

Changes of cooling conditions, observed at transition from stationary-arc welding to PAW suggest that in this welding process a more favourable structure with a higher cold cracking and brittle fracture resistance will form in the metal of HAZ of high-strength steels with $\sigma_{0.2} > 600$ MPa. Work in this direction will be the result of out further studies.

Conclusions

1. Pulsed-arc welding allows reducing metal spatter, HAZ width, and increasing penetration depth (practically 2 times) compared to stationary arc welding. Rate of metal cooling in the HAZ in the temperature range of 600–500 °C is here reduced practically 1.5 times.

2. Application of pulsating-arc welding allows increasing weld width and reducing HAZ width, compared to stationary-arc welding.

3. Processes of pulsed-arc welding and pulsating-arc welding feature greater capabilities for controlling the weld parameters and heat input.

1. Zajtsev, M.P. *Electric arc welding method of sheet steel*. USSR author's cert. 100898, 450109/K-578 [in Russian].
2. [https://ru.wikipedia.org/wiki/ %D0 %98 %D0 %BC %D0 %BF %D1 %83 %D0 %BB %D1 %8C %D1 %81 %D0 %BD %D0 %B0 %D1 %8F_ %D1 %81 %D0 %B2 %D0 %B0 %D1 %80 %D0 %BA %D0 %B0#cite_note-2](https://ru.wikipedia.org/wiki/%D0%98%D0%BC%D0%BF%D1%83%D0%BB%D1%8C%D1%81%D0%BD%D0%B0%D1%8F_%D1%81%D0%B2%D0%B0%D1%80%D0%BA%D0%B0#cite_note-2)
3. Zaruba, I.I., Lebedev, V.K., Shejko, P.P. (1968) Welding with modulated current. *Avtomatich. Svarka*, **11**, 35–40 [in Russian].
4. Lenivkin, V.A., Dyurgerov, N.G., Sagirov, Kh.N. et al. (1989) *Technological properties of welding arc in shielding gases*. Moscow, Mashinostroenie [in Russian].
5. Potapievsky, A.G. (2007) *Consumable electrode welding in shielding gases*. Pt 1: Welding in active gases. 2nd Ed. Kiev, Ekotekhnologiya [in Russian].
6. Paton, B.E., Potapievsky, A.G., Podola, N.V. (1964) Consumable electrode pulsed-arc welding with programmable control of process. *Avtomatich. Svarka*, **1**, 2–6 [in Russian].
7. Lashchenko, G.I. (2006) *Methods of metal arc welding*. Kiev, Ekotekhnologiya [in Russian].
8. Voropaj, N.M., Ilyushenko, V.M., Lankin, Yu.N. (1999) Peculiarities of pulsed-arc welding with synergistic control of mode parameters. *Avtomatich. Svarka*, **6**, 26–32 [in Russian].
9. Melton, G.B., Aberg, P. (1991) Soldadura por pulsaciones con electrodos rellenos de fundente basico. *Dyna*, **6**, 15–18.
10. (1995) *The ultimate by Hobart*. Ultra — ARC350.
11. Shejko, P.P., Pavshuk, V.M. (1992) Power source for pulsed gas metal arc welding with smooth regulation of parameters. *Avtomatich. Svarka*, **6**, 44–46 [in Russian].
12. Palani, P.K., Murugan, N. (2006) Selection of parameters of pulsed current gas metal arc welding. *Journal of Materials Processing Technology*, **172**, 1–10.
13. Tong, H., Ueyama, T., Harada, H. (2001) Quality and productivity improvement in aluminium alloy thin sheet welding using alternating current pulsed metal inert gas welding system. *Sci. Technol. Weld. Join.*, **6**(4), 203–208.
14. Needham, J.C., Carter, A.W. (1965) Material transfer characteristics with pulsed current. *Brit. Weld. J.*, **5**, 229–241.
15. Rajasekaran, S. (1999) Weld bead characteristics in pulsed GMA welding of Al–Mg alloys. *Weld. J.*, **78**(12), 397–407.
16. Murray, P.E. (2002) Selecting parameters for GMAW using dimensional analysis. *Ibid.*, **81**(7), 125–131.
17. Amin, M., Ahmed, N. (1987) Synergic control in MIG welding 2 — power current controllers for steady dc open arc operation. *Met. Construct.*, **7**, 331–340.
18. Amin, M. (1983) Pulse current parameters for arc stability and controlled metal transfer in arc welding. *Ibid.*, **5**, 272–377.
19. Lambert, J.A. (1989) Assessment of the pulsed GMA technique for tube attachment welding. *Weld. J.*, **68**(2), 35–43.
20. Essers, W.G., Gompal Van. (1984) Arc control with pulsed GMA welding. *Ibid.*, **64**(6), 26–32.
21. Amin, M. (1981) Synergetic pulse MIG welding. *Metal construction*, **6**, 349–353.
22. Mikhoduj, L.I., Poznyakov, V.D., Denisenko, A.V. (1999) Influence of current modulation on properties of low-carbon high-strength steel welded joints performed by manual arc welding. *Avtomatich. Svarka*, **4**, 13–18 [in Russian].
23. Stanzel, K. (2001) Pulsed GMAW cuts cycle time by 600 percent. *Weld. Des. Fabricat.*, **4**, 85–87.
24. Tippins, J. (1970) Box beam fabrication using the pulsed MIG process. *Met. Construct. Brit. Weld. J.* **12**, 547–550.
25. Harvey, R.C. (1995) Gas metal arc welding fume generation using pulsed current. *Ibid.*, **74**(11), 59–68.
26. Tseng, K., Chou, C. (2002) The effect of pulsed GTA welding on the residual stress of a stainless steel weldment. *Journal of materials processing technology*, **123**, 346–353.
27. Krantz, B.M., Coppolecchia, V. (1971) The effects of pulsed gas metal-arc welding parameters on weld cooling rates. *Welding Research Supplement*, **11**, 474–479.
28. Fragetta, W.A. (1968) *Pulsed power welding of HY-130(T) steel, the effects of welding parameters on arc stability and fusion zone dimensions*. Pt I. Air Reduction Co., Inc., Murray Hill, N. J. RE-68-002- CRE-44 Contract NObs-94535 (Jan. 15, 1968).
29. Pokhodnya, I.K., Golovko, V.V., Grabin, V.F., Vasiliev, V.G. (1997) Peculiarities of thermal cycle of submerged pulsed-arc welding. *Avtomatich. Svarka*, **9**, 3–8 [in Russian].
30. Joseph, D., Farson, D., Harwig, R. (2005) Richardson Influence of GMAW-P current waveforms on heat input and weld bead shape. *Sci. Technol. Weld. Join.*, **10**(3), 311–318.
31. Tomoyuki Ueyama (2013) Trends in developments in gas shielded arc welding equipment in Japan. *The Paton Welding J.*, **10–11**, 53–60.

Received 05.07.2018

CHARACTERISTICS OF STRUCTURAL STRENGTH OF D16T ALLOY WELDED JOINTS, PRODUCED BY FRICTION STIR WELDING

A.G. POKLYATSKY¹, Yu.V. GOLOVATYUK², T.M. LABUR¹, O.P. OSTASH² and S.I. MOTRUNICH¹

¹E.O. Paton Electric Welding Institute of the NAS of Ukraine

11 Kazimir Malevich Str., 03150, Kyiv, Ukraine. E-mail: office@paton.kiev.ua

²G.V. Karpenko Physico-Mechanical Institute of the NAS of Ukraine

5 Nauchnaya Str., 79060, Lviv, Ukraine

A series of research was performed to study the characteristics of structural strength of butt joints of aluminium alloy D16T 2 mm thick, produced by friction stir welding. Features of weld formation and degree of metal softening in the zone of the produced permanent joint were analyzed. Mechanical testing of welded joint samples was performed at static and cyclic loading. Diagrams of fatigue crack growth rates in the base metal, heat-affected zone and thermomechanical impact zone, on the boundary of these zones and in the weld metal were plotted. It is shown that the characteristics of cyclic crack resistance of weld metal of these joints are more than two times higher than the respective values for base metal that is indicative of the good prospects for application of friction stir welding in fabrication of critical structures from D16T alloy. 19 Ref., 8 Figures.

Keywords: aluminium alloy D16T, friction stir welding, microstructure, cyclic crack resistance, structural strength

Aluminium alloys of different alloying systems are widely applied in aerospace engineering [1, 2]. This is due to a combination of low metal content of aluminium alloys and quite high values of strength and crack resistance that together provide a reliable and long-term operation of metal structure assemblies [3]. Under the conditions of cyclic loading, the structural strength [4] is evaluated by complex parameter $[\sigma_t \Delta K_{th} K_{fc}]$, where σ_t is the material ultimate strength, as well as the values of material cyclic crack resistance: ΔK_{th} is the fatigue threshold; ΔK_{fc} is the cyclic fracture toughness [5]. These parameters are particularly important at operation of structures by the fail-safe concept [6].

In fabrication of aerospace engineering components various methods of welding these aluminium alloys are used to produce permanent joints. Here, certain problems often arise due both to chemical composition of the aluminium alloys being welded, and to the welding process, which lead to lowering of welded joint structural strength. In particular, this is metal softening in the permanent joint zone [7], and formation of cast coarse-grained structure of welds [8], and appearance of characteristic defects in the form of pores, oxide film macroinclusions and hot solidification cracks [9–11]. Therefore, the available welding technologies are optimized, and new methods to produce permanent joints are developed, in or-

der to improve the performance of aluminium alloy components.

The method of friction stir welding (FSW) is considered to be one of the most promising in fabrication of critical structures, including aerospace engineering. It was developed in 1991 at The Welding Institute as a method to produce joints in the solid phase [12]. FSW process has a characteristic difference from other pressure welding processes, due, mainly, to application of a special welding tool (Figure 1). Therefore, the main stages of permanent joint formation are directly related to this tool. Metal heating up to the plastic state, as well as prior cleaning of the surfaces of edges to be welded from oxide film, as a result of their friction with the shoulder working surface, take

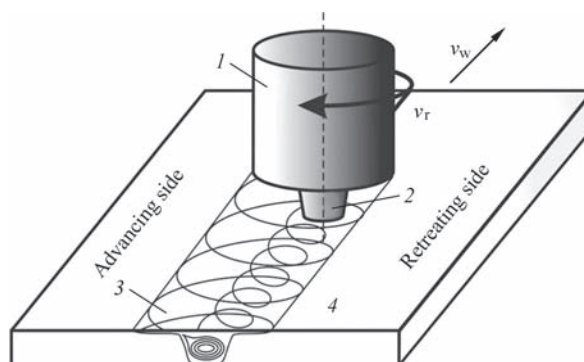


Figure 1. Schematic of FSW process: 1 — tool shoulder; 2 — tool pin; 3 — weld; 4 — welded blanks

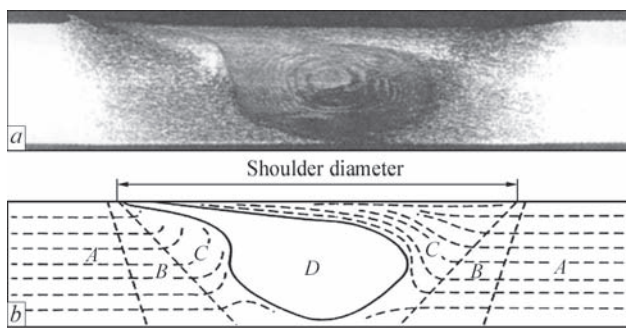


Figure 2. Transverse macrosection of the welded joint, produced by FSW (a) and respective schematic image of its characteristic zones

place under the tool shoulder. Owing to slight immersion of the tool into the metal being welded and its inclination relative to the vertical axis, the metal is in constant contact with the shoulder leading edge, forming a wave of plasticized metal owing welded. Mixing across the entire thickness occurs due to rotation of the tool pin. Metal heated up to the plastic state due to high adhesion of aluminium, is entrained by the pin side surface and is plastically deformed, moving after it. It results in intensive mass transfer of the metal being welded, at which the edges being welded are cleaned from oxide films and come into contact. Owing to intensive plastic deformation and heating, the metal goes into the plastic state, and its grains in the zone of direct impact of the tool are refined significantly that additionally promotes its viscoplastic flow. Under the shoulder rear edge, owing to tool inclination in the vertical plane, conditions are in place for additional compression of metal, moved into this zone by the pin side surface, that promotes running of relaxation processes (dynamic recrystallization, relaxation of welding stresses), as well as metal densification. Thus, physical contact at FSW is the result of degradation of the butt boundary under the impact of a special tool in the bulk limited by the tool working surfaces, substrate and the metal being welded proper.

Themomechanical conditions, at which permanent joints form in FSW result in a specific weld structure (Figure 2). Unlike welds of a cast structure, characteristic for fusion welding processes, they have fine

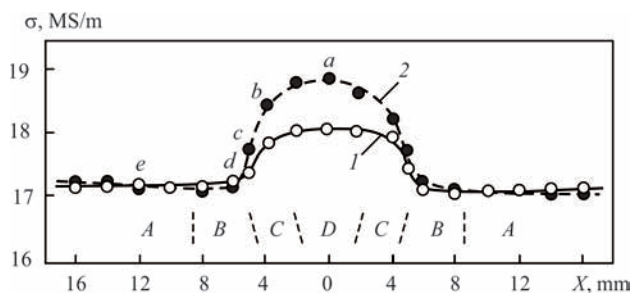


Figure 3. Change of specific electric conductivity on the sample face (1) and root (2) surfaces in the characteristic zones of FSW joint

deformed structure, with a clear-cut nugget D formed as a result of dynamic recrystallization, with up to 10 μm grain size. Bending, elongation and partial recrystallization of the grains proceed in the thermomechanical impact zone (TMIZ) C , adjacent to the nugget, as here the metal is subjected to heating and plastic deformation. Behind this area is the HAZ B , in which the metal remains undeformed and changes its structure only as a result of temperature rise. Next comes base metal zone A , where the metal does not undergo any changes [13, 14].

The objective of this work is evaluation of strength characteristics and cyclic crack resistance of welded joints of D16T alloy 2 mm thick, produced by FSW.

Experimental procedure. Investigations were conducted on butt joints of D16T alloy sheets (wt.%: 4.5 Cu; 1.7 Mg; 0.53 Mn; 0.19 Si; 0.21 Fe; 0.11 Zr; 0.06Ti; bal. — Al); welded along the rolling direction. Ultimate strength of this alloy sheets in the state after hardening and natural ageing $\sigma_t = 445$ MPa, and relative elongation $\delta = 11$ %. FSW process was performed in a laboratory unit developed at PWI. The rate of rotation of special welding tool [15] with a conical pin and 12 mm dia shoulder was 1420 rpm, and the speed of its linear displacement (welding speed) was 10 m/h.

Investigations were conducted in different zones of the welded joint (see Figure 2): in the weld central part (nugget), on the boundary of thermomechanical impact and heat-affected zones, in TMIZ and HAZ at 1 mm distance from this boundary, as well as in the base metal. These areas were selected in the characteristic points of change of local values of metal specific electric conductivity (Figure 3, points $a-f$), which is the physical characteristic of aluminium alloys, sensitive to the change of their structure and local stress-strain state, occurring during welding [3]. Values of specific electric conductivity were measured, using the eddy current method, with 1 mm step at alternating current frequency of 100 kHz that ensured the control depth up to 2 mm [16].

Metal hardness was measured on face surfaces of the produced welded joints. Degree of metal softening in the welding zone was assessed in ROCKWELL instrument at the load $P = 600$ N. Evaluation of structural features of welded joints was performed in MIM-8 optical electronic microscope. Ultimate strength of welded joints $\sigma_t^{w,j}$ and weld metal $\sigma_t^{w,m}$ was determined on standard samples with test portion width of 15 mm. Characteristics of cyclic crack resistance were determined on samples-strips 30 mm wide with side sharp (0.1 mm radius) U-shaped notch 2 mm deep along the axis of the studied zone of the welded joint, in keeping with the procedure, accepted

by ASTM International [17]. Obtained experimental data were the basis to plot the diagrams of fatigue macrocrack growth rates — $da/dN - \Delta K$ dependencies at the frequency of 10–12 Hz and coefficient of asymmetry $R = 0.1$ of the loading cycle in atmosphere at room (20 °C) temperature. Crack length was measured by cathetometer KM-6 at 25-fold magnification with 0.02 mm error. Obtained results were described by the respective analytical dependencies:

$$da/dN = C_1(\Delta K - \Delta K_{th})^{n_1}, \text{ if } 10^{-10} \leq da/dN \leq 10^{-8}, \text{ m/cycle}; (1)$$

$$da/dN = C_2(\Delta K)^{n_2}, \text{ if } 10^{-8} \leq da/dN \leq 10^{-5}, \text{ m/cycle}, (2)$$

where da is the increment of crack length between the two successive measurements; dN is the number of loading cycles between two successive measurements; n_1, n_2 is the exponent determined in keeping with the procedure of [17].

Diagrams of fatigue macrocrack growth rates were shown by lines, corresponding to these dependencies. The parameters selected as cyclic crack resistance characteristics were fatigue threshold $\Delta K_{th} = \Delta K_{10}^{-10}$ and cyclic fracture toughness $\Delta K_{fc} = \Delta K_{10}^{-5}$ the ranges of stress intensity factors ΔK at the crack growth rate $da/dN = 10^{-10}$, m/cycle and 10^{-5} , m/cycle, respectively. Microfractographic features of fatigue fracture of samples were studied in a scanning electron microscope ZeisEVO-40XPV.

Investigation results and discussion. Performed investigations showed that the weld shape and dimensions in friction stir welding differ favourably from the weld produced by nonconsumable electrode argon-arc welding (GTAW) due to weld formation on a backing without the forming groove and producing a permanent joint without filler wire application (Figure 4). Absence of reinforcement or complete penetration in it allows avoiding high levels of stress concentration in the points of weld to base metal transition, adversely affecting the performance and life characteristics of welded joints.

In addition, permanent joint formation in the solid phase without base material melting prevents appearance of characteristic defects arising in fusion welding of aluminium alloys. So, absence of molten metal, in which hydrogen solubility increases markedly, allows avoiding additional saturation of the welding zone by it, because of migration of this gas from the adjacent metal layers and pore formation. Now, deformation and intensive stirring of plasticized metal over the entire thickness of the edges during welding, promoted fragmentation of oxide films present in them. Absence of molten metal in the zone of permanent joint formation allows avoiding its oxidation during welding. Therefore, welds, obtained by friction stir welding

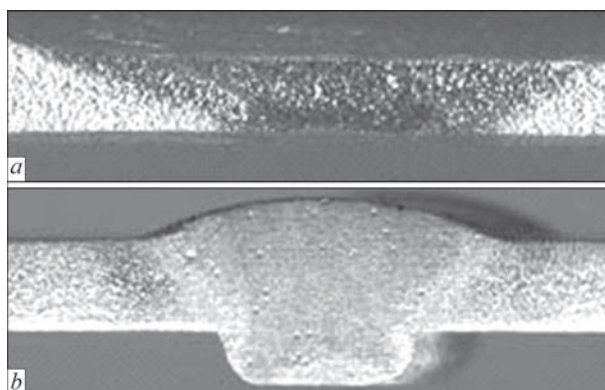


Figure 4. Transverse sections of welds of 2 mm alloy D16T produced by friction stir (a) and TIG welding (b)

have no defects in the form of oxide film macroinclusions, appearing in GTAW. The most hazardous and inadmissible defects for critical structures are hot cracks, forming during molten metal solidification in the point of accumulation of low-melting eutectic inclusions. As in friction stir welding the weld forms in the solid phase, and processes of metal melting and solidification are absent, formation of such defects can be completely avoided.

Features of weld formation in friction stir welding also have a favourable effect on the degree of metal softening in the zone of permanent joint formation. So, metal hardness measurements in the zone of permanent joint formation showed that in friction stir welding of D16T alloy, weld metal hardness practically is on the level of base metal (Figure 5). In the thermomechanical impact zone metal hardness gradually decreases at greater distance from the weld, reaching minimum value (HRB 97–98) at the boundary of the thermomechanical impact and heat-affected zones that corresponds to the point of lowering of specific electric conductivity (see Figure 3). Therefore, at uniaxial static tension samples of friction-stir welded joints have a high (425 MPa) yield limit and fail near the boundary of abutment of the thermomechanical impact zone to the heat-affected zone, where the metal hardness is minimum.

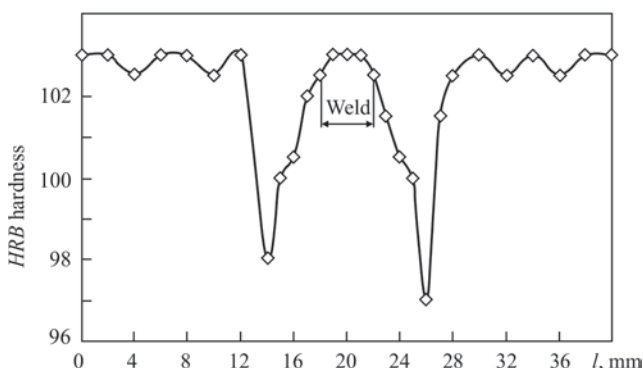


Figure 5. Hardness distribution in welded joints of D16T alloy 2 mm thick, produced by FSW

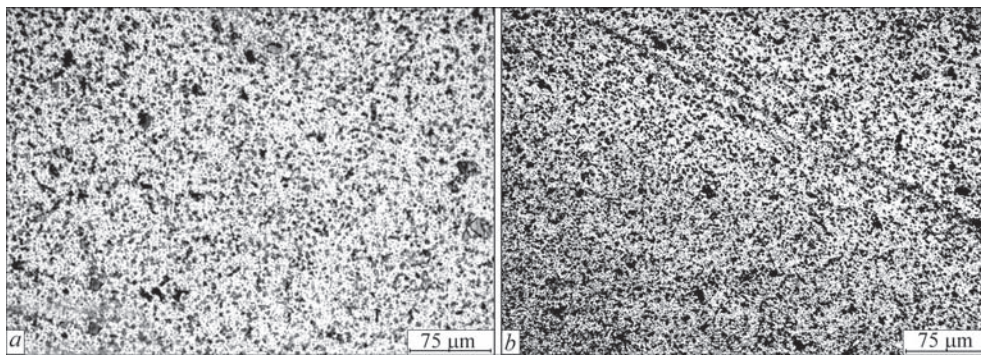


Figure 6. Microstructure of metal in weld nugget (a) and in TMIZ (b) of FSW joint

Investigation of the microstructure of welds showed that dynamic recrystallization of metal in the zone of intensive plastic deformation results in formation in the weld metal of a dispersed equilibrium structure with element size of 1–10 μm with individual intermetallics of 20–25 μm size, grouped into a conglomerate of grains of 70–150 μm size (Figure 6). Investigations of cyclic crack resistance revealed obvious differences in the diagram of the rate of fatigue macrocrack growth in the weld metal (Figure 7, curve 1), for which after intensive bulk plastic shear deformation the mid-amplitude traditionally straight Paris section is transformed into the curvilinear section with the inflection point at $\Delta K = \Delta K_0 = 20 \text{ MPa}\sqrt{\text{m}}$. This is characteristic exactly for the structure of the metal of weld, produced as a result of intensive plastic deformation of metal at FSW. Calculation of the size of cyclic plastic zone r_p^c by the following formula:

$$r_p^c = 1 / 8\pi(\Delta K / \sigma_{0.2})^2, \quad (3)$$

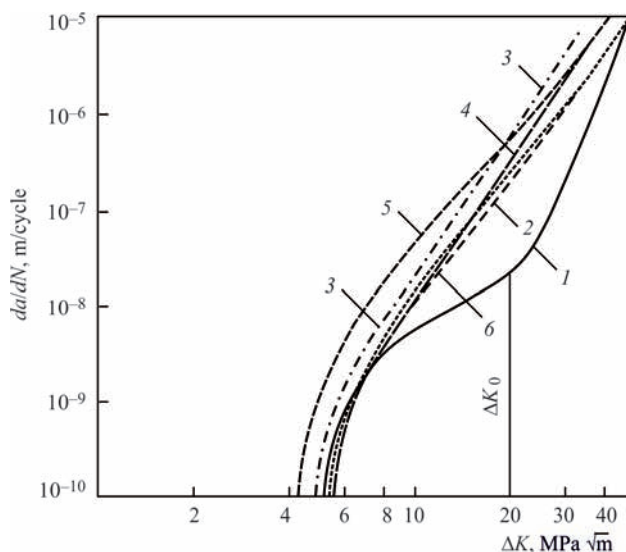


Figure 7. Diagrams of the rates of fatigue macrocrack growth in different zones of the joint produced by FSW: 1 — weld; 2 — TMIZ; 3 — HAZ; 4 — boundary of the zone of thermomechanical impact and heat-affected zone; 5 — base metal (samples cut across the rolling direction); 6 — base metal (samples cut out along the rolling direction)

where $\Delta K = 20 \text{ MPa}\sqrt{\text{m}}$, and yield limit $\sigma_{0.2} = 340 \text{ MPa}$, gives value $r_p^c = 138 \mu\text{m}$, that is in agreement with grain size (70–150 μm) of weld metal deformed during FSW. Thus, the inflection on the curve is indicative of the change of fracture mode, when at the tip of the fatigue macrocrack plastic deformation runs as multiplane dislocation slip in the volume of not one, but of several grains with involvement of grain-boundary processes. It can be also assumed that in such a deformed structure compressive residual stresses can arise [18], causing a considerable effect of crack tip closing. As a result, such weld metal, compared to base metal, demonstrates a higher fatigue threshold ΔK_{th} and cyclic fracture toughness ΔK_{fc} and, particularly, cyclic crack resistance index in mid-amplitude section of the diagram (Figure 7). Here, cyclic crack resistance of TMIZ and HAZ is somewhat lower, compared to weld metal: slightly in near-threshold section of the diagram and more in the mid- and high-amplitude sections (curves 2–4). For instance, the fatigue macrocrack growth rate at medium ΔK ranges can be by an order of magnitude higher than this value for weld metal. HAZ metal has the lowest cyclic crack resistance among all the welded joint zones (curve 3), although it is somewhat higher, compared to crack resistance of base metal, cut out across the rolling direction (curve 5), particularly in near-threshold and mid-amplitude sections of the diagram. Here, crack resistance of TMIZ metal (curve 2) is practically not inferior to crack resistance of base metal, cut out along the rolling direction (curve 6). In the high-amplitude section of the diagram, crack resistance index (cyclic fracture toughness ΔK_{fc}) of HAZ metal is much lower, compared to base metal, cut out across the rolling direction. Therefore, further on it is rational to study the possibility of its increase by changing the structural components of HAZ metal and its stress-strain state by postweld heat treatment of such joints [19].

Analysis of microfractographs of tested sample fractures is indicative of the fact that the micromechanism of fatigue crack growth in all the studied

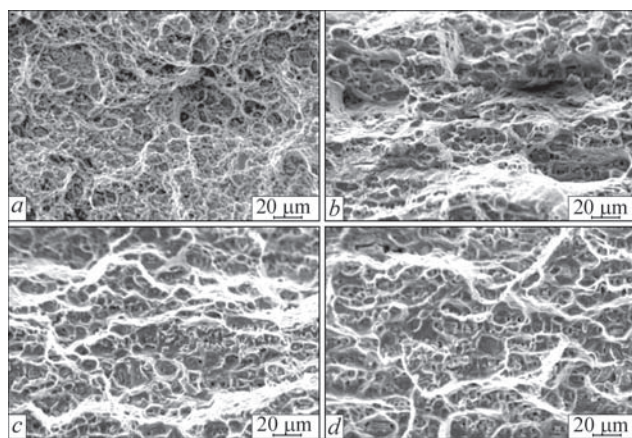


Figure 8. Microfractographs of fractures of samples failing in different joint zones: *a* — weld; *b* — TMIZ; *c* — boundary of the zones of thermomechanical impact and heat-affected zone; *d* — HAZ

zones of welded joints, produced by FSW, mainly is high-energy intensive pit one. Morphology of the pits and deformation ridges in weld metal fracture is the most finely-dispersed — individual fine cleavage sections (10–20 μm) are commensurate with weld structural elements (Figure 8, *a*). In TMIZ the number of sections of cleavage as a result of the impact of cyclic loads becomes greater, but they are divided by relatively large zones with deformation ridges (Figure 8, *b*), the most pronounced at the boundary of TMIZ and HAZ (Figure 8, *c*). Metal fracture morphology in the HAZ section is characterized by reduction of the number of extended deformation ridges and increase of the size of quasi-cleavage facets compared to weld metal (Figure 8, *d*), that, probably, is the reason for lowering of cyclic crack resistance index in this zone.

Conclusions

1. The process of friction stir welding allows producing sound welded joints of D16T alloy with high values of static strength that is just by 4–5 % smaller than the respective values of base metal.

2. High values of strength of such joints are achieved due to lowering of the level of stress concentration in the points of weld to base metal transition, absence of defects (pores, oxide inclusions and hot solidification cracks), due to metal melting and solidification in the welding zone at GTAW, and formation of a fine-dispersed deformed structure of welds.

3. Owing to high indices of cyclic crack resistance of D16T alloy welded joints, produced by friction stir welding in the solid phase, their high structural

strength is ensured that expands the possibilities for this alloy application in aerospace engineering.

1. Beletsky, V.M., Krivov, G.A. (2005) *Aluminium alloys (composition, properties, technology, application)*: Refer. Book. Ed. by I.N. Fridlyander. Kiev, Komintekh [in Russian].
2. Ishchenko, A.Ya., Labur, T.M., Bernadsky V.N., Makovetska-ya, O.K. (2006) *Aluminium and its alloys in modern welded structures*. Kiev, Ekotekhnologiya [in Russian].
3. Ostash, O.P. (2015) *Fracture mechanics and strength of materials*: Refer. Book. Ed. by V.V. Panasyuk. Vol. 15: *Structure of materials and fatigue life of structural elements*. Lviv, SPO-LOM [in Ukrainian].
4. Romaniv, O.N. (1979) *Fracture toughness of structural steels*. Moscow, Metallurgiya [in Russian].
5. Ostash, O.P., Gajvoronsky, O.A., Poznyakov, V.D., Kulyk, V.V. (2016) *Method of heat treatment of high-strength low-alloy carbon steels*. Pat. 105440, Ukraine. Publ. 25.03.2016 [in Ukrainian].
6. (1998) *Joint Aviation Requirements*, JAR 25.571.
7. Lozovskaya, A.V., Chajka, A.A., Bondarev, A.A. et al. (2001) Softening of high-strength aluminium alloys in different fusion welding processes. *The Paton Welding J.*, **3**, 13–17.
8. Poklyatsky, A.G., Ishchenko, A.Ya., Grinyuk, A.A. et al. (2002) Non-consumable electrode argon-arc welding of aluminium alloys with arc oscillations. *Ibid.*, **2**, 18–22.
9. Poklyatsky, A.G., Grinyuk, A.A. (2001) Effect of parameters of asymmetric and modulated currents on quality of aluminium alloy welded joints. *Ibid.*, **7**, 33–36.
10. Poklyatsky, A.G. (2001) Peculiarities of formation of macro-inclusions of oxide film in weld metal of aluminium alloys (Review). *Ibid.*, **3**, 36–38.
11. Ishchenko, A.Ya., Lozovskaya, A.V., Sklabinskaya, I.E. (1999) Mechanism of retardation of solidification cracks in welding of aluminium alloys with scandium. *Avtomatich. Svarka*, **8**, 13–16 [in Russian].
12. Thomas, W.M., Nicholas, E.D., Needham, J.C. et al. *Friction stir butt welding*. Int. Pat. PCT/GB 92/02203; GB Pat. Appl. 9125978.8. Publ. 1991.
13. Pietras, A., Zadroga, L., Lomozik, M. (2004) Characteristics of welds formed by pressure welding incorporating stirring of the weld materials (FSW). *Welding International*, **1**, 5–10.
14. Shibayanagi, T. (2007) Microstructural aspects in friction stir welding. *J. of Japan Inst. of Light Metals*, **9**, 416–423.
15. Ishchenko, A.Ya., Poklyatsky, A.G. (2010) *Tool for friction stir welding of aluminium alloys*. Pat. 54096, Ukraine. Publ. 25.10.2010 [in Ukrainian].
16. Ostash, O., Uchanin, V., Semenets, J. et al. (2018) Evaluation of aluminium alloys degradation in aging aircraft. *Research Nondestructive Evaluation*, **29**(3), 156–166.
17. *Standard test method for measurement of fatigue crack growth rates*. ASTM Standards, E647-93.
18. Bussu, G., Irving, P.E. (2003) The role of residual stress and heat affected zone properties on fatigue crack propagation in friction stir welded 2024-T351 aluminium joints. *Int. J. Fatigue*, **25**, 77–78.
19. Aydin, H., Bayram, A., Durgun, I. (2010) The effect of post-weld heat treatment on the mechanical properties of 2024-T4 friction stir-welded joints. *Mater. Des.*, **31**, 2568–2577.

Received 26.10.2018

INVESTIGATION OF PLASMATRON ELECTRIC AND ENERGY CHARACTERISTICS IN MICROPLASMA SPRAYING WITH WIRE MATERIALS

Yu.S. BORISOV, O.M. KYSLYTSIA, S.G. VOINAROVYCH,
Ie.K. KUZMYCH-IANCHUK and S.M. KALIUZHNYI

E.O. Paton Electric Welding Institute of the NAS of Ukraine
11 Kazimir Malevich Str., 03150, Kyiv, Ukraine. E-mail: office@paton.kiev.ua

To determine the range of operating voltages of the plasmatron MP-04 of installation MPN-004 for microplasma spraying, a family of volt-ampere characteristics was plotted, each of which was measured at the constant composition and consumption of the working gas, length of the arc open section and the design dimensions of the plasmatron. The heat flux was determined by the continuous-flow calorimetry method. It allowed under the conditions of microplasma wire spraying to determine the thermal efficiency of the plasmatron, the average-mass initial enthalpy and the plasma jet temperature depending on the plasmatron operation mode: arc current and plasma-forming gas consumption. 12 Ref., 7 Figures.

Keywords: *microplasma wire spraying, wire materials, argon plasma jet, volt-ampere characteristics of plasmatron, temperature and enthalpy of plasma jet, thermal efficiency coefficient, voltage and current of plasma arc, consumption of plasma-forming gas*

As to the type of spraying materials, the technology of thermal spraying (TS) of coatings is divided into powder and wire spraying [1]. The technology of powder TS is distinguished by the variety of types and compositions of spraying materials and possibility of using powders with different granulometric composition. However, it has a number of drawbacks associated with the difficulty in providing the accurate and stable supply of powders into the spraying gas jet, as well as the need in using special powder batchers: complex and expensive devices.

The difference in the size of particles, inherent to all the powders for TS, creates a problem of their non-uniform heating, which influences the quality of coatings. In case of wire TS, by controlling the supply of spraying material (wire), its accurate and stable introduction into the atomizing gas jet and the guaranteed formation of flow of wire spraying molten products are provided. The disadvantage of this process is that the composition of the spraying material is limited by ductile metals. However, recently, the expansion of application of flux-cored wires alleviates this drawback to a certain degree.

In practice, the wire TS is represented by the processes of electric arc metallization, gas flame wire spraying and, in a slightly smaller volume, by plasma TS with the use of «neutral wire» and «wire-anode» spraying systems [2].

The technology of microplasma spraying of coatings (MPS), developed at the E.O. Paton Electric

Welding Institute, used the technology of powder spraying at the first stage. For its realization, a design of a plasmatron was made, characterized by a remote anode and presence of a channel for shielding gas supply, protecting plasma jet [3].

The formation of plasma jet, distribution of temperature values and velocities in its volume, is determined both by the plasmatron operation parameters, as well as by its design. In this connection, when creating a new design of a plasmatron, the necessary stage in the development of a spraying technology with its use is the determination of its main characteristics and the limiting levels of temperatures and velocities of plasma jet. This evaluation is necessary to determine the capabilities of the plasmatron for heating and melting the particles of the spraying material.

When developing the technology of microplasma spraying of coatings using a neutral wire, it was necessary to study the characteristics of the microplasmatron and the microplasma jet, generated by it in the conditions of spraying with wire materials.

The aim of the experiment is to investigate the thermal efficiency of the plasmatron operation η and to determine the average-mass initial enthalpy and temperature of the plasma jet depending on the plasmatron operation modes: arc current I_a and plasma-forming gas consumption $Q_{p,g}$.

Procedure for determining characteristics of microplasmatron for conditions of MPS. Plasmatron is the converter of electrical energy into heat one.

Therefore, on the one hand, the arc of the plasma jet as an element of electrical circuit is characterized by electrical parameters (current, voltage), and on the other hand, as a source of heat, it is characterized by thermal parameters (temperature, heat content). There is a complex relationship between the parameters of the first and the second group.

Enthalpy (ΔH) is the amount of heat contained in a unit of volume or mass of the jet, is an important thermal parameter of the plasma jet. The effect of consumption and composition of working gas on the arc voltage is graphically illustrated by the volt-ampere characteristics of plasmatrons (VAC), representing the dependence between the voltage and arc current at the other equal conditions (arc length, plasmatron parameters, external conditions). In the region of low currents, the VACs of plasmatrons are falling, and with the current growth they pass into independent and rising ones. With an unchanged gas composition, the intensity of all sections of the plasma arc column increases with increasing the degree of its compression. The degree of the arc column constriction is growing (to a certain extent) with a decrease in the forming nozzle diameter and an increase in the consumption of working gas. As investigations show, the gas main mass passes through the peripheral regions of the column and, as the consumption increases, it chills and constricts the column ever more intensively. The more intensively the arc is constricted, the lower the value of the current, at which VAC transfers into rising one. Thus, the plasma arc voltage depends on the design dimensions of the plasmatron, on the arc current, composition and consumption of the working gas [4–6].

To determine the range of operating voltages of the plasmatron, the VAC family is plotted, each of which is taken at change in the consumption of the plasma-forming gas $Q_{p,g}$ and unchanged design dimensions of the plasmatron.

For experiments, the plasmatron MP-04, designed by the E.O. Paton Electric Welding Institute, was used. The measurements were carried out with a channel diameter of the plasma-forming nozzle of 1.0 mm and an electrode diameter of 1.5 mm. The distance from the electrode end to the nozzle edge was 1.0 mm, the distance from the nozzle edge to anode was 1.5 mm. As a plasma-forming and shielding gas, argon was used. The plasma-forming gas consumption changed within the limits of 100–300 l/h. The shielding gas consumption in all the experiments was maintained at 400 l/h.

The losses for heating of the plasmatron parts were evaluated according to the methods described in works [7, 8], according to the value of the heat flux Q_f ,

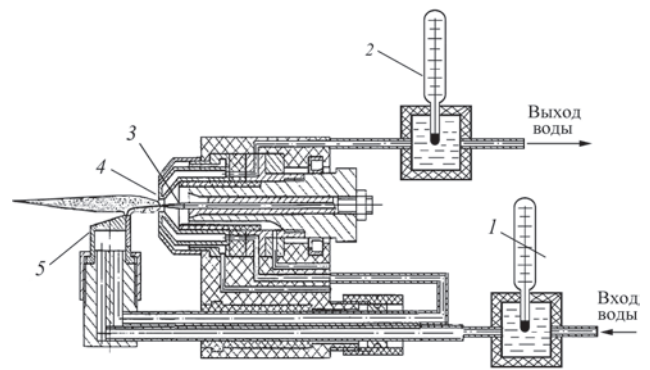


Figure 1. Scheme of experiment for determination of the plasmatron operation efficiency: 1 — thermometer, measuring temperature of water at the inlet to the plasmatron; 2 — thermometer, measuring temperature of water at the outlet from the plasmatron; 3 — cathode; 4 — plasma-forming nozzle; 5 — anode

(J) taken by the water-cooled surfaces of the plasmatron (copper anode, cathode unit and plasma-forming nozzle).

$$Q_f = c\rho Q_w \Delta T, \quad (1)$$

where c is the heat capacity of water, J/(g·K); ρ is the density of water, g/cm³; Q_w — water consumption, cm³/s; ΔT is the difference of water temperature at the inlet and outlet from the calorimeter, °C.

The water consumption through the calorimeter (sections of the calorimeter) was measured by rotameters RS-5, the difference in temperatures ΔT was measured by mercury thermometers with a division value of 0.1 °C.

The heat flux was determined by the method of continuous-flow calorimetry in the experimental installation, the scheme of which is shown in Figure 1.

The thermal efficiency of the plasmatron was calculated from the ratio:

$$\eta = 1 - \frac{P_h}{P_a}, \quad (2)$$

where P_a is the arc power, determined as the product of I_a , U_a , W; P_h is the heat flux power consumed for heating the water-cooled surfaces of the plasmatron (copper anode, cathode unit and plasma-forming nozzle), which is determined by the value Q_f and the heat losses for radiation P_{rad} ; $P_h = Q_f + P_{rad}$.

Assuming that the plasma is optically thin (transparent for its own radiation), the losses on radiation (taking into account that during operation of the plasmatron MP-04 the arc is burning outside the plasmatron body, i.e. between the remote anode and the cathode tip) can be estimated from the formula:

$$P_{rad} = \frac{\pi d^2}{4} l \psi (\bar{T}), \quad (3)$$

where d is the arc column diameter; l is the open arc section length; $(\pi d^2/4)l$ is the plasma volume; ψ is the

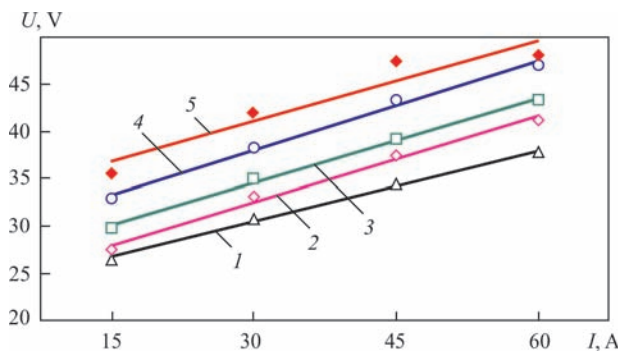


Figure 2. VAC of the plasmatron MP-04 (nozzle diameter is 1 mm, plasma-forming gas is argon, consumption of plasma-forming gas, l/h: 1 — 100; 2 — 150; 3 — 200; 4 — 250; 5 — 300

volume plasma losses for radiation, W/m^3 ; T is the average mass temperature of the plasma, K.

The enthalpy ΔH (J/l) of the plasma jet was determined from the ratio:

$$\Delta H = \frac{P_a \eta}{Q_{pg}}, \quad (4)$$

where Q_{pg} is the consumption of the plasma-forming gas, l/h; η is the thermal efficiency of the plasmatron; P_a is the arc power, J/h.

The jet temperature was determined from the Tables of its relationship with the enthalpy in work [9].

Measurement of VAC of microplasmatron MP-04 during wire spraying. VAC of the plasmatron demonstrates the relation between the voltage of plasma arc and current. VAC allows establishing the range of stable operation of the power source during change in the operation modes of the plasmatron.

The voltage of the plasma arc depends on the design dimensions of the plasmatron (nozzle diameter, nozzle length), arc current, composition and consumption of the working gas and on the value of interelectrode gap.

The main thermal characteristics of the plasmatron are the thermal efficiency of its operation $\eta_{t,o}$, enthalpy ΔH and the temperature of plasma jet.

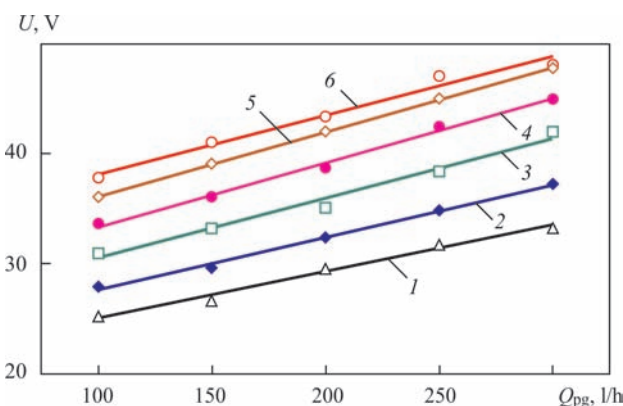


Figure 3. Variation in voltage of the plasmatron MP-04 depending on the consumption of plasma-forming gas at different values of current, A: 1 — 10; 2 — 20; 3 — 30; 4 — 40; 5 — 50; 6 — 60

A calculated evaluation of the influence of parameters of the plasmatron operation mode on the enthalpy of plasma jet was carried out using the expression (4). With the increase in the arc power P_a , the temperature and the enthalpy ΔH of plasma jet increase. The effect of the consumption of plasma-forming gas Q_{pg} is opposite. The arc power is in its turn determined by two parameters: current and voltage.

To determine the range of operating voltages of the plasmatron MP-04, a family of VAC was plotted, each of which was taken at the unchanged composition and consumption of the working gas, length of the arc open section and constant design dimensions of the plasmatron (Figure 2).

The processing of the experiment results shows that VACs of the plasmatron MP-04 are rising and have a linear form. It is known that in most cases the rising VACs are more energetically advantageous, because during the use of power sources they do not require introduction of additional ballast resistance to the circuit, the voltage drop at which can reach 50 % [10]. Thus, the rising VACs of the microplasmatron MP-04 allow using the power sources with both steep-falling external VAC, as well as with rigid external VAC for operation with it [11].

It was established that at a constant «cathode–anode» distance and constant composition of the gas, the voltage increases linearly with increase in current and consumption of plasma-forming gas (Figures 2 and 3), at the same time, the power of plasmatron increases.

The growth in voltage at the increase in working gas consumption can be explained by the increase in the degree of the arc column constriction. During blowing of arc discharge at its boundary due to intense heat exchange between the gas and the arc column, the deionization process takes place, which leads to reduction in the discharge diameter and growth in the electric field intensity in it. The more intensively the arc is constricted, the lower value of current is required for the VAC to go into rising one.

It is seen from the VAC (Figures 2 and 3) that for operating values of current and consumption of plasma-forming gas, the voltage is in the range of 25–50 V. Using the dependence given in work [12], one can assume that the power source for the arc exciting and stable operation of the plasmatron MP-04 at the modes providing spraying of wire materials, should be capable for smooth regulation of current in the range of 20–80 A and the open-circuit voltage of not less than 60 V.

The investigations of thermal efficiency of microplasmatron showed that a change in current from 15 to

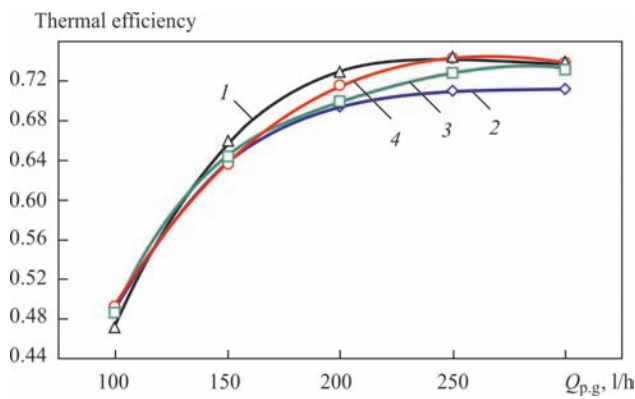


Figure 4. Variation in thermal efficiency of the plasmatron MP-04, depending on the consumption of plasma-forming gas at different values of current A: 1 — 15; 2 — 30; 3 — 45; 4 — 60

60 A in the entire consumption range of plasma-forming gas of 100–300 l/h almost does not result in its change (Figure 4). It was established, that thermal efficiency of the plasmatron grows with the increase in the consumption of plasma-forming gas in the range of 100–200 l/h, and in the range of consumption of 200–300 l/h, the efficiency growth is not observed. This is explained by the balance beginning between the energy, which is taken by the plasma-forming gas and cooling system of the plasmatron, as well as by the beginning of critical conditions, at which the arc constriction is maximum and the losses to the nozzle walls remain at the same level. The maximum efficiency of the microplasmatron MP-04 reaches 75 %, which exceeds the result obtained in the conditions of powder MPS [12].

The carried out investigations showed that the efficiency of the plasmatron MP-04 is almost not changed with a change in the current at the gas consumption, exceeding 100 l/h (Figure 5).

Determination of enthalpy and temperature of argon plasma jet in microplasma wire spraying. During microplasma wire spraying, for improvement of the wire melting conditions and dispersion of the molten metal drop, formed at the end of the neutral

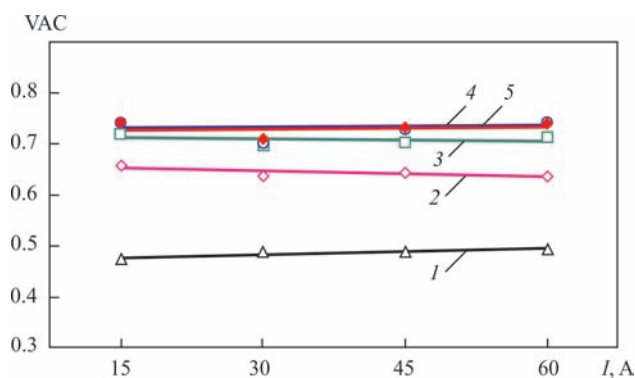


Figure 5. Variation in thermal efficiency of the plasmatron MP-04 as a function of current at different values of consumption of plasma-forming gas, l/h: 1 — 100; 2 — 150; 3 — 200; 4 — 250; 5 — 300

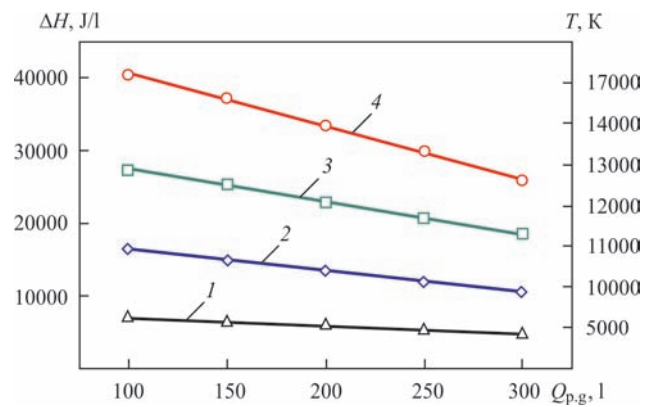


Figure 6. Variation in enthalpy depending on gas consumption for different values of current A: 1 — 15; 2 — 30; 3 — 45; 4 — 60

wire and formation of a jet, containing the particles of the spraying material, an increased gas consumption at a low plasma arc current is used. Therefore, the enthalpy of the plasma jet is much lower than that in microplasma powder spraying. In Figure 6 it is seen that with the increase in gas consumption at a less intensive increase in the jet power, the values of the enthalpy and temperature of the plasma jet are reduced.

The carried out calculation of plasma parameters allowed determining the temperature of microplasma jet from the data of argon temperature dependence on the enthalpy [9]. The maximum temperature of the jet is 17700 K at the minimum gas consumption (100 l/h) and the maximum current (60 A), and the minimum temperature is 5000 K at the maximum gas consumption (300 l/h) and the minimum current (15 A) (Figure 6).

At a fixed voltage, the arc power can be controlled by the more flexible parameter: arc current. The jet enthalpy increases linearly at all the gas consumptions with increase in current and hence, in arc power (Figure 7).

Since the voltage is mainly determined by the design of the plasmatron and the composition of plasma-forming gas, the selection of its operating mode during spraying process consists in establishing the

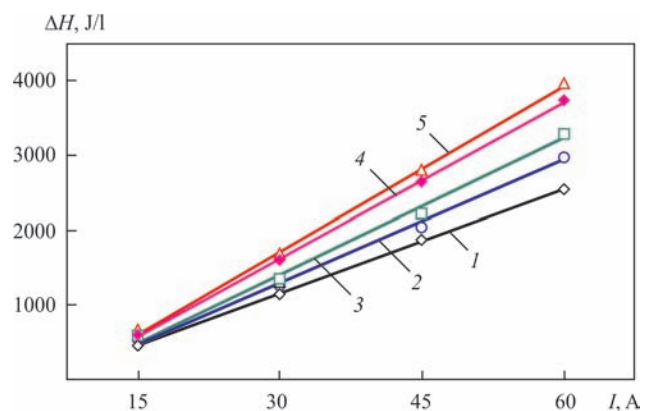


Figure 7. Variation in enthalpy depending on current for different values of consumption of plasma-forming gas, l/h: 1 — 100; 2 — 150; 3 — 200; 4 — 250; 5 — 300

optimal combination of current and consumption of the plasma-forming gas. The lower and the upper level of consumption of the plasma-forming gas is connected with the operating conditions of the microplasmatron (thermal load at the nozzle walls, anode life, process stability).

Conclusions

As a result of measuring the electrical and thermal characteristics of a turbulent microplasma argon jet during spraying the neutral wire, it was established that under these conditions the VAC of a microplasmatron with a remote anode increases linearly in the range of currents of 10–60 A for the consumption of plasma-forming gas of 100–300 l/h, and the efficiency of the microplasmatron is almost independent of the current value and increases from 48 to 73 % with an increase in the plasma-forming gas consumption from 100 to 200 l/h. A further increase in the consumption of the plasma-forming gas to 300 l/h does not lead to a change in the efficiency. The calculated value of the plasma jet enthalpy under these conditions reaches 40 kJ/l, which is equivalent to the argon jet temperature of 17700 K.

1. Yushchenko, K.A., Borisov, Yu.S., Kuznetsov, V.D., Korzh, V.M. (2007) *Surface engineering*. Kiev, Naukova Dumka [in Russian].
2. Bobrov, G.V., Iliin, A.A. (2004) *Deposition of inorganic coatings*. Moscow, Internet Engineering [in Russian].
3. Borisov, Yu.S., Vojnarovich, S.G., Fomakin, O.O., Yushchenko, K.A. (2002) *Plasmatron for spraying of coatings*. Pat. 2002076032, Ukraine, Int. Cl. B23K10/00 [in Ukrainian].
4. Zhukov, M.F., Smolyakov, V.Ya., Uryukov, B.A. (1973) *Electric arc heaters of gas (plasmatrons)*. Moscow, Nauka [in Russian].
5. Korotaev, A.S., Kostilyov, A.M., Koba, V.V. et al. (1969) *Generators of low-temperature plasma*. Moscow, Nauka [in Russian].
6. Donskoj, A.V., Klubnikin, V.S. (1979) *Electroplasma processes and systems in mechanical engineering*. Leningrad, Mashinostroenie [in Russian].
7. Paton, B.E., Gvozdetsky, V.S., Dudko, D.A. et al. (1979) *Microplasma welding*. Kiev, Naukova Dumka [in Russian].
8. Gladky, P.V. (1999) Thermal characteristics of arc of surfacing plasmatrons. *Avtomatich. Svarka*, **6**, 13–15 [in Russian].
9. Engelsht, V.S., Gurovich, V.Ts., Desyatkov, G.A. et al. (1990) *Theory of electric arc column*. Low-temperature plasma. Vol. 1. Novosibirsk, Nauka. [in Russian].
10. Korotaev, A.S. (1980) *Electric arc plasmatrons*. Moscow, Mashinostroenie [in Russian].
11. Borisov, Yu.S., Kharlamov, Yu.A., Sidorenko, L.A., Ardatovskaya, E.N. (1987) *Thermal coatings from powder materials*. Kiev, Naukova Dumka [in Russian].
12. Borisov, Y.S., Sviridova, I., Voynarovich, S. et al. (2002) Investigation of the microplasma spraying processes. In: *Proc. of ITSC, Essen*, 335–338.

Received 10.07.2018

APPLICATION OF ELECTROSLAG WELDING IN CONSTRUCTION

K.A. YUSHCHENKO, I.I. LYCHKO, S.M. KOZULIN, A.A. FOMAKIN and I.S. NESENA

E.O. Paton Electric Welding Institute of the NAS of Ukraine
11 Kazimir Malevich Str., 03150, Kyiv, Ukraine. E-mail: office@paton.kiev.ua

The paper presents the results of experimental studies and engineering developments, which were the base for creating a technology and technique of performance of electroslag welding with consumable nozzle of reinforcing elements of building columns of a high-rise building. Experience of application of the developed technology in construction of a high-rise building is described. New machines and special technological fixture at performance of welding operations under assembly conditions was demonstrated. 15 Ref., 7 Figures.

Keywords: *building columns, girths, reinforcing elements, electroslag welding, consumable nozzle, special technological fixture, assembly conditions, efficiency of welding operations*

One of the specific features of application of welding processes in construction is strict compliance of the terms of welding operations performance with the terms of construction and mounting work. Special requirements are made of welding technologies to ensure simultaneous performance of this work, namely high process efficiency, mobility, higher reliability of welding equipment and its insensitivity to unfavourable (field) conditions of operation, low labour consumption, minimum time consumed by assembly-preparatory operations.

In recent years, a significant growth in the construction of high-rise administrative buildings necessitated application of rolled metal of increased thickness (60 mm and greater) by design institutes for manufacturing all-welded bearing columns. At present the girths of building columns and reinforcing elements of their opening frames are joined by coated-electrode manual or mechanized welding with solid or flux-cored wire, i.e. the methods, which are characterized by high labour consumption and low efficiency for the above thicknesses that significantly prolongs the terms of construction and mounting work.

At the initial stage of construction of basement flooring at erection of high-rise «Community Center» experimental building (Kiev) it became necessary to significantly increase the welding operations efficiency. It was proposed to replace coated-electrode arc welding by electroslag welding, as the most productive method of joining metals of unlimited thickness [1] that was the objective of this work.

Electroslag welding (ESW) was applied for the first time in the USSR at construction of blast furnace jackets, mounting of metal structures of industrial buildings,

large-capacity converters, processing apparatuses for alumina plants, massive water conduits, etc. [1].

Also known is the experience of successful application of ESW in the USA and Japan in fabrication of massive building structures for administrative buildings [2–6]. ESW was applied for making longitudinal butt joints of T- and I-beams in fabrication of heavy building columns [3], as well as joining corner columns with support plates and diagonal braces [5]. Here, the method of consumable-nozzle ESW (CNESW) became the most widely accepted for fabrication of all-welded columns for steel frames of 52–59-storey buildings due to the possibility to weld elements of different thickness from 44 to 73 mm [7]. At present CNESW is widely applied in these countries for joining inner diaphragms 40–150 mm thick to girths of building columns of a rectangular profile [8, 9] at their fabrication under production conditions.

According to Production Project the design of the building columns of 54-storey «Community Center» experimental building under construction resembles the shape of the Maltese cross in its cross-section (Figure 1). It was necessary to weld reinforcing elements 2 (90 mm thickness, 800–1450 mm length) to the opening frames located between the end faces of girths 1 with the purpose of subsequent erection of basement flooring on their base. Column girths were made from new structural steel 06GB-390 (TU U 27.1-05416923-085–2006) 50 mm thick, and reinforcing elements of their opening frames were from steel 09G2S-15 (GOST 19281–89). A feature of steel 06GB is its good weldability, high delayed and cold cracking resistance, compared to the known grades of low-carbon steels of this strength class [10].

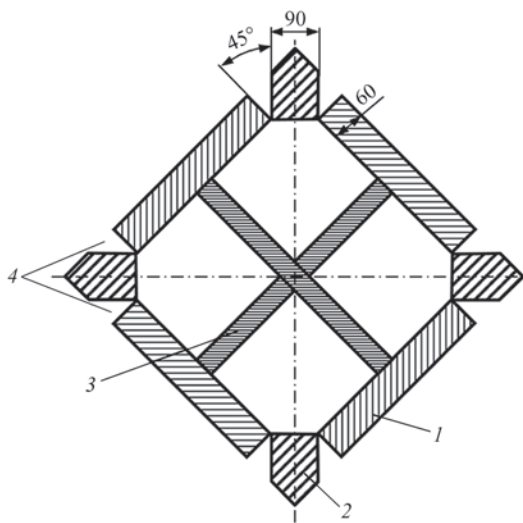


Figure 1. Scheme of butt assembly for welding the reinforcing elements of girths of a building column of Maltese cross type: 1 — cross-section of column girth; 2 — column reinforcing element; 3 — stiffener; 4 — butt welded joint

According to project documentation, a V-shaped groove was specified in the points of welding the reinforcing elements to building column girths, which is designed for performance of multipass electric arc welding in the vertical position (of the order of 300 passes). For application of single-pass CNESW it was necessary to develop a special technology and technique of joining the reinforcing elements to the column.

In connection with the non-standard groove shape, adverse working conditions in the underground space (high humidity, abrasive and cement dust), as well

as complexity of formation of the reverse side of the butt joint, the following problems had to be solved to reach the defined goal:

- develop the technology and technique of ESW performance, ensuring guaranteed fusion of filler metal with base metal, sound formation of weld metal and absence of defects;
- develop and manufacture portable welding machines of higher reliability, where the control systems are protected from possible penetration of moisture and dust, that is characteristic for operation in site conditions. Machine design should provide their fast mounting on the item, as well as dismantling;
- develop special devices for quick mounting of welding machines on building columns;
- develop technological fixture, ensuring sound formation of outer and reverse sides of the electroslag weld, as well as devices for its fast mounting and dismantling, particularly in difficult-of-access sections.

To solve the defined tasks we have conducted design work and experimental studies. CNESW parameters were optimized on full-scale samples, made from the above-mentioned steels, using a DC power source. Sv-08G2S electrode wire and AN-8U welding flux were used as welding consumables. Welding speed was 1.6–2 m/h to reduce the heat input.

Transverse templates were cut out of the welded samples to determine the mechanical properties and chemical composition of welded joints. Microhardness measurements were performed by contact-resonance hardness meter TKR-35. Transverse macrosection of welded joints, scheme and results of hardness measurements are shown in Figure 2, from which one can see that hardness distribution in the studied sections is characteristic for ES welds of analogous steels, not subjected to subsequent heat treatment. Here, considering the sequential performance of adjacent welds, as well as close location of welded-up grooves, one can see from Figure 2, *b* that the heat, evolved when making the second weld, produced partial auto-heat treatment of metal of the previous weld and part of the heat-affected zone (HAZ).

Visual inspection of welded samples after CNESW of V-shaped butt joints is indicative of satisfactory formation of weld surface. Welds are tight, without slag inclusions, pores, lacks-of-fusion or cracks.

Figure 3 shows the results of determination of chemical composition of metal of a column girth, reinforcing element, welding wire and weld, from which it follows that the weld metal composition differs only slightly from that of the steels being welded, and low content of carbon and increased content of manganese in the weld metal ensure a high level of technological strength of the welded joint.

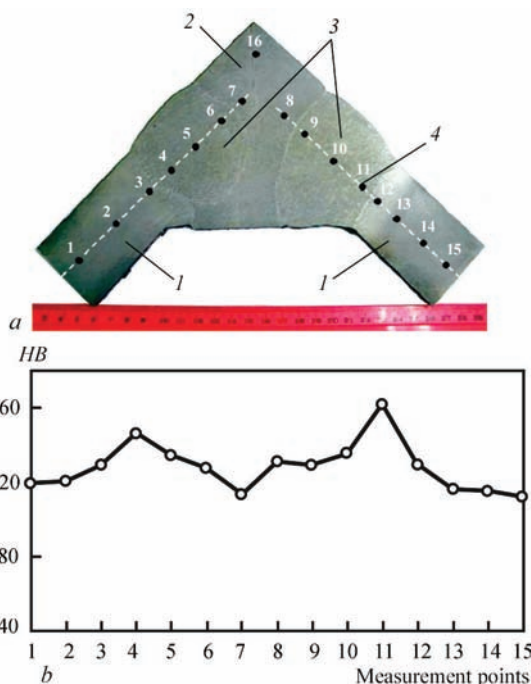


Figure 2. Transverse macrosection, scheme (*a*) and results of measurement of welded joint metal hardness (*b*): 1 — column girths; 2 — reinforcing element; 3 — electroslag welds; 4 — measurement points

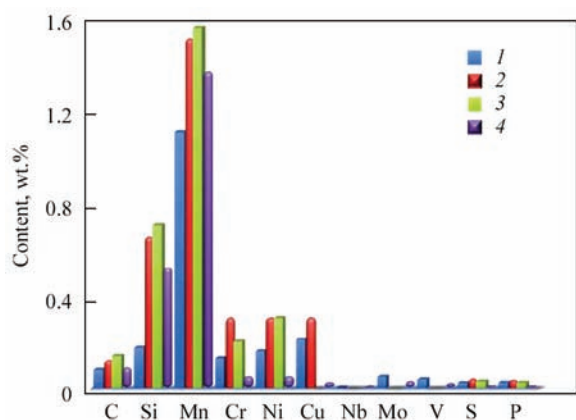


Figure 3. Chemical composition of the metal of girths reinforcing elements, electrode wire and weld: 1 — 06GB; 2 — 09G2S steel; 3 — Sv-08G2S; 4 — weld

Values of mechanical strength of welded joint metal were determined from the side of column girth. Tensile tests of samples showed that ultimate strength value σ_t for metal along the fusion line and in the HAZ at 5 mm distance from the fusion line is equal to $\sigma_t = 466\text{--}480\text{ MPa}$, that is indicative of a sufficient level of welded joint strength at ESW of steels 06GB and 09G2S. Values of impact toughness after testing at the temperature of 20 °C in the as-welded condition for metal along the fusion line and in the HAZ



Figure 4. Fastening A-1304 machines on a building column: 1 — column; 2 — welding machines; 3 — quick-detachable frame

at 5 mm distance from the fusion line are equal to $KCU = 108\text{--}155\text{ J/cm}^2$.

Analysis of the given results of CNESW of butt joints, earlier to be joined by electric arc welding, as well as positive experience of operation at above zero ambient temperatures of welded structures, not sub-

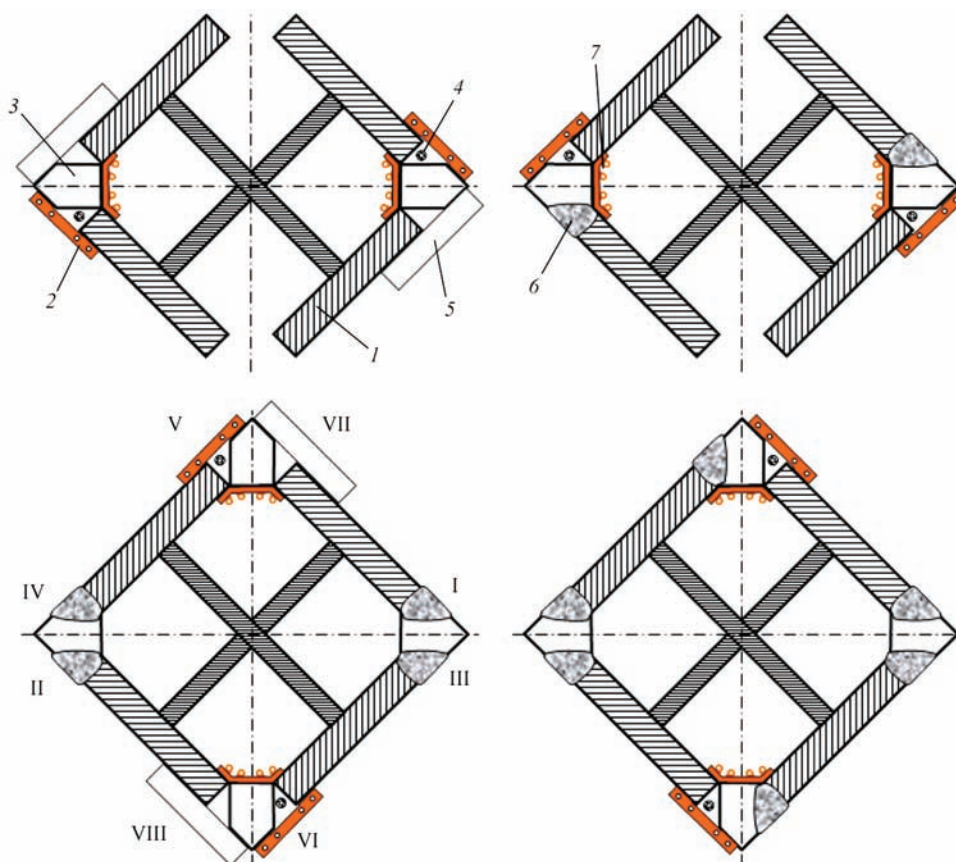


Figure 5. Sequence of assembly and consumable-nozzle electroslag welding of reinforcements of building column opening frames: 1 — column girth; 2 — water-cooled coverplate; 3 — reinforcing element; 4 — consumable nozzle; 5 — technological tab; 6 — weld; 7 — forming coverplate on the reverse side of butt joint; I—VIII is the weld stacking sequence

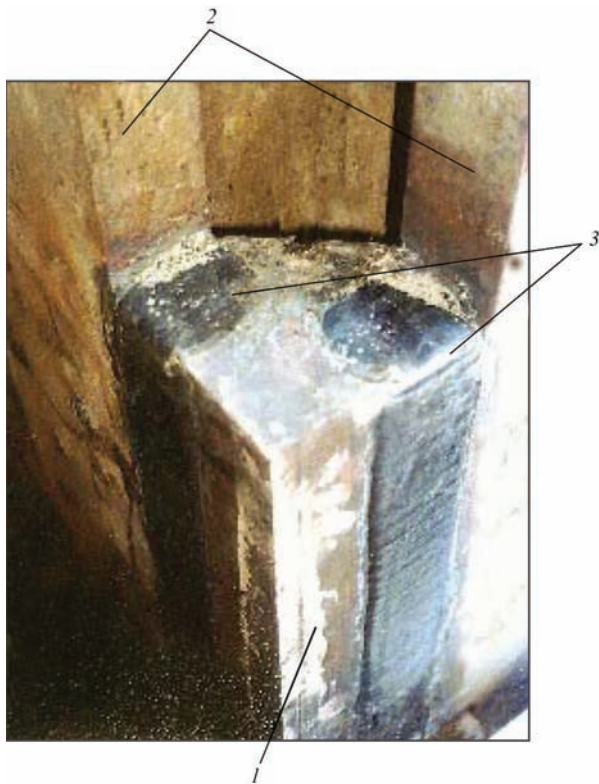


Figure 6. Appearance of electroslag welds after welding-up the shrinkage cavity on their linear part: 1 — reinforcing element; 2 — building column girths; 3 — welds

jected to postweld heat treatment [11], are indicative of technical possibility and rationality of its application for welding the reinforcing elements of opening frames of columns of Maltese cross type.

Considering the short construction time, at the first stage it was proposed to adapt for CNESW batch-produced A-1304UKhLCh welding machines for their application under specific conditions of construction work performance in underground premises. A special quick-detachable frame (Figure 4) was developed and manufactured for fastening the machines on the columns. It allows quickly mounting and dismantling the systems after welding the butt joints.

Reliable containment of the slag and metal pools in the gap is provided by copper water-cooled devices from the outer and reverse sides of the welded butt joint [1]. Nonstandard shape and dimensions of the groove, as well as difficult access for servicing the reverse side of the butt joint (Figure 1), required application of forming devices of a special design. Customized technological fixture was developed and manufactured to ensure sound fusion of filler metal with base metal and satisfactory weld formation, namely water-cooled forming devices and fixtures for their quick fastening on the item being welded [12, 13].

In order to lower the level of residual welding stresses, welding of eight butt joints on each column was performed with simultaneous application of two



Figure 7. Fragment of consumable-nozzle electroslag welding of reinforcements of opening frames of building columns using ASHP 113M2 machines (a) and appearance of welds (b)

welding machines and with specific stacking order of welds at higher welding speeds (Figure 5).

Considering the prohibition for oxy-fuel cutting application at construction of the above building, as well as to reduce the welding time and save welding consumables, a technological measure was implemented, resulting in maximum reduction of the size of the crop parts of welds by welding-up the shrinkage cavity on the welded butt joint linear part (Figure 6).

After transfer of the developed technology to Ukritarm Company (Kiev) and training its personnel in the technique of CNESW performance, the latter performed welding of reinforcing elements of opening frames on eight columns (64 butt joints) in construction of the flooring of the first basement storey. However, during performance of the above work, some problems were encountered in operation of A-1304 machines. A large weight of the machines greatly increased the labor consumption and time for assembly-preparatory operations. The electric components of the machines failed periodically, because of the high humidity and dustiness of the locations of welding operations performance. To solve the above problems, PWI developed portable ASHP 113M2 machines for CNESW with two electrode wires in site,

which is devoid of the above drawbacks [14]. Two pilot-production AShP 113M2 machines were manufactured and transferred to the customer for welding operations performance in the object under construction. New machines were used to successfully weld more than 1500 butt joints (more than 1250 run. m of welds) in construction of eight basement storeys (Figure 7) [15]*. Ultrasonic testing of welded joints did not reveal any defects in the form of cracks, pores, lacks-of-fusion, etc.

Conclusions

1. Technology and technique for performance of CNESW of reinforcing elements of building columns opening frames were developed, which provide guaranteed fusion of filler metal with base metal, sound formation of weld metal and absence of any defects. Labour consumption of assembly-preparatory and welding operations was essentially reduced, process efficiency was increased by more than 20 times, compared to coated-electrode manual welding, and production standards were improved.

2. Application of new portable AShP 113M2 machines ensured their trouble-free operation under the conditions of high humidity and presence of cement dust during the entire cycle of welding operations.

3. Application of developed special technological fixture ensured reliable containment of slag and metal pools in the welding gap, also in difficult-of-access sections, and allowed an essential reduction of labour consumption of assembly-preparatory operations.

4. New technology and equipment can be recommended for welding in site of massive building columns, thick-walled tanks and other metal structures, operating at positive ambient temperatures.

1. (1980) *Electroslag welding and surfacing*. Ed. by B.E. Paton. Moscow, Mashinostroenie [in Russian].

2. Magic, T., Hampton, Y.A. (1967) Electroslag welding with consumable guide on the Bank of America World Headquarters Building. *Weld. J.*, 47(12), 936–946.
3. Baigent, W.W. (1972) Inescapable in heavy columns: Close work high deposition. *Weld. Des. and Fabr.*, 45(5), 39–42.
4. Hannahs, J., Lea, D. (1970) Where to consider electroslag welding. *Metal Prog.*, 98(5), 62–64.
5. (1973) Massive building calls for massive welds. *Weld. Des. and Fabr.*, 46(8), 47.
6. (1965) *Method of production of round columns using electroslag welding*. Pat. 24811, Japan [in Russian].
7. (1962) Electroslag welding process attains production status. *Can. Mach. and Metalwork*, 73(8), 128.
8. Janice, J., Chambers, Brett R. Manning (2016) Electroslag welding: From shop to field. *Structure Magazine*, February, 20–23.
9. Takahiko Suzuki, Takumi Ishii (2017) Guidebook for preventing brittle fractures of inner diaphragm electroslag welds. *Steel Construction Today & Tomorrow*, 52, 9–12.
10. Sineok, A.G., Demchenko, Yu.V., Proskudin, V.N. et al. (2015) Substantiation of economic efficiency for application of different welding methods and steels for repair of blast furnace jacket No. 4 PJSC MK Azovstal. *Svarshchik*, 4, 18–21 [in Russian].
11. Trufyakov, V.I., Dvoretzky, V.I., Mikheev, P.P. et al. (1990) *Strength of welded joints under alternating loads*. Ed. by V.I. Trufyakov. Kiev, Naukova Dumka [in Russian].
12. Kozulin, S.M., Podima, G.S. (2016) Device for weld formation in difficult-of-access areas of thick-wall metal structures. In: *Proc. of 5th All-Ukrainian Sci.-Pract. Conf. of Students, Postgraduate Students and Junior Scientists on Applied Geometry, Design, Objects of Intellectual Property and Innovation Activity of Students and Junior Scientists*. Kyiv, *DIYa*, 5, 127–131 [in Ukrainian].
13. Kozulin, S.M., Podyma, G.S. (2018) Forming devices for electroslag welding of reinforcement elements of building column openings. In: *Proc. of 5th All-Ukr. Sci.-Pract. Conf. of Students, Postgraduate Students and Junior Scientists on Applied Geometry, Design, Objects of Intellectual Property and Innovation Activity of Students and Junior Scientists*. Kyiv, *DIYa*, 7, 62–66 [in Russian].
14. Yushchenko, K.A., Lychko, I.I., Kozulin, S.M. et al. (2012) Portable apparatus for consumable-nozzle electroslag welding. *The Paton Welding J.*, 8, 45–46.
15. Ukritarm.com.ua/

Received 27.07.2018

*B.V. Tsybulenko, V.G. Yarmak, G.S. Shulzhenko, V.A. Dakal, E.S. Oganisyan, V.A. Kharchenko.

EFFECT OF ALLOYING CHARGE AND EXTERNAL MAGNETIC FIELD ON STRUCTURE AND PROPERTIES OF DEPOSITED METAL

V.V. PEREMITKO, V.L. SUKHOMLIN, O.L. KOSINSKAYA and A.I. PANFILOV

Dniprovsk State Technical University

2 Dneprostroevskaya Str., 51918, Kamenskoe, Ukraine. E-mail: welding@dstu.dp.ua

Effect of inducing the external magnetic field in arc surfacing over preliminary deposited alloying charge (carbon-containing fibers + SiO₂) on hardness and structure of metal, as well as on change in the above-mentioned indices within the limits of single beads was investigated. It was found that the carbon-containing fibers applied to the part surface being deposited cause during surfacing the local enrichment with carbon of a liquid phase, which is decayed in cooling for ferrite-carbide mixture, that leads to the increase in metal hardness. Additional inducing the external magnetic field in process of surfacing promotes intensive stirring of weld pool that results in producing the more uniform structure and hardness. The analytical dependencies of hardness of deposited layers on amount of carbon-containing fibers, SiO₂ + Fe and magnetic field induction were obtained. The results of investigations can be used in development of technology for manufacture and restoration of parts operated under the abrasive wear conditions. 9 Ref., 1 Table, 10 Figures.

Keywords: *submerged-arc surfacing, carbon-containing materials, modifying components, external magnetic field, deposited metal, hardness, microstructure*

Submerged electric arc surfacing over the alloying charge is one of the simplest and most economical methods to produce wear-resistant layers on the surface of parts, operated under the conditions of different types of abrasive wear [1–3]. It is also known

that using this method of surfacing, the producing of deposited metal of a preset and homogeneous chemical and microstructural composition depends to the greatest extent on the mode of surfacing, chemical and fractional composition of alloying charge, over which the surfacing is performed [4, 5].

The aim of this work was the improvement of this method of surfacing by the use of carbon-containing and modifying materials as the alloying charge. As the basis the scheme of arc surfacing of high-carbon coatings over the layer of charge was taken, where it was used in the form of carbon fibers [6]. Additionally, in order to improve the chemical and structural homogeneity of the deposited metal, the effect of an external magnetic field on this parameter was investigated, which according to some data [7, 8] has a positive effect on these properties.

In the course of experiments, the carbon fibers 3 were preliminarily put on the surface deposited in strips (Figure 1). During surfacing, the electrode wire was placed so that the depositing bead 2 overlapped the carbon-containing strip approximately by 25–35 %.

As a material, which fixes the placement of carbon fibers (2–4 fibers T 700SC Torey per the bead) on the surface deposited, a primer-based mixture was used, to which iron powder (15–25 wt.%) and aerosil (0.6–1.2 wt.%) were added. The layout of carbon-contain-

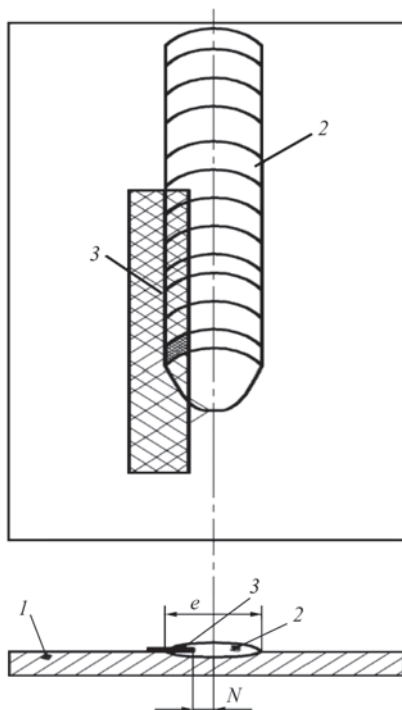


Figure 1. Scheme for the introduction of additional materials: 1 — specimen; 2 — deposited bead; 3 — carbon-containing material; N — displacement; e — bead width

Effect of amount of carbon-containing fibers and magnetic induction on deposited metal hardness

No. of specimen	Induction B , mT	Amount of $\text{SiO}_2 + \text{Fe}$, %	Amount of fibers n , pcs	Hardness, HRC^*		
				1	2	3
1	60	1.2	2	18.0	21.0	16.0
2	60	0	2	24.1	25.0	21.9
3	0	1.2	2	24.8	26.2	22.5
4	0	0	2	17.5	20.1	15.2
5	30	0.6	2	22.5	23.8	20.7
6	60	0.6	4	28.7	30.0	26.5
7	60	0.6	0	21.2	22.0	18.8
8	0	0.6	4	23.0	24.5	21.2
9	0	0.6	0	15.0	16.5	14.0
10	30	0.6	2	22.5	24.1	20.3
11	30	1.2	4	26.4	29.0	24.2
12	30	1.2	0	19.0	20.2	16.9
13	30	0	4	24.0	26.0	22.0
14	30	0	0	18.0	18.3	15.7

*Places of hardness measurements (see Figure 3).

ing fibers on the surface deposited is shown in Figure 2.

In the experiments on surfacing, the automatic welding machine ADS-1000 with the rectifier VDU-506 was used. The surfacing was performed with the wire Sv-08A of 3 mm diameter under the flux AN-348A at a direct current of reverse polarity. The surfacing mode: current is 400–420 A, arc voltage is 32–36 V, wire feed speed is 160 m/h, surfacing speed is 12–16 m/h, pitch is 6–8 mm. The material of the specimens is steel 09G2S (hardness as-delivered is HB 128–143). In order to induce the external magnetic field, a special coil was used, which was fixed on the torch nozzle of the automatic machine ADS-1000. The coil was supplied by direct current.

During the experiments, the second order central noncompositional planning for three factors was performed: the concentration of $\text{SiO}_2 + \text{Fe}$, the amount of introduced carbon-containing fibers and induction of external magnetic effect. From the deposited beads the specimens were cut out to investigate the microstructure and hardness.

Based on the obtained data, the highest values of hardness of the deposited metal are fixed at the periphery of the deposited beads, an expressive maximum is observed at the magnetic induction $B = 60$ mT; $\text{SiO}_2 + \text{Fe}$ — 0.8–1.0 wt. %; n — 4 pcs (see Table and Figure 3).

The processing of the experimental data was carried out using the program STATISTICA 6.0 (Figures 4 and 5). Having compared the diagrams shown in Figures 4 and 5, it can be concluded that at the point 2 (the place, where additional materials were applied) at the same modes of surfacing, the increase in the hardness HRC by 8–10 units is observed.



Figure 2. Scheme for the introduction of additional materials: 1 — deposited bead; 2 — carbon-containing fibers fixed by the primer before surfacing

With the increase in the number of carbon-containing fibers and magnetic induction, the hardness of the weld metal also increases. However, as the practice shows, at the magnetic induction values higher than 70 mT, the pores appear due to intensive stirring of the molten metal pool. The equation, describing the influence of all factors, has a form:

$$HRC = 14.17 + 0.14[c] + 2.72[\text{SiO}_2] + 2.57B - 2.03[\text{SiO}_2]^2 + 0.1B^2 + 0.0027[c][\text{SiO}_2] - 0.035[c]B + 0.49[\text{SiO}_2]B,$$

where $[c]$ is the number of carbon-containing fibers in the deposited layer, pcs; $[\text{SiO}_2]$ is the concentration of aerosil, wt. %; B is the induction of magnetic field, mT.

Figure 6 shows the diagrams of changes in the hardness of metal on the deposited bead according to the traditional scheme of surfacing and that used in the investigations.

Thus, when adding additional materials in the form of aerosil and carbon-containing fibers T 700Sc Torey, 1.5–2.0 times increase in the hardness is observed, the highest hardness is fixed at the periphery of the beads.

After measuring the hardness, the analysis of microstructures was carried out. Figures 7–9 show the microstructures of specimens 1, 3, and 6 in the zones 1, 2, and 3 (see Figure 3 and Table). Comparing the structure of specimens 1 and 3 in the zone 1, it is possible to note a noticeable refining of both ferritic component, as well as the areas with the ferrite-cementite mixture.

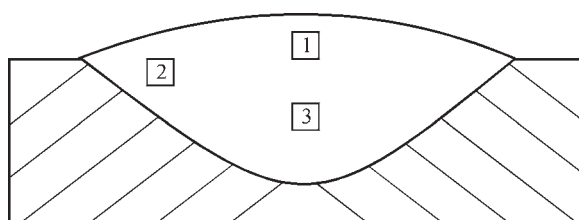


Figure 3. Scheme for measuring hardness of the deposited bead

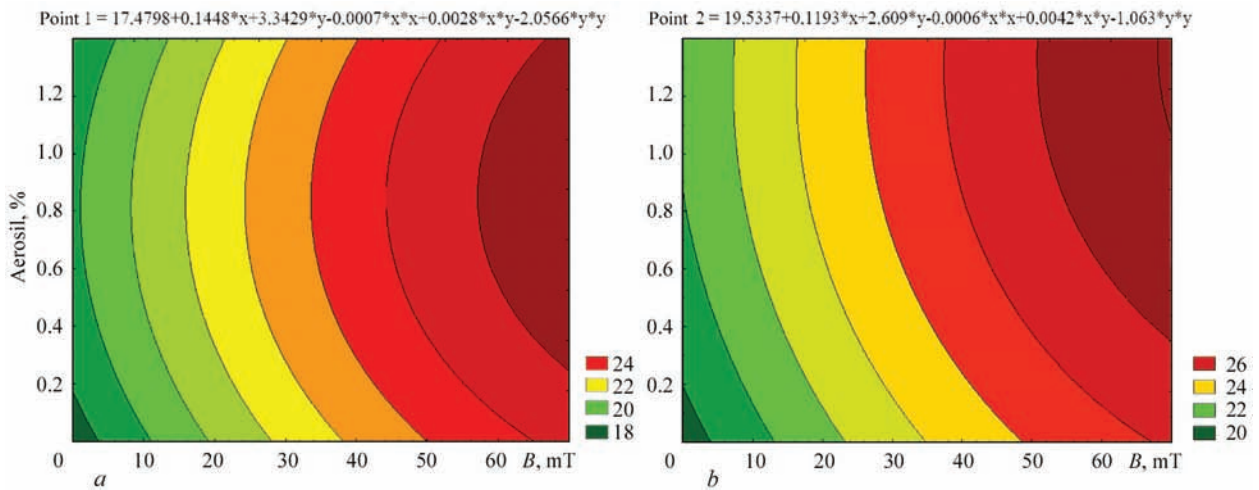


Figure 4. Dependences of hardness (*HRC*) at the points 1 (*a*) and 2 (*b*) on the amount of aerosil and magnetic induction value

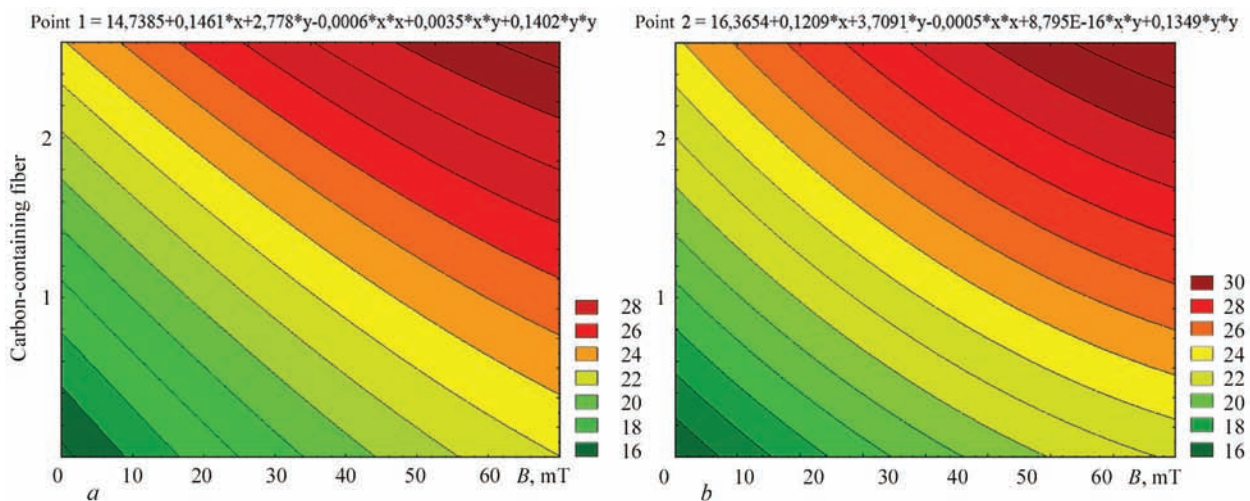


Figure 5. Dependences of hardness (*HRC*) at the points 1 (*a*) and 2 (*b*) on the amount of carbon-containing fibers and magnetic induction value

In the specimen 1, the size of quasi-polygonal grains of ferrite is 20–40 μm, and in the specimen 3 it is 10–30 μm. The grains of ferrite-cementite mixture have a size of 40–60 μm in the specimen 1 and 30–40 μm in the specimen 3 (Figure 7, *a, b*).

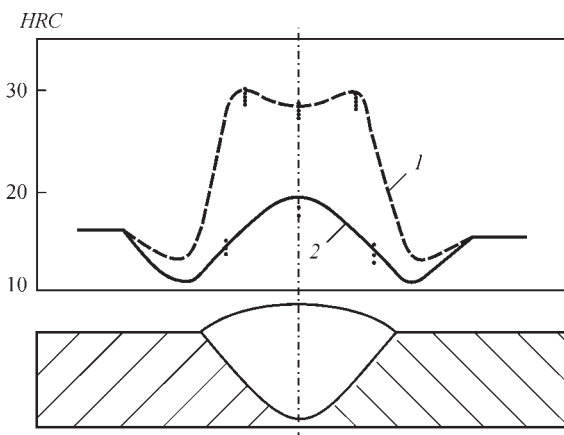


Figure 6. Diagrams of changes in the hardness of deposited bead metal: 1 — with the introduction of additional materials; 2 — without introduction of additional materials

Such refining of structural elements in the specimen 3 is explained by the influence of an external magnetic field during arc surfacing [8]. The additional stirring of the molten metal in a pool facilitates the growth of cooling rate, and, therefore, increases the degree of overcooling during solidification and refining of all the structural components.

In the zone 2, the formation of a structure is influenced not only by carbon-containing fibers and aerosil, but also by an intense heat removal to the base metal. Under its influence, the primary ferrite partially changes its morphology: the acicular ferrite appears in the structure [9]. Also under the effect of a directional heat removal the ferrite-cementite mixture acquires a noticeably elongated shape. The pearlitic structures are formed in the form of thin interlayers between the laths of acicular ferrite or in the form of coarse grains of a quasi-eutectoid. The ferritic formations in zone 2 of the specimen 1 have a width of 30–40 μm and are elongated by 150–200 μm, in the specimen 3 they are elongated, respectively by 15–20 μm and 80–150 μm.

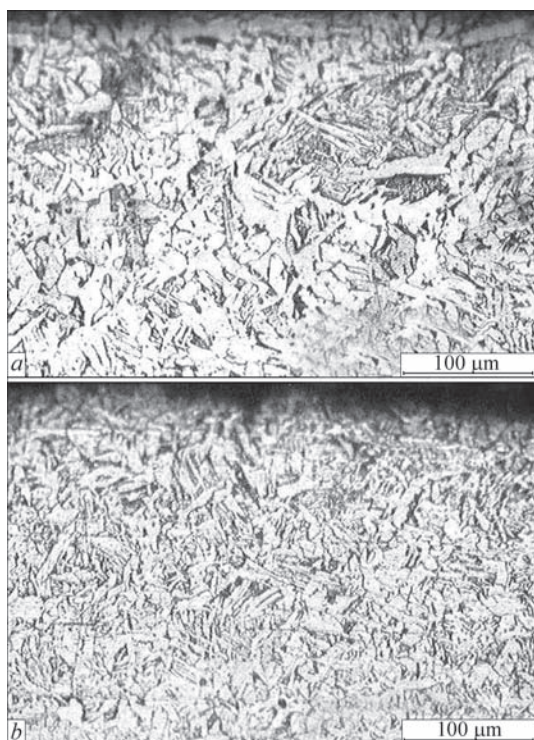


Figure 7. Microstructure of specimens 1 (*a*) and 3 (*b*) in the zone 2

The factor of the magnetic field (for the specimen 3) facilitates stirring of weld pool metal and a more uniform distribution of SiO_2 particles, which play the role of a modifier of the second type, increasing the amount of solidification centers, and the carbon-containing fibers in the zone 2 supply carbon for the formation of a carbide phase. These two factors not only facilitate the refining of the final structure, but also increase the fraction of ferrite-cementite mixture in the specimen 3 (Figure 8, *a*, *b*). The hardness in this zone is maximum.

In the zone 3 of the specimen 1, the lowest hardness is noted. Without additional magnetic effect, the formation of gradient structures occurred almost without the participation of aerosil SiO_2 particles. The width of the ferritic areas in this zone is 25–35 μm , the length is 180–250 μm . The areas of the ferritic-pearlitic mixture have a width of 50–80 μm and a length of 250–300 μm . The width of the acicular ferrite lath is 20–40 μm at an average length of up to 90 μm .

The structure of specimen 3 in the zone 3 was formed with the participation of SiO_2 particles and an external magnetic field. In this zone, the width of the ferritic areas in the structure of columnar crystallites reaches 20–35 μm with a length of 140–180 μm , the width of the areas of ferritic-pearlitic structure is 35–50 μm with a length of 200–230 μm . The width of the acicular ferrite lath is 15–20 μm at an average length of up to 45–70 μm (Figure 9, *a*, *b*).

In the specimen 6, unlike the specimen 3, twice lower content of SiO_2 and twice higher content of

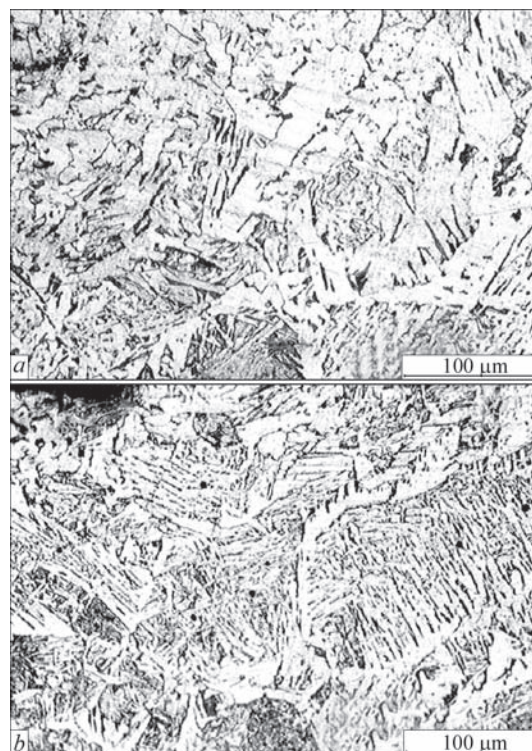


Figure 8. Microstructure of specimens 1 (*a*) and 3 (*b*) in the zone 2

carbon-containing fibers were used. First of all, these changes affected the zone 1. The structure in this zone, due to a smaller amount of modifier, intensive stirring by a magnetic field and additional amount of carbon, has a uniform distribution of quasi-polygonal ferrite areas of 20–30 μm in size, grains of ferrite-cementite mixture with sizes of 35–55 μm and acicular ferrite at a width of the lath being 10–20 μm and a length of 30–55 μm .

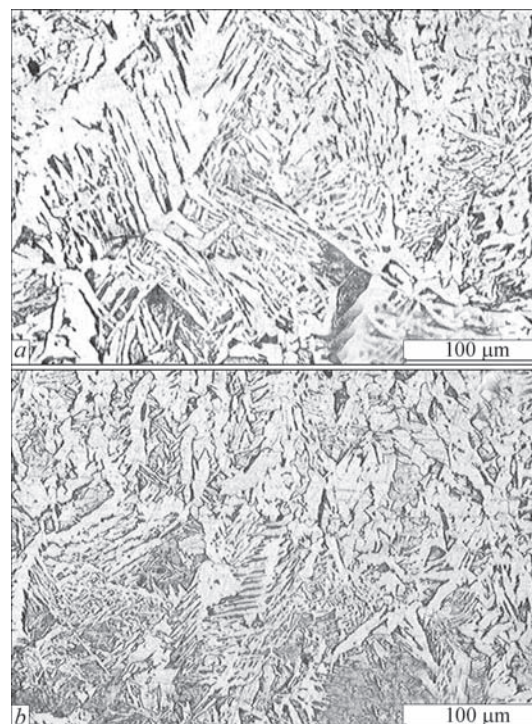


Figure 9. Microstructure of specimens 1 (*a*) and 3 (*b*) in the zone 3

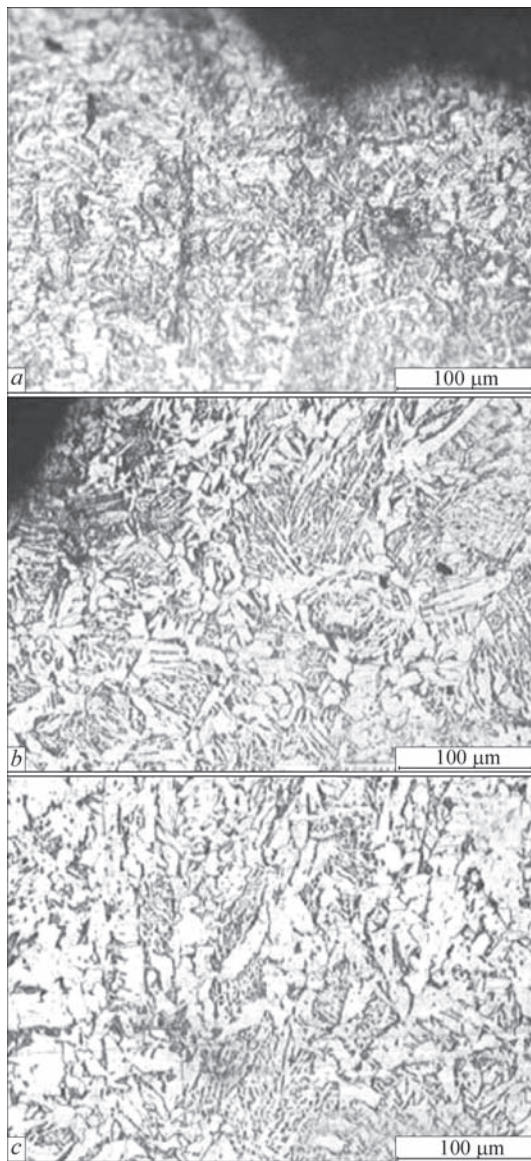


Figure 10. Microstructure of specimens 1 (a) and 3 (b) in the zone 3

A large total volume of ferritic-carbide mixture (up to 50 %) in combination with acicular ferrite (up to 20 %) contributed to an increase in the hardness *HRC* of the specimen in the zone 1 by 3.9 units as compared to the specimen 3. In the zones 2 and 3, the increase in hardness is also predetermined by the refining of both the ferritic component of the structure, and the areas of the quasi-eutectoid and the acicular ferrite laths, which led to higher *HRC* values among all the specimens (Figure 10, a–c).

Conclusions

1. The analytical dependences were proposed to determine the hardness of deposited layers on the number of carbon-containing fibers, previously applied on the surface deposited, the concentration of $\text{SiO}_2 + \text{Fe}$, and the external magnetic field induction.

2. It was established that carbon-containing fibers applied on the parts surface deposited cause a local carbon enrichment of the liquid phase during surfacing, which decomposes into a ferritic-carbide mixture during cooling, thus leading to an increase in the hardness of the metal. The additional inducing of external magnetic field in the process of surfacing promotes an intensive stirring of the weld pool, which results in a more uniform structure and hardness of the deposited metal.

3. The use of aerosil SiO_2 as a modifier is the most justified in the combination with the inducing of an external magnetic field during surfacing. The hardness of metal after using this technology is increased in the near-surface area of the deposited metal by about 20 %.

4. The obtained results can be used in the development of technology of surfacing the parts operated under the conditions of intensive abrasive wear.

1. (2002) *Restoration and improvement of wear resistance and service life of machine parts*. Ed. by V.S. Popov. Zaporozhie, OJSC Motor Sich [in Russian].
2. Peremitko, V.V. (2014) Wear-resistant arc surfacing over the layer of alloying charge. *The Paton Welding J.*, **8**, 54–57.
3. Kuznetsov, V.D., Stepanov, D.V. (2015) Wear-resistant surfacing with feeding of nanopowders in welding pool. *Ibid.*, **5-6**, 47–51.
4. Frumin, I.I. (1961) *Automatic electric arc surfacing*. Kharkov, Metallurgizdat [in Russian].
5. Ryabtsev, I.A., Senchenkov, I.K. (2013) *Theory and practice of surfacing works*. Kiev, Ekotekhnologiya [in Russian].
6. Savulyak, V.I., Zabolotny, S.A., Shenfeld, V.J. (2010) Surfacing of high-carbon coatings using carbon fibers. *Problemy Trybologii*, **1**, 66–70 [in Ukrainian].
7. Razmyshlyayev, A.D. (2000) *Magnetic control of weld formation in arc welding*. Mariupol, PSTU [in Russian].
8. Ryzhov, R.M., Kuznetsov, V.D. (2010) Magnetic control of welded joints quality. Kyiv, Ekotekhnologiya [in Ukrainian].
9. Bolshakov, V.I. (2015) Acicular ferrite. *Visnyk Prydnipr. Derzh. Akademii Budivnytstva ta Arkhitektury*, **9**, 10–15 [in Russian].

Received 02.07.2018

CONTROL OF THE PROCESS OF BASE METAL PENETRATION AT END FACE ELECTROSLAG SURFACING IN CURRENT-SUPPLYING MOULD*

V.G. SOLOVIOV and Yu.M. KUSKOV

E.O. Paton Electric Welding Institute of the NAS of Ukraine
11 Kazimir Malevich Str., 03150, Kyiv, Ukraine. E-mail: office@paton.kiev.ua

In the absence of discrete filler of a certain chemical composition, there appears the task of performing end face electroslag surfacing with large-section electrodes. Here, one of the main surfacing quality characteristics is achieving the minimum and uniform penetration of the base metal. Main principles of design of the system of automatic regulation of these parameters at end face electroslag surfacing in a current-supplying mould were developed. Schemes of control of current distribution in the current-supplying mould are proposed, which allow regulation of the process of electrode melting, and, thus, indirect control of the quality of base metal penetration. A particular scheme should be used to produce a sound bimetal joint with provision of regulation of the position of remelted electrode end face in the slag pool relative to the current-supplying section of the mould and maintaining the calculated heat level of the slag pool. 9 Ref., 7 Figures.

Keywords: automation, regulation, penetration, end face electroslag surfacing, current-supplying mould, electrode, conductivity

A method of electroslag surfacing (ESS) in a current-supplying mould (CSM) developed at the E.O. Paton Electric Welding Institute to the largest extent shows its advantages at melting of different type discrete filler materials in a slag pool [1]. Nevertheless, in a series of cases, for example at absence of filler with specific composition, difficulty and high price of its manufacture as well as with the availability of the billets, which can be used for relatively simple manufacture of the remelted electrodes, there is a task to carry out ESS, in particular end face, with large-section electrodes. Moreover, the practice showed that such a method of surfacing under certain conditions allows achieving increased process efficiency with providing its high quality.

Technologies of ESR with canonic electrode-bottom plate monofilar diagram of connection to power source are well studied and in the majority automated [2, 3] in contrast to ESS using end face electroslag surfacing in CSM with upper current-supplying section. One of the main index of surfacing quality is production of minimum and uniform penetration of base metal. This paper is dedicated to development of the basic principles of design of a system for automatic regulation of these indices in end face ESS with large section electrode.

The synergy principles of synthesis [4], stabilizing relationship between the variables of process states are used more often in the recent time for automation of the dissipative systems, to which ESS is referred. Thus, it is possible to achieve degeneration of the dynamic equations of ESS process and presence of integral invariants of manifolds in the space of its states. The invariant manifolds present themselves «some functions, which do not change during movement». Such approaches to automation of the nonlinear objects significantly simplify synthesis of the system. The processes taking place in the mould during electroslag surfacing are determined by number of factors, which in most cases cannot be controlled by operator all the time using the equipment and being evaluated by his/her intuition. Moreover, the level of reliability of such evaluation depends on operator experience. Therefore, for solution of the problem of automation of surfacing process in CSM it is necessary to find the possibility of indirect estimation of the values of parameters, necessary for automation, analyzing electrotechnical processes in the mould and current-supplying circuits.

Large effect on repeatability of the surfacing results can have not only modes and technique of electroslag process itself, but also variation of electrical parameters of the electric circuits out of mould working zone. In particular, length and location of cables influence characteristics of surfacing process. For example, in the case with ESS in CSM of 200 mm diameter at up

*In discussion.

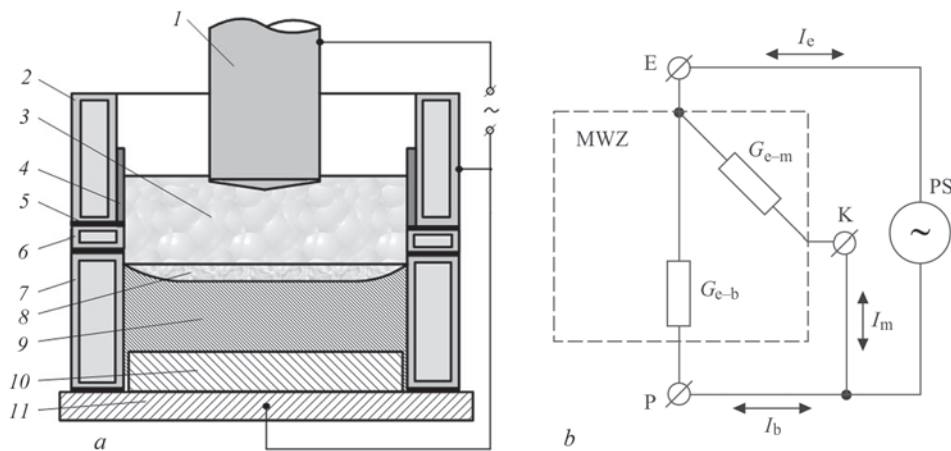


Figure 1. Scheme of ESS in CSM: *a* — with one power source (*I* — electrode, 2, 6, 7 — current-supplying, intermediate and forming sections of mould, respectively; 3 — slag pool; 4 — safely lining; 5 — insulating lining; 8 — metallic pool; 9 — deposited metal; 10 — product; 11 — bottom plate); *b* — electric equivalent diagram (PS — power source with rigid characteristic; E, K and P are terminals of electrode connection to current-supplying section of mould and bottom plate, respectively; I_e , I_m and I_b — current passing through electrode, current-supplying section of mould and bottom plate, respectively; G_{e-m} and G_{e-b} — electric conductivity between terminals E and K as well as E and P, respectively)

to 3 kA currents and cable lengths around 10 m the voltage drop at them can reach 15–25 V. Besides, it is necessary to take into account presence of «valve-like effect» in a slag pool [5], which introduces nonlinearity and deteriorates shape of sine wave in connection of alternating current power sources [6, 7]. The same effect shall be considered when selecting polarity of connection of direct current sources to the mould.

Layout of electrical diagram of CSM connection. Figure 1 presents the diagram of ESS in CSM with one power source and its electrical equivalent diagram.

There is a possibility of automatic control of electric parameters of current-supplying elements, which determine a mould working zone (MWZ), i.e. current-supplying section of the mould, slag pool, electrode and bottom plate. It is necessary to measure voltage between the electrode and current-supplying section of the mould U_{e-m} , electrode–bottom plate U_{e-b} , current-supplying section of the mould and bot-

tom plate U_{m-b} , mould current I_m , electrode current I_e and bottom plate current I_b . However, indicated parameters themselves are not representative in order to characterize the process. There is a need in more generalized, complex parameters having higher correlational relationship with processes taking place in the mould working zone, which are «integral invariants of manifolds» of occurring thermodynamic and electrochemical processes in MWZ.

Independent on connection diagram of the source (sources) to current-supplying elements of the working zone in accordance with Kirchhoff’s first law one of the currents (sum current, marked as I_{sum}) will be always determined by sum of two other currents (component currents, marked as I_{com}).

For example, if I_e is I_{sum} , then I_m and I_b are I_{com} . Based on such presentation of electrical connections of inputs and outputs of the working zone it is possible to talk about the parameters, which to some extent characterize the internal processes in the mould, namely this is electrical conductivity of inner channels of the mould working zone along the channels that refer to I_{com} . In our example these are conductivities $G_{e-m} = I_m/U_{e-m}$ and $G_{e-b} = I_b/U_{e-b}$ (Figure 1, *b*). Naturally, that current directions are not considered here and values of currents and voltages are taken by modulus. Figure 2 shows a vector field of electric intensity and field of equipotential surfaces in MWZ in a two-coordinate presentation, obtained by means of electrostatic modelling [8] in PDETool MatLab medium. The image demonstrates division of the electric current flow, passing from the electrode on two passes (conventional inner channels of MWZ) — electrode–current-supplying section of the mould and electrode–bottom plate.

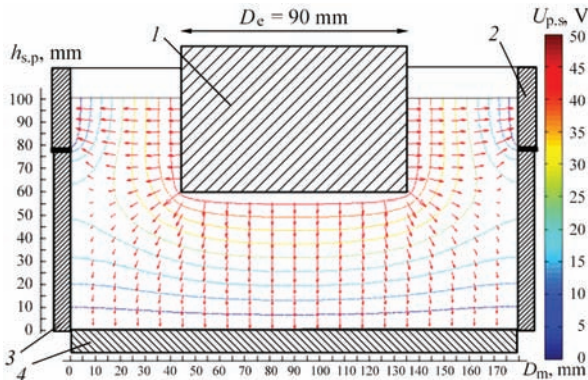


Figure 2. Vector field of electric intensity and field of equipotential surfaces in MWZ; 1 — electrode; 2, 3 — current-conducting and forming sections of the mould; 4 — bottom plate; D_e — electrode diameter; D_m — mould inner diameter; $h_{s,p}$ — depth of slag pool; $U_{p,s}$ — power source voltage

At such interpreting of the inner electrical connections of the elements of surfacing working zone, the mould will be a three-terminal device. If a surfacing diagram with one power source is used, than the mould due to electrical connection of any two (of three) elements (poles) is transformed into a two-terminal device, to terminals of which the source is connected.

Conductivity of conventional «inner» channel of the working zone characterizes a physicochemical state of «channel medium». The «channel medium» is a conventional presentation of the medium, through which current passes between the corresponding inputs/outputs, i.e. current-supplying elements of the mould working zone. Current can pass through the electrode or billet, through slag, through cooled walls of the mould, deposited metal and bottom plate. Conductivity of each of mentioned components of the medium depends on temperature of corresponding parts of the electrode, zones of slag pool and many others. Operator when setting the initial parameters of surfacing such as grades of used consumables, electrode diameter, rate of its immersion into a slag pool and voltage of power source can form the channel medium and, thus, vary nature of its conductivity. At that, change of voltage, applied to the channel, does not change its conductivity in allowably long time duration till the voltage change would not lead to variation of properties of media itself. In turn, introduction into the slag pool of electrode or billet having high conductivity and temperature different from the slag temperature will result in rapid change of pool properties and, thus, change of conductivity of the channels. Thus, in some way it can be assumed that conductivity of the inner channels of the surfacing working zone are the complex parameters characterizing surfacing process in CSM.

Position of the electrode in the slag pool effects the channels' conductivity and, if the temperature of slag is kept constant, relationship of channel conductivities can be indirectly used for estimation of location of end of the consumable electrode in the weld pool. At that, conductivities of the channels can be automatically controlled and regulated for automation purposes. Regulation of electrode feed rate on relationship of channels' conductivity will provide a set location of end of the consumable electrode in the slag pool.

One more of the complex parameters is consumed power. A temperature mode of surfacing process is determined by consumption of power of electric energy applied to the corresponding channel, i.e. for our example $P_{e-m} = I_m U_{e-m}$ and $P_{e-b} = I_b U_{e-b}$. Regulation of the consumed power allows controlling the temperature mode and efficiency of surfacing process. Auto-

matic control of the consumed power of applied electric energy is possible and variation of the consumed power in both channels to the set value is achieved by change of source voltage. Maintenance of the set relationship of conductivities in both channels and set power of electric energy applied to corresponding channel provides the possibility of quality characteristics of the deposited layer and fusion zone.

Let's consider a diagram for connection of the elements of surfacing working zone presented in Figure 1, *b*. If it is assumed that as a result of multiple experiments it was possible to determined the values optimum for technological purposes of conductivity and consumed power of electrode–mould channel, for example $G_{e-m}^{opt} = I_m^{opt} / U_{e-m}^{opt}$ and $P_{e-m}^{opt} = I_m^{opt} U_{e-m}^{opt}$, than after small transformations it is obtained $U_{e-m}^{opt} = \sqrt{P_{e-m}^{opt} / G_{e-m}^{opt}}$. So, operator or automatic system should have the possibility in process of surfacing to maintain U_{e-m}^{opt} value (at that, it is assumed that the electrode feed rate is kept constant at its optimum value). It follows from here that for the purpose of automatic regulation of surfacing process the power source voltage should be smoothly changed in the required limits. Besides, it is necessary to provide control and regulation of electrode displacement at stationary mould or, vice versa, mould at stable electrode, with sufficient accuracy and in the necessary range to maintain U_{e-m}^{opt} in accordance with the technological requirements.

It is supposed that for the specific set initial conditions of surfacing there is a single optimum solution on variation in time of electrode displacement rate as well as corresponding solution on change in time of source voltage (in set time interval). As a result of realizing such a solution it is possible to reach predicted quality of surfacing with the set values of deposition rate and energy efficiency. Search of indicated «optimum» solution should be preformed by a control system using automatic collection of data on each surfacing.

It is possible to formalize types of channels in the working zone following the ideas on the mould working zone. There are three types of diagrams of surfacing working zone channels in CSM (Figure 3), marked as «E», «K» and «P». They differ by location of common terminals of the working zone (common terminal corresponds to input/output, on which sum current I_{sum} is passing). In this interpretation the channel of surfacing working zone in CSM is a pass between the elements of this zone connected by resistor. Resistor conductivity is a channel conductivity.

Due to the fact that there are three current-supplying elements in the working zone, then number of variants of power source connection also makes three

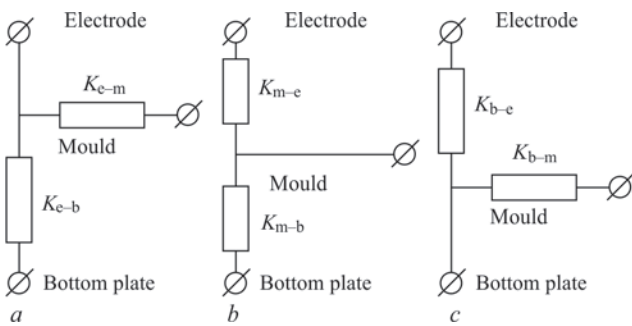


Figure 3. Types of diagrams of surfacing working zone channels: *a* — «E»; *b* — «K»; *c* — «P» (K_{e-m} — «electrode–mould» channel; K_{e-b} — «electrode–bottom plate»; K_{m-e} — «mould–electrode»; K_{m-b} — «mould–bottom plate»; K_{b-e} — «bottom plate–electrode»; K_{b-m} — «bottom plate–mould»)

since the source is connected to a pair of zone elements. There are only two variants for connection of remaining third terminal, namely to one or to another source terminal. Figure 4, as an example, shows the diagrams for connection of elements of working zone to alternating current power source. The diagrams for connection to direct current source are similar.

Thus, three variants of diagrams for connection of source to mould are proposed. The most perspective for increase of surfacing efficiency is «E» type diagram and, in less degree, «K», since the experience shows that the best melting of the electrode takes place at sufficiently high currents, passing through the electrode and mould, thus providing high process efficiency. In contrast to a diagram of type «P», which is characterized by high current passing through the bottom plate, small rate of electrode melting, but good and uniform penetration of the base metal.

Therefore, when choosing a diagram for connection of source to current-supplying elements of the working zone, it is necessary, first of all, orient on selection of type of channel diagram, i.e. on that which terminals shall be short-circuited. Geometry of the working zone of mould in many aspects determines this choice.

The following functions are taken as one being automated for the first stage of system development:

- function of selection and maintain of electric mode for formation of fusion of dissimilar metals

with set relative nonuniformity of penetration and minimum average penetration depth;

- function of selection and maintain of electric mode for providing stable conditions of deposited metal solidification.

Selection of that or another electric mode is carried out by operator from the list provided by the system. The system is designed in such a way that a story of surfacing was collected and stored in computer memory. From the information in computer memory the operator can select necessary mode or develop new with further storage. After mode is selected and system launched «into operation», the system stabilizes the set parameters in a set range. The values of set parameters and range of stabilizing are not constant and being determined by selected mode.

Automation of mode of fusion formation between dissimilar metals with set relative nonuniformity of penetration and minimum average penetration depth requires stabilizing the set value of electrode deepening and set voltage of source in connection of source to CSM on diagram «P».

Automation of stable conditions for deposited metal solidification requires stabilizing the set value of conductivity of electrode-bottom plate channel and set voltage of source during connection of source to CSM on diagram «E».

Such an approach of electroslag surfacing was proposed in work [9] based on evaluation of longitudinal sections of bimetal billets.

Conceptually, the following functions and problems shall be fulfilled in development of a system for automatic control of ESS in CSM:

- control and indication of current values of rate of consumable electrode displacement, voltage of power source, surfacing currents passing through the electrode, mould and bottom plate;
- providing the devices setting the values of mode parameters, indication of set typical surfacing mode;
- control and indication of values of calculated parameters (value of electrode deepening, deposition rate, time of process etc.);

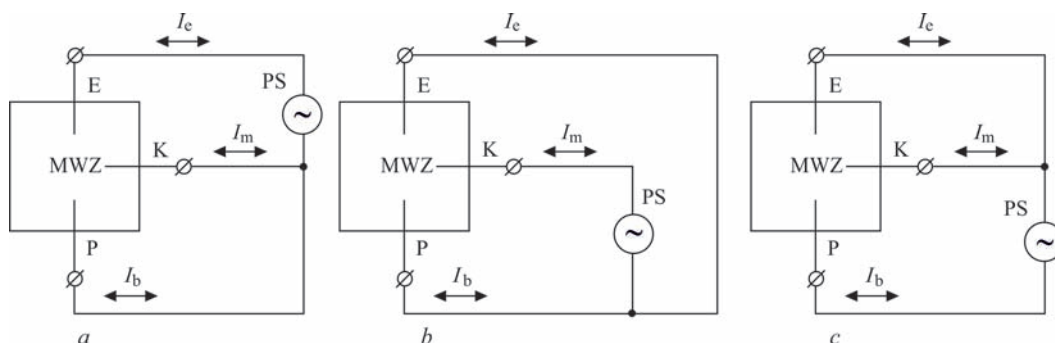


Figure 4. Types of diagrams for connection of elements of surfacing working zone to alternating current power source: *a* — «E»; *b* — «K»; *c* — «P»

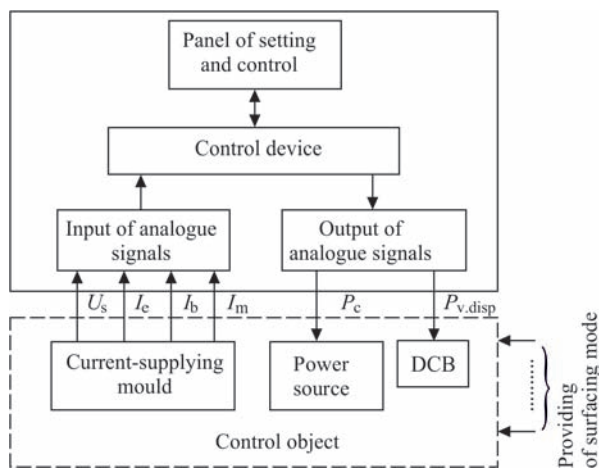


Figure 5. Structural scheme of automation of base metal penetration in ESS in CSM

- mathematical modelling and experimental researches of dependencies of depth and uniformity of penetration on value of electrode deepening and power consume by current-supplying mould;
- automatic control of electrode displacement;
- automatic control of voltage, current and power consumed by surfacing.

Structural scheme of automation of base metal penetration during ESS in CSM is presented in Figure 5. The system consists of a block of «Input of analogue signals» designed for entry into the system of signals of surfacing voltage U_s and currents I_e , I_b , I_m , i.e. electrode, bottom plate and mould, respectively, coming from probes located in the immediate vicinity to «Current-supplying mould». Block for «Output of analogue signals» is designed for output of the controlling signals P_c — controller of output voltage of «Power source» and $P_{v,disp}$ — controller of displacement rate of consumable electrode, which influences a drive control block («DCB») of electrode displacement mechanism. «Panel of setting and control» is designed for manual entry and indication of discrete, digital, text information and automatic input of indicated information in «Control device» as well as obtaining from it the signal for indication on «Panel of setting and control» itself. «Control device» obtains the analogue signals from «Control object» and discrete signals from «Panel of setting and control», performs mathematical processing of these signals and forms the discrete signals for transfer into «Panel of setting and control» for indication as well as the controlling analogue signals for «Control object». Besides, it records a history of surfacing for unstudied types and modes of surfacing for the purpose of further processing of recorded information files and modernizing system software, forms an array of approximating regression functions for types and modes of surfacing provided in the system as well as an array of surfacing history.

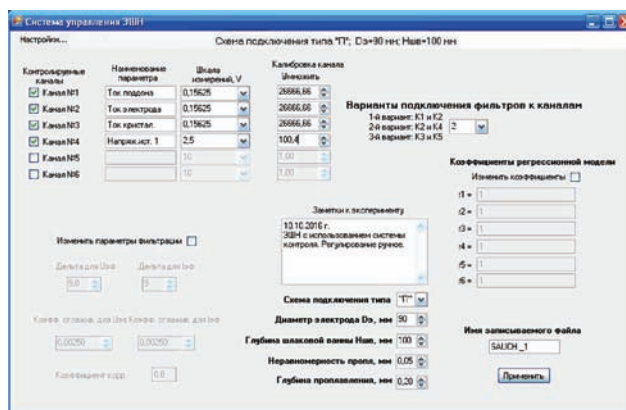


Figure 6. Appearance of computer screen at initial setting of ESS control system before surfacing

At this stage the «Control device» is realized based on notebook LENOVO model IdealPad Y560 with 64-bit operating system. Input of analogue information is carried out using external ADT E14-140-M L-CARD (bus USB2), which is in particular conformable for development of portable measuring system based on notebook. It has software controlled setting of the parameters for data collection, namely amount and sequence of input channels' inquiry, measurement range, frequency of analogue-digital transducer. An original non-standard device of own design is used as normalizing transducers of current and voltage signals.

«Manual» regulation was carried out using the indices calculated by the system. Manual mode was used to maintain a rate of electrode feed for the purpose of stabilizing the value of electrode deepening into the slag pool as well as value of power voltage.

Figure 6 presents a view of computer screen at initial setting of the ESS control system before surfacing. Parameters of entering and filtering the input signals, technological conditions of subsequent surfacing, type of diagram for connection of source to CSM etc. are set.

Figure 7 presents a view of computer screen during system operation in mode of control, regulation and registration of surfacing process. The values of source



Figure 7. Appearance of computer screen during system operation in control mode, regulation and registration of surfacing process

voltage, currents of bottom plate, mould and electrode are displayed on the screen in real time mode with frequency of presentation 1 Hz. A rate of surfacing and duration of surfacing are presented with 1 min period. Calculated current values of process parameters are displayed with 5 s period.

Conclusions

1. Developed were the main principles of design of the system for automatic regulation of base metal penetration in end face electroslag surfacing with large-section electrodes in current-supplying mould. A pilot version of computer system for automatic control of ESS in CSM was developed.

2. Based on the presentations of the mould working zone, technologist can choose among three proposed diagrams of current distribution in surfacing working zone, titled as «E», «K» and «P», which determine the process of electrode melting and value of base metal penetration.

3. Determined were the main controlled complex parameters in the system, i.e. electric conductivity of the channels and power consumed by them. Using them it is possible in indirect way to determine position of the end face of consumable electrode in the slag pool and regulate the process of electroslag surfacing varying the rates of electrode deepening and voltage of power source. It will result in providing the

minimum and uniform penetration of the base metal, stabilizing the surfacing process with the set values of productivity and energy efficiency.

1. Kuskov, Yu.M., Gordan, G.N., Ereemeeva, L.T. et al. (2015) Electroslag surfacing using discrete materials of different methods of manufacture. *The Paton Welding J.*, **5–6**, 121–123.
2. Moiseev, V.V., Zakamarkin, M.K., Loiferman, M.A., Chetvertnykh, V.V. (2001) One million of steel ESR was melted using computer. *Problemy Spets. Elektrometallurgii*, **3**, 15–18 [in Russian].
3. Troyansky, A.A., Ryabtsev, A.D., Samborsky, M.V., Mastepan, V.Yu. (2002) Application of information measurement system for study of ESR process. *Metall i Lityo Ukrainy*, **7–8**, 25–26 [in Russian].
4. Vladimirovsky, E.I., Ismajlov, B.I. (2011) *Synergetic methods of control of chaotic systems*. Baku, ELM [in Russian].
5. Dudko, D.A., Rublevsky, I.N. (1962) To problem of nature of barrier effect during electroslag process. *Avtomatich. Svarka*, **4**, 40–48 [in Russian].
6. Kuskov, Yu.M., Soloviov, V.G., Zhdanov, V.A. (2017) Electroslag surfacing of end faces with large-section electrode in current-supplying mould. *The Paton Welding J.*, **12**, 29–32.
7. Mironov, Yu.M. (2002) Influence of current nature on processes in electroslag installations. *Elektrometallurgiya*, **4**, 25–32 [in Russian].
8. Soloviov, V.G., Kuskov, Yu.M. (2018) Influence of technological and electrical parameters of ESS in current-supplying mould on electrode melting rate and base metal penetration. *The Paton Welding J.*, **6**, 20–27.
9. Kuskov, Yu.M., Soloviov, V.G., Osechkov, P.P., Osin, V.V. (2018) Electroslag surfacing with large-section electrode at direct current in current-supplying mould. *Ibid.*, **3**, 32–35.

Received 15.03.2018

MODELING OF PHASE-STRUCTURE STATE AND REGULATION OF PROPERTIES OF Fe–Cr–Mn ALLOYING SYSTEM METAL DEPOSITED ON LOW-CARBON STRUCTURAL STEEL

Ya.A. CHEYLYAKH and A.P. CHEYLYAKH

Pryazovskyi State Technical University

7 Universitetskaya Str., 87555, Mariupol, Donetsk region, Ukraine. E-mail: cheylyakh_o_p@pstu.edu

A physical-mathematical model was developed. It describes formation of a structure of deposited metal of Fe–Cr–Mn alloying system and binds its chemical composition, critical points of martensite transformation (M_s , M_f), phase-structure state and nature of their layer-by-layer variation on thickness of the deposited metal. The model allows designing and regulating chemical and phase compositions (austenite, austenite-martensite, martensite-austenite, martensite) of metal of Fe–Cr–Mn alloying system deposited on steel St3 that provides the possibility to regulate service properties of the deposited metal. Specific conditions of operation of the deposited parts require selection of phase composition of the deposited metal (content of quenching martensite and metastable austenite), level of γ -phase metastability providing optimum development of deformation $\gamma \rightarrow \alpha'$ -transformation and acquiring of the most significant effect of strengthening in process of testing and operation. 14 Ref., 1 Table, 4 Figures.

Keywords: *surfacing; flux-cored wire, metastable austenite, martensite, modeling, transformations, wear resistance*

Regulation of structure and service properties of deposited metal (DM) is one the main problems in production and restoration surfacing of virtually all critical parts in different branches of industry [1–3]. This problem is in particular relevant in surfacing of high-manganese and high-chromium-manganese steels taking into account that these steels have metastable austenite structure, which can be strengthened in process of operation under dynamic mechanical loads [4–8]. Considering the fact that significant penetration of base metal and previous deposited layers can be observed in arc surfacing, chemical and phase composition as well as structure of the deposited metal will be changed in specific way from layer to layer.

The aim of present work is development of a scientific-based model of formation and regulation of phase-structure state and service properties of deposited metal of Fe–Cr–Mn alloying system depending on its composition and composition of base metal as well as parameters of technology of electric arc flux-cored wire surfacing.

A physical-mathematic model (No.1) of layer-by-layer-steplike distribution of alloying elements on the DM layers depending on a level of base metal penetration [9] was proposed. The model with some assumption supposes that content of alloying elements in the DM layers changes gradually. In multilayer surfacing composition of each layer is determined by di-

lution of previous and portion of its participation in formation of each next layer ($N_1, N_2, N_3 \dots N_i$). It is determined that any combinations of different or same portions of participation of base metal in the deposited one by layers, equal in the sum ($N_1 + N_2 + N_3 \dots N_i$), provide similar composition of the resulting (upper) deposited layer. Based on experimental investigations and analysis of formation of composition in each of the deposited layers there was obtained an equation for calculation of content of each of elements in i -th deposited layer at various levels of penetration:

$$C_e^{DMi} = C_e^0 N_1 N_2 N_3 \dots N_i + C_e^s (1 - N_1 N_2 N_3 \dots N_i), \quad (1)$$

where C_e^b is the content of element in base metal; C_e^s is the set content of element.

At similar portion of the base metal and previous layers in the deposited metal, dependence (1) has the next view:

$$C_e^{DMi} = C_e^0 N^i + C_e^s (1 - N^i). \quad (2)$$

Taking into account possible oxidation (burn-out loss) of alloying elements (in open arc surfacing) or addition of alloying elements from the flux into the melt, expressions (1) and (2) shall be completed with a summand $\pm \Delta C_e^f$, characterizing contribution of flux content into the DM composition, similar to data of work [10]:

$$C_e^{DMi} = C_e^0 N_1 N_2 N_3 \dots N_i + C_e^s (1 - N_1 N_2 N_3 \dots N_i) \pm \Delta C_e^f, \quad (3)$$

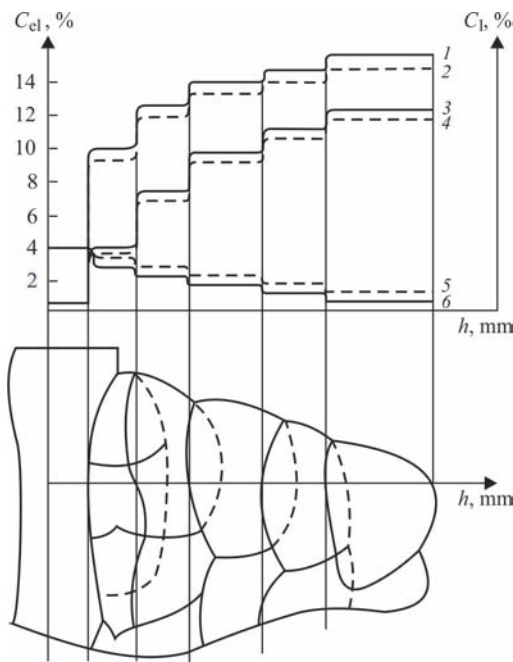


Figure 1. Model of distribution of alloying elements content on DM layers: 1, 2 — chromium; 3, 4 — manganese; 5, 6 — carbon (solid lines — $N = 0.3$; dashed — $N = 0.5$)

$$C_e^{DMi} = C_e^0 N^i + C_e^s (1 - N^i) \pm \Delta C_e^f \quad (4)$$

Obtained equations (1)–(4) prove the known conclusion that the less the penetration level and, respectively, portion of participation of base metal into deposited one N is, the quicker and at less amount of layers the set composition of the DM is reached [1].

At different portion of participation of the base metal in each of the deposited layers of multi-layer surfacing the result of calculation of element content is determined taking into account their product ($N_1 N_2 N_3 \dots N_i$). Based on set forth, a physical-mathematical model of layer-by-layer formation of chemical and phase composition (No.1), graphical interpretation of which is given in Figure 1, was proposed. After first layer surfacing on unalloyed steel-base (St3) the content of alloying elements in the first DM

layer is sufficiently rapidly increased at transfer of a fusion zone and on thickness of this layer the average concentration remains approximately the same, that corresponds to a horizontal section of a concentration distribution curve. At that, the set content of alloying elements in the first layer is not usually achieved. After surfacing of the second layer the concentration of alloying elements on fusion zone of the first and second layers due to penetration of the first layer with specific N_2 again rises, and, approximately, stays the same on thickness of this (second) layer (Figure 1, curves 1, 2). Composition of the third and next layers is formed in the same way.

According to calculations, content of carbon also gradually varies by layers to the side of increase, or, vice versa, reduction (as it is shown in Figure 1, curves 5, 6) depending on its content in metal-base in relation to content in flux-cored wire. In layers 4–6 the concentration of the elements will correspond to set content of the flux-cored wire.

The quicker the rate of surfacing and the less current in studied limits ($v_{surf} = 18\text{--}38$ m/h, $I = 320\text{--}500$ A) are, the less the portion of participation of metal from each previous layer in formation of the next one is, the narrower the zone of interlayer fusion is and the larger the difference in the concentrations of elements between the horizontal lines on concentration curves of a layer-by-layer analysis is.

The layer-by-layer calculation of metal deposited with flux-cored wire PP-Np-12Kh13G-12STAF, using proposed model is given in the Table. As can be seen from the given data, multilayer surfacing provides DM with the structure of metastable austenite.

Relationship of the alloying elements (first of all chromium and manganese) as well as carbon, having significant effect (decrease) on points of M_s and M_f was selected in such a way that in the upper layer of DM it was austenite metastable structure, corresponding to 12Kh13G12STAF composition.

At small portion of the base metal and next layer in the deposited metal ($N_1, N_2, N_3 \leq 0.3$) the set composition of metal, deposited with wire PP-Np-12Kh13G-12STAF is already reached in the third layer, which corresponds to steel 12Kh13G12STAF with metastable austenite. At average values of $N_1, N_2, N_3 \approx 0.5$ the set composition of DM can be obtained only in the fourth or even fifth layer. In the third layer it will correspond to grade 14Kh12G11STAF of austenite class with under-alloying on chromium (by $\sim 1.5\%$), manganese (by $\sim 1.5\%$) and overrating by 0.02% content of carbon (Table).

At large portion of the base metal and next layers ($N_1, N_2, N_3 \approx 0.7$) the content of the third deposited layer will correspond to steel 15Kh9G8STAF (Ta-

Calculation composition of DM depending on portion of base metal in deposited (N) in three-layer surfacing using flux-cored wire PP-Np-12Kh13G12STAF

Layer number	N for each layer of DM			Calculation composition of DM (type of deposited metal)	Phase composition of DM
	1	2	3		
1	0.3	–	–	14Kh9G8STAF	M + A
2	0.3	0.3	–	12Kh11G9STAF	A + M
3	0.3	0.3	0.3	12Kh13G12STAF	A
1	0.5	–	–	17Kh7G6STAF	M + A
3	0.5	0.5	0.5	14Kh12G11STAF	A
1	0.7	–	–	19Kh5G4STAF	M
3	0.7	0.7	0.7	15Kh9G8STAF	A + M

Note. M — quenching martensite; A — austenite.

ble) with lack of alloying from the set composition on chromium and manganese by $\sim 4\%$, on silicon by $\sim 0.6\%$, excess of carbon content by $\sim 0.03\%$, content of vanadium and titanium can be at lower limits. This deposited metal refers to martensite-austenite class. In surfacing with penetration level $N \approx 0.7$ (modes, which provide such a penetration, are not recommended to be used in surfacing), acquiring the set composition will only be possible in layers 6–7. Reliability of the results of DM calculation on the developed model is proved by the experimental results of works [9, 10] and others.

Composition of each layer effects martensite points M_s , M_f and M_d^* and determines phase composition of the layers of deposited metal [11, 12]: austenite (A); austenite-martensite (A + M) ($< 50\%$ of quenching martensite and $> 50\%$ of austenite); martensite-austenite (M + A) ($> 50\%$ of quenching martensite, the rest is A_{res}); martensite (M) with 5–15% of A_{res} . In all cases structure of the deposited metal includes small amount of carbides (carbonitrides).

Nature of distribution of chemical elements according to the proposed model is proved by the experimental results of spectral (quantometric) analysis on quantometer «SpectromaxX» (after step-by-step grinding away of a layer by 0.3–0.5 mm as well as micro-X-ray-spectrum analysis using autoemission electron microscope «Ultra-55» (with a step of 0.1–0.2 mm order) (Figure 2). A structure-phase state on the layers of Fe–Cr–Mn DM was determined by the methods of quantitative metallography and X-ray structural analysis on diffractometer DRON-3 in iron K_α -radiation.

A structural class of DM (layer-by-layer) was determined on quantitative relationship of quenching martensite and metastable austenite. An upper layer in three-layer surfacing using PP-Np-12Kh13G12S-TAF wire at $N_i = 0.31$ – 0.40 corresponds to grade DM 20Kh12G9STAF and (A + M) class. Within the limits of each layer there are variations of content of the elements in small limits, typical for arc surfacing with flux-cored wire. At $N_i = 0.70$ – 0.76 , the DM of 20Kh10G8STAF grade and (M + A) class with qualitatively similar nature of alloying elements distribution is formed in the third layer.

Due to the importance of taking into account the effect of composition of each layer on phase content of the DM, the physical-mathematical model was developed, which considers effect of the main elements (Cr, Mn, Si, C) on point M_s in Fe–Cr–Mn steels. Application of this model allowed obtaining different DM compositions (12–20)Kh(8–13)G(6–12)STAF

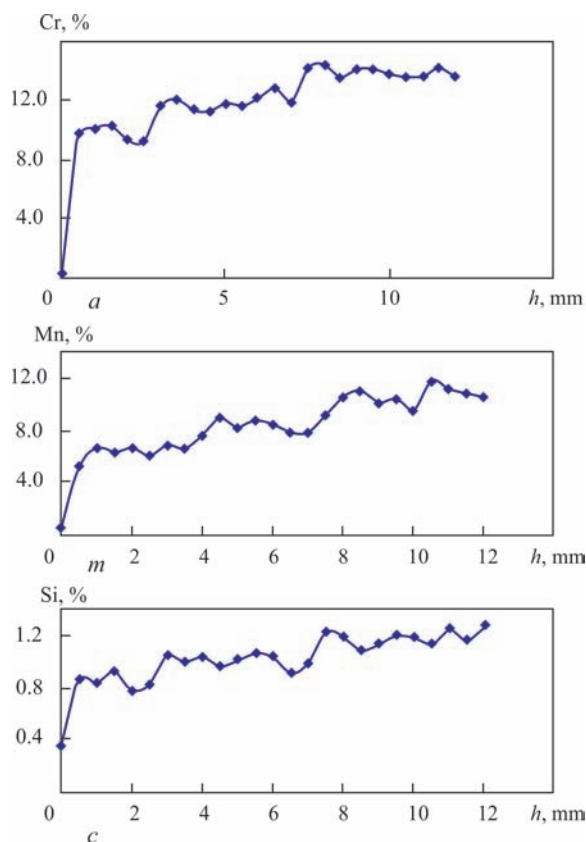


Figure 2. Distribution of alloying elements on thickness h of three-layer DM of 20Kh12G9STAF steel type: a — chromium; b — manganese; c — silicon

with variation of content of elements within (wt.%): 0.12–0.2 C, 8–13 Cr, 6–12 Mn.

Using regression analysis of the experimental data on high-strength steels of close alloying of Fe–0.3% C–(2–8)% Cr–6% Mn–2% Si and Fe–0.1% C–14% Cr–(0–8)% Mn compositions, the next polynomial dependencies of $p. M_s$ on content of chromium and manganese were obtained:

$$M_s(\text{Cr}) = -a\text{Cr}^3 + b\text{Cr}^2 - c\text{Cr} + d + \Delta M_s; \quad (4)$$

$$M_s(\text{Mn}) = -a(\text{Mn})^2 - b(\text{Mn}) + c + \Delta M_s, \quad (5)$$

where Cr and Mn is the content of elements in the DM, wt.%; a, b, c, d are the constant coefficients reflecting the level of element effect; ΔM_s is the average value of displacement of $p. M_s$ from the experimental dependencies under effect of carbon and alloying elements (on generalizing the reference data provided in work [12]):

$$\Delta M_s = -500\Delta C - 38\Delta \text{Mn} - 8\Delta \text{Cr} - 40\Delta \text{Si}, \quad (6)$$

where $\Delta C, \Delta \text{Mn}, \Delta \text{Si}, \Delta \text{Cr}$ are the difference between the content of the alloying element in the experimental and model DM, %.

The correlation coefficients made: for equation (4) — $R^2 = 0.9999$; (5) — $R^2 = 0.9975$.

* M_d is the lowest temperature, at which not less than 50% of deformation martensite due to DMTW is formed.

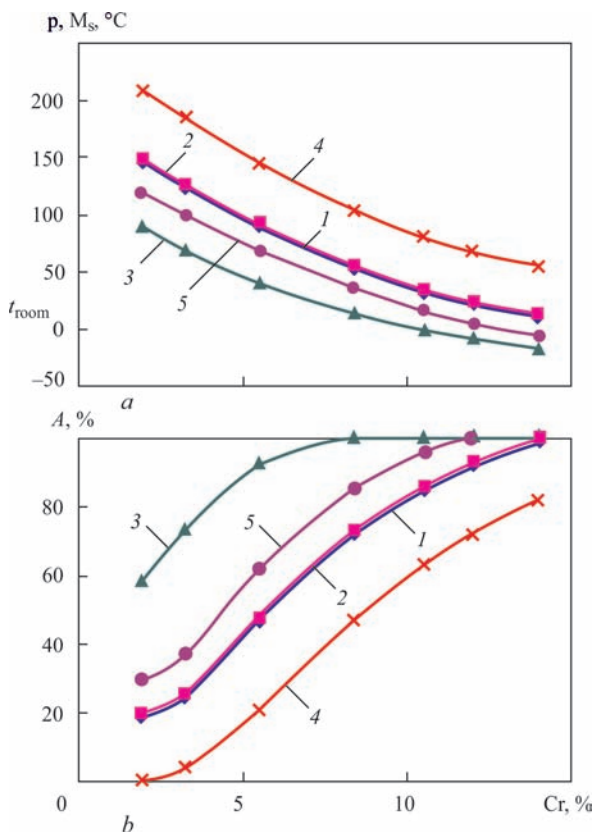


Figure 3. Experimental and calculated dependencies of chromium effect on position of $p. M_s$ (a) and amount of austenite (b) in Fe–Cr–Mn steels with different variation of alloying elements: 1 — experimental steels 30Kh(2–8)G6S2F (with extrapolation of curves to 14.0 % of Cr); model; 2 — 20Kh(2–14)G8SF; 3 — 20Kh(2–14)G10SF; 4 — 10Kh(2–14)G8SF; 5 — 10Kh(2–14)G10SF

A series of curves were plotted in a calculation way with the help of equations (4)–(6) using the model, namely dependencies of $p. M_s$ from content of chromium and manganese at the discrete values of content of the rest elements (Mn, Cr, Si, C, respectively), some of which are given in Figure 3. For any ratio of the main alloying elements (Cr, Mn) the temperatures of $p. M_s$ were calculated using the model and in cooling to room temperature there were determined an amount of forming phases — martensite and austenite in Fe–Cr–Mn structure of the DM. Thus, for the DM, containing approximately Cr 10 %, Mn 8 %, C 0.2 % (at similar content of silicon and vanadium), $p. M_s = 40$ °C (Figure 3, a, curve 2). At room temperature its phase composition is ~ 82 % of austenite and ~ 18 % of quenching martensite (Figure 3, b, curve 2). And for steel with the same content of chromium (~ 10 %), but higher content of manganese, for example, 10 %, its structure will be austenitic. The calculated ratios of phase composition (content of martensite and austenite) are proved by the experimental data of magnetometric and X-ray structural methods, given in works [10, 12].

The developed model allows also using the set phase composition determining the necessary com-

position of alloying elements in the DM and corresponding to it position of $p. M_s$. Based on this content using the known methods [13] it is possible to calculate composition of the charge of flux-cored wire, which will provide formation of set chemical and phase-structure composition of the DM.

The obtained calculation ratios of amount of quenching martensite and metastable austenite for Fe–Cr–Mn of DM adequately correspond to the experimental results determined by magnetometric and X-ray structural methods [11, 12].

Generalization of two models considered above allows explaining the differences of layer-by-layer formation of DM phase content on concentration of the chemical elements according to the next cause-and-effect relationship. Chemical composition of each deposited layer depends on composition of material being deposited, level of penetration (portion) of base metal and further deposited layers (Figure 4, a). Content of elements in the layers determines the temperatures of $p. M_s$ and M_f (Figure 4, b) effecting the amount of martensite and metastable austenite in the limits from 0 % to 100 % of each phase (Figure 4, c) forming during Fe–Cr–Mn DM cooling. This relationship determines formation of wear resistance of the examined DM (Figure 5). In the first approximation, the more formation of quenching martensite is, the higher the hardness and wear resistance are, and the more remaining austenite is, the lower these properties are, but higher ductility and impact toughness are. However, these characteristics and wear resistance of DM depend not only on ratio of amount of quenching martensite and austenite. Particularly important is that austenite in the structure of the examined Fe–Cr–Mn DM is a metastable phase subjected to deformation martensite $\gamma \rightarrow \alpha'$ -transformation in the process of testing (wear-out) (DMTW) provoking deformation hardening and, simultaneously, stress relaxation. A level of metastability, determining DMTW kinetics and amount of forming deformation martensite, depends on different factors, namely ratio between content of quenching martensite and metastable austenite, content and level of its strengthening, heat treatment, conditions of tests and operation [8, 11]. All these in total determine formation of mechanical and service properties of the DM of Fe–Cr–Mn alloying system.

Figure 4, b schematically shows a graphical dependence of $p. M_s$ position on content of one of the alloying elements in Fe–Cr–Mn DM (for example, chromium, manganese or carbon). Dependence of amount of quenching martensite M and austenite A on position of $p. M_s$ are given in Figure 4, c. The latter shows various quantitative ratio between quenching martensite for different content of the alloying

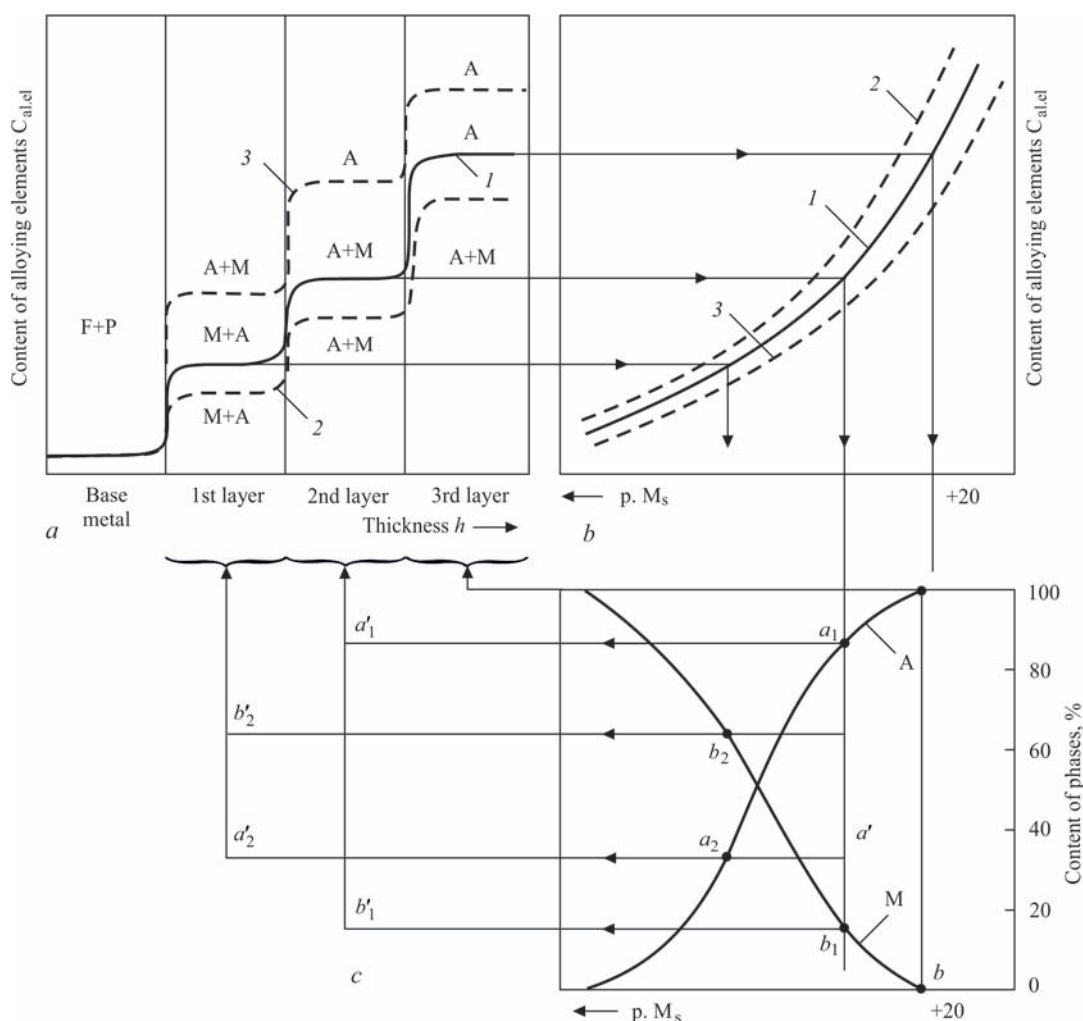


Figure 4. Principal diagram of calculation on proposed generalized model of layer-by-layer-steplike chemical and structural composition of deposited Fr–Cr–Mn metal: *a* — 1–3 — curves of distribution of phase content on layers of DM; *b* — 1–3 — corresponding to them curves of $p. M_s$ dependencies on content of main alloying elements (Cr, Mn, Si) (see Figure 3 and data of work [12]; *c* — dependence of amount of austenite (*a*) and quenching martensite (*M*) on position $p. M_s$ (more details in work [12]; A — austenite, M — quenching martensite, F + P — ferrite-pearlite structure of base metal (St3))

elements and, respectively, different temperature of $p. M_s$ (for example a_1, b_1, a_2, b_2 in Figure 4, *c*).

Obtained experimentally graphical dependencies between $p. M_s$ and amount of quenching martensite *M*, austenite *A* for system of steel alloying with 30Kh(2–14)G6S2F and 10Kh14G(0–12) content [11] are approximated by a polynomial function of the 3rd level:

$$\begin{aligned} M(\%) &= -6 \cdot 10^{-5} (M_s)^3 + 0.147 (M_s)^2 - 0.2236 (M_s) + 0.8859; \\ A(\%) &= 100 - M(\%). \end{aligned} \quad (7)$$

At that a coefficient of correlation made $R^2 = 1.0$.

A projection of points of curve $p. M_s - f(\% \text{ Cr, Mn, Si})$ of the model (No.2) (Figure 4, *b*) on steplike curves of the model (No.1) (Figure 4, *a*) explains the nature of alternation of the phase-structure compositions: base metal $\rightarrow (M + A) \rightarrow (A + M) \rightarrow A$ on its thickness (from fusion zone with base metal to surface layer), that is determined by $p. M_s$ temperature, depending on content of alloying elements in the DM layers (Figure 4, *a*).

The generalized model allows predicting and designing the phase composition of the DM by layers taking into account technological parameters of surfacing mentioned above. Rising content of such elements as Cr, Mn, Si, C (separately or in a complex) provokes reduction of $p. M_s$ (Figure 4, *b*) and variation of phase composition to the side of increase of austenite content, and decrease of content of quenching martensite, respectively (Figure 4, *c*). Following from the set chemical composition of DM, a series of curves $p. M_s - f(\% \text{ Cr, Mn, Si})$ were plotted using model No.2 [12] (Figure 4, *b*, curves 1–3).

When generalizing models Nos 1 and 2 it is possible quantitatively calculate obtained phase composition (% A; % M) in each deposited layer by Figure 4, *c*, getting steplike curves 1, 2, 3 on Figure 4, *a*. For this there is a use of obtained calculation dependencies (7) and dependences of content of phases on $p. M_s$ (Figure 4, *c*) through the effect on it of alloying elements and carbon in each deposited layer, projecting

received points on curves 1, 2, 3 (Figure 4, *b*) through Figure 4, *c* on Figure 4, *a*. Projecting determined in such a way phase composition (wt.%) from curves on Figure 4, *a* to the curve (Figure 4, *b*), and from it down to Figure 4, *c* it is possible to get a qualitative and quantitative presentation on phase composition of each of the deposited layers (Figure 4, *a*).

As an example it is possible to consider the DM corresponding to curve 1 of distribution of alloying elements by layers (Figure 4, *a*). The first (lower) layer is characterized with a horizontal shelf of step, which shall be projected on curve 1 (Figure 4, *b*), corresponding to present deposited metal and conditions of surfacing, and characterizing dependence $p. M_s$ and content of elements in this layer. The projections of obtained point on a phase composition diagram (ratios of phases of quenching martensite — M and austenite — A) show the content of quenching martensite ($p. b_2 \approx 65\%$) and austenite ($a_2 \approx 35\%$). Points b'_2 and a'_2 are characterized with martensite-austenite (M + A) phase composition of the first layer (shown by arrow to brace on Figure 4, *a*). The second layer is characterized by corresponding step (Figure 4, *a*), projection of which on Figure 4, *b* for considered above curve 1, and down from it to Figure 4, *c* show the obtained phase composition, which is characterized by points $a_1 \approx 89\%$ of austenite and $b_1 \approx 11\%$ of quenching martensite. The projections of these points a'_1 and b'_1 (arrow up to brace) show austenite-martensite (A + M) phase composition of the second layer on Figure 4, *a*. The upper third layer of DM is characterized with the upper step on a model diagram (Figure 4, *a*). Its projection on curve 1 Figure 4, *b*, and then down to curve 4, *c*, shows purely austenite phase composition (100% A).

In a similar way it is possible to consider formation of composition, and from it through effect on

$p. M_s$ (Figure 4, *b*) i.e. formation of phase composition (A and M) on Figure 4, *c* for other conditions of surfacing characterized by lower content of alloying elements and carbon (curve 2 on Figure 4, *a*) or, vice versa, large one (curve 3 in Figure 4, *a*). This depends on somewhat different composition of the deposited metal of the same Fe–Cr–Mn alloying system, or at its similar composition on other indices of penetration (portion) of base metal and next layers.

Obtained calculation results on content of martensite and metastable austenite on DM layers, the same as layer-by-layer-steplike nature of change of chemical phase-structure compositions on the DM layers, are proved by quantitative analysis, electron microscopy, metallographic and X-ray structural examinations.

In total, obtained in surfacing microstructure and level of γ -phase metastability determine the nature and $\gamma \rightarrow \alpha'$ kinetics of DMTW and allow regulating formation of physical-mechanical and service properties. Selecting indicated parameters, it is possible to get combinations of different phase-structure zones (A, A + M, M + A, M) of Fe–Cr–Mn deposited metal of different thickness.

Hardness and wear resistance of the DM is varied corresponding to layer-by-layer nature of change of the phase-structure state and level of deformation of austenite metastability. Schematically it is shown in Figure 5 based on generalizing the results of our previous researches [10, 11, 14], where similar curves for the DM of various chemical and phase compositions are given. The highest hardness of Fe–Cr–Mn DM corresponds to (M + A) structure (first or second layer), then it drops due to increase of content of more plastic austenite in (A + M) structure and decreases to larger level for austenite structure (the second or third layer, respectively). Following the experimental data, the highest wear resistance of the DM of Fe–Cr–Mn alloying system is provided by austenite-martensite structure with active $\gamma\text{-}\alpha'$ kinetics of DMTW [10, 11].

The reason of significant increase of wear resistance of metastable Fe–Cr–Mn DM with (A + M) structure is obtaining in surfacing of some amount of quenching martensite (20–30%) and formation of significant amount of deformation martensite in thin surface layer (30–55%) as a result of $\gamma\text{-}\alpha'$ development of DMTW as well as cold working of martensite-austenite structure under effect of wear-out medium.

The deformation martensite differs by increased dispersion, higher level of microdistortions and increased dislocation density, and process of its formation is accompanied by relaxation processes [8] that promotes rise of DM ductility, wear resistance and life duration. It is also probable development of dynamic deformation ageing characterized with precipitation of high-disperse par-

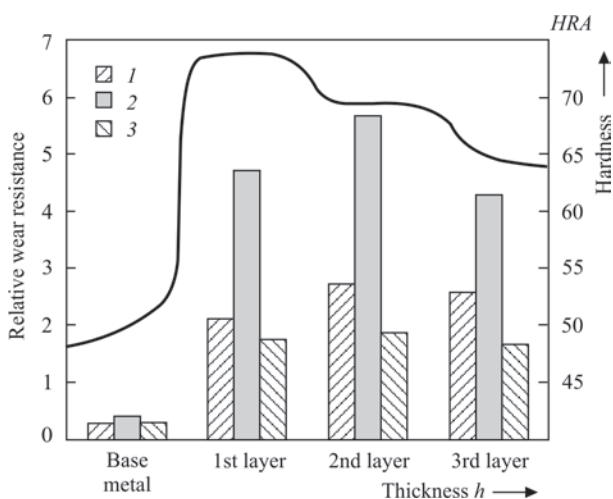


Figure 5. Dependence of hardness (curve) and relative wear resistance under different conditions of wear out of metastable Fe–Cr–Mn DM: 1 — metal on metal; 2 — impact-abrasive; 3 — abrasive

ticles of carbides and carbonitrides from martensite and austenite in course of wear out in the surface layer that is also an important factor of wear resistance increase. Certainly, for specific conditions of operation of the deposited parts it is necessary to select phase composition (content of quenching martensite and metastable austenite), level of metastability of γ -phase providing optimum γ - α' development of DMTW and acquiring the highest strengthening effect in the process of tests and operation.

In whole, the optimum parameters of chemical and phase composition, microstructure and γ - α' kinetics of DMTW for each type of wear out provide improved characteristics of properties and wear resistance of the examined metastable DM, which significantly exceed properties of deformation-stable materials of close alloying.

1. Frumin, I.I. (1961) *Automatic electric arc surfacing*. Kharkov, Metallurgizdat [in Russian].
2. Livchits, L.S., Grinberg, N.A., Kurkumelli, E.G. (1969) *Principles of alloying of deposited metal*. Moscow, Mashinostroenie [in Russian].
3. Ryabtsev, I.A., Senchenkov, I.K. (2013) *Theory and practice of surfacing works*. Kiev, Ekotekhnologiya [in Russian].
4. Razikov, M.I., Kulishenko, B.A. (1967) On selection of surfacing material resistant to cavitation loading. *Svarochn. Proizvodstvo*, **7**, 10–12 [in Russian].
5. Kalensky, V.K., Chernyak, Ya.P., Ryabtsev, I.A. (2003) *Powder electrode wire for welding and surfacing of steel products*. Pat. 39646, Ukraine [in Russian].
6. Ryabtsev, I.A., Kuskov, Yu.M., Chernyak, Ya.P. et al. (2004) Restoration of rings of rotary support of crane MKT-250. *Svarshchik*, **4**, 35–38 [in Russian].
7. Malinov, L.S., Malinov, V.L. (2009) *Resource-saving sparcely-alloyed alloys and strengthening technologies providing effect of self-quenching*. Mariupol, Renata [in Russian].
8. Ryabtsev, I.A., Kondratiev, I.A., Chernyak, Ya.P. et al. (2010) Structure and properties of high-manganese deposited metal. *The Paton Welding J.*, **4**, 7–9.
9. Cheylyakh, Ya.O. (2013) *Development of surfacing material and technology of surface strengthening with formation of wear-resistant metastable alloy*: Syn. of Thesis for Cand. of Techn. Sci. Degree. Kramatorsk [in Ukrainian].
10. Cheylyakh, Ya.A., Chigarev, V.V. (2011) Structure and properties of deposited wear-resistant Fe–Cr–Mn steel with a controllable content of metastable austenite. *The Paton Welding*, **8**, 17–21.
11. Cheylyakh, A.P. (2009) *Sparcely-alloyed metastable alloys and strengthening technologies*. Mariupol, PGTU [in Russian].
12. Cheylyakh, Ya.A., Krivenko, O.V., Shejchenko, G.V. (2013) Modeling of effect of alloying elements on p_s and phase composition of deposited Fe–Cr–Mn metastable steels. *Visnyk Pryazov. DTU. Ser.: Tekhnichni Nauky*. Mariupol, **27**, 82–89 [in Russian].
13. Pokhodnya, I.K., Suptel, A.M., Shlepakov, V.N. (1972) *Flux-cored wire welding*. Kiev, Naukova Dumka [in Russian].
14. Cheylyakh, Ya.A., Chigarev, V.V. (2011) Principles of change of composition and structure of deposited Fe–Cr–Mn metastable steels. In: *Proc. of Int. Conf. on Strategy of Quality in Industry and Education (3–10 June 2011, Varna, Bulgaria)*, **2**, 310–312.

Received 11.02.2018

PATON PUBLISHING HOUSE

www.patonpublishinghouse.com

SUBSCRIPTION

The Paton
WELDING JOURNAL

АВТОМАТИЧЕСКАЯ
СВАРКА

«The Paton Welding Journal» is Published Monthly Since 2000 in English, ISSN 0957-798X, DOI: <http://dx.doi.org/10.15407/tpwj>.

«Avtomaticheskaya Svarka» Journal (Automatic Welding) is Published Monthly Since 1948 in Russian, ISSN 005-111X, DOI: <http://dx.doi.org/10.15407/as>.

«The Paton Welding Journal» is Cover-to-Cover Translation of «Avtomaticheskaya Svarka» Journal into English.

If You are interested in making subscription directly via Editorial Board, fill, please, the coupon and send application by Fax or E-mail.

The cost of annual subscription via Editorial Board is \$384 for «The Paton Welding Journal» and \$180 for «Avtomaticheskaya Svarka» Journal.

«The Paton Welding Journal» can be also subscribed worldwide from catalogues subscription agency EBSO.

SUBSCRIPTION COUPON

Address for journal delivery _____

Term of subscription since _____

20

till _____

20

Name, initials _____

Affiliation _____

Position _____

Tel., Fax, E-mail _____

We offer the subscription all issues of the Journals in pdf format, starting from 2009.

The archives for 2009–2016 are free of charge on www.patonpublishinghouse.com site.



ADVERTISEMENT

in «Avtomaticheskaya Svarka» and «The Paton Welding Journal»

External cover, fully-colored:

First page of cover
(190×190 mm) — \$700

Second page of cover
(200×290 mm) — \$550

Third page of cover
(200×290 mm) — \$500

Fourth page of cover
(200×290 mm) — \$600

Internal cover, fully-colored:

First/second/third/fourth page
of cover (200×290 mm) — \$400

Internal insert:

Fully-colored (200×290 mm) —
\$340

Fully-colored (double page A3)
(400×290 mm) — \$500

• Article in the form of advertising
is 50 % of the cost of advertising
area

• When the sum of advertising con-
tracts exceeds \$1001, a flexible sys-
tem of discounts is envisaged

**Size of journal after cutting is
200×290 mm**

Editorial Board of Journals «Avtomaticheskaya Svarka» and «The Paton Welding Journal»

E.O. Paton Electric Welding Institute of the NAS of Ukraine

International Association «Welding»

11 Kazimir Malevich Str. (former Bozhenko Str.), 03150, Kiev, Ukraine

Tel.: (38044) 200 60 16, 200 82 77; Fax: (38044) 200 82 77, 200 81 45

E-mail: journal@paton.kiev.ua; www.patonpublishinghouse.com

VISIT TO WELDING CENTER OF ISF-2 PROJECT IN CHERNOBYL

Today interest to nuclear safety is relevant like never before. For Ukraine it is, first of all, connected with large-scale accident at Chernobyl NPP in 1986. By the initiative of the journal editorial board in July, 2018 there was organized a visit to ISF-2 facility of specialists of the E.O. Paton Electric Welding Institute in the lead of deputy director Prof. L.M. Lobanov.

Currently, works on project ISF-2 are carried out in Ukraine in order to solve the problem of safe storage of spent nuclear fuel as well as materials from ruined by accident 4th power generating unit of ChNPP. The project is held under the supervision of the International Atomic Energy Agency and agreements of SSE Chernobyl NPP with Holtec International Company, USA.

A course of work performance in Ukraine on ISF-2 project is carried out under the supervision of government, State Nuclear Regulatory Inspectorate of Ukraine and according to the project of Holtec International Company. Participation of the E.O. Paton Electric Welding Institute in the separate stages of ISF-2 construction at Chernobyl NPP is determined by the project.

It is supposed that at the end of 2018 there will be carried out the «hot» tests at new ISF-2 facility, which includes an object on preparation of spent nuclear fuel

and storage itself (Figure 2). Start of work in full capacity is planned for fourth quarter of 2019. Launching the new storage is rated as substantial forward step of Ukraine in development of facility, operation of which will allow changing the existing scheme of handling the spent nuclear fuel of domestic nuclear power plants, thus, strengthening energy security. It is planned that the facility will provide safe storage of the spent nuclear fuel from Rivne, Khmelnytskyi and South-Ukraine NPP for 100 years. Operation of the facility will be carried out using advanced technology of «dry» storage with two-barrier sealing system, which is provided with the help of special engineering systems of canister type from Holtec International Company. The latter are double-wall dry canisters (DWC) of around 4 m length and 2 m diameter.

Today DWCs of American production are delivered to ISF-2. It should be noted that SSE ChNPP is ready to consider the proposals of the Ukrainian enterprises on organization of production of such canisters using domestic materials.

Loading of spent nuclear fuel in DWC, welding of two main lids and welding-up of three auxiliary ports in the lids (Figures 3, 4) will be provided during ISF-2 operation. Automatic nonconsumable electrode welding with feeding of «hot» filler metal (welding



Figure 1. Object for SNF preparation



Figure 2. Storage of SNF

of the lids) and manual TIG (auxiliary ports) will be used for welding operations by Holtec International technology.

A welder-operator will carry out a remote control of the process of automatic multipass welding of the lids in the specially equipped site having the possibility of visual monitoring of the process and regulation of weld metal formation. For performance of this process Holtec has selected the arc equipment (power source and welding automatic machine with wire heating) of well-known company Liburdi (Figure 5).

E.O. Paton Electric Welding Institute carries out separate operations of technological processes of welding (under conditions of ChNPP exclusion zone) of seal welds on DWC loaded with spent nuclear fuel under the contract with Holtec International Company. They include:

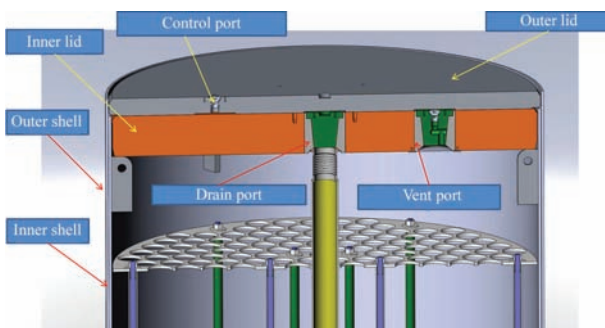


Figure 3. Scheme of performance of permanent joints

- elaboration of version of Holtec technological instructions for welding of seal welds;
- preparation of welding process flow-charts of each weld, their qualification and agreement with SNRIU applicable to working conditions in SSE ChNPP exclusion zone;



Figure 4. Welding-up of canister lid

- qualification of welding technological process at SSE ChNPP production facility for performance of welding of seal welds on DWC loaded with spent nuclear fuel;



Figure 5. Liburdi welding system

- training and qualification of welder-performers of DWC seal welds under conditions of ChNPP exclusion zone;
- participation in control field test of welding technological process of seal welds on DWC loaded with spent nuclear fuel;
- compiling the analytical scientific-technical reference-substantiation for granting SSE ChNPP with a license from SNRIU for performance of works on DWC sealing.

Currently, old storage contains 21297 spent fuel elements, which will be transferred to ISF-2. Every year it is planned to move 2500 fuel assemblies, i.e. in a 10-years period all the nuclear wastes will be located in ISF-2, period of storage of which is around 100 years.